

RIMS-1771

**Stability and bifurcations of two-dimensional zonal jet
flows on a rotating sphere**

By

Eiichi SASAKI

January 2013



京都大学 数理解析研究所

RESEARCH INSTITUTE FOR MATHEMATICAL SCIENCES

KYOTO UNIVERSITY, Kyoto, Japan

Stability and bifurcations of two-dimensional zonal jet
flows on a rotating sphere

Eiichi SASAKI

Research Institute for Mathematical Sciences, Kyoto University

Abstract

In planetary atmospheres in Jupiter or Saturn, for example, strong zonal jets have been observed. The existence of the zonal jet flow has been considered as one of the robust properties of planetary atmospheres.

The two-dimensional incompressible Navier-Stokes flow on a rotating sphere is considered to be one of the simplest and most fundamental models of the atmospheric motions taking into account the effect of the planetary rotation. The Reynolds number of the planetary atmospheres is so large that properties of the Navier-Stokes turbulence on a rotating sphere should be relevant to some aspect of the dynamics of the atmosphere. However, even in this simplest model, it is far from straightforward to obtain global properties of fully nonlinear solutions. In this thesis we discuss the Navier-Stokes flows on a rotating sphere, with an attention focused on the stability problem, the bifurcation structure of the zonal jet flows and chaotic solutions at high Reynolds numbers.

First we show the inviscid stability of the zonal jet flows on a rotating sphere. The semi-circle theorem obtained by Howard (1961) on a non-rotating planer domain is extended to the rotating sphere. We also study the linear stability of the zonal jet flows (l -jet flow) the streamfunction of which is expressed by a single spherical harmonics function Y_l^0 . This linear stability problem was first studied by Baines (1976), and his numerical result has been considered as a standard result for the zonal jet flows. We show that the critical rotation rates obtained by Baines include numerical errors caused by an emergence of singularities (critical layers), and we give accurate numerical results for the critical rotation rate by using a power-series expansion and a shooting methods taking into account the singular points.

Next, we study the viscous stability problem and the bifurcation diagram of the zonal jet flows, by introducing a forcing term balancing with the viscous dissipation terms. This setting is similar to the Kolmogorov problem, in which the stability and the bifurcation diagram of two-dimensional Navier-Stokes flows on a flat torus is considered. We prove rigorously that the 2-jet zonal flow is globally and asymptotically stable for an arbitrary Reynolds number and rotation rate. Then we study the linear stability of l -jet zonal flow for $l \geq 3$ and find an interesting phenomenon that the inviscid limit of the critical stability point does not coincide with the inviscid critical stability point. We also show that this is not a contradiction because the inviscid limit of the growth rates of the viscous unstable modes coincides with that of the inviscid unstable mode. In the numerical simulation by Obuse et al. (2010), the asymptotic states of forced two-dimensional turbulence are only the 2- or 3-jet zonal flows. A discussion is given on their results and our result on stability of laminar jets.

We study the bifurcation structure arising from the 3-jet zonal flow. In non-rotating case, at the critical Reynolds number, a steady traveling wave solution arises from the 3-jet zonal flow through the Hopf bifurcation. As the Reynolds number increases, several traveling solutions arise only through the pitchfork bifurcations and at high Reynolds numbers the steady bifurcating solutions become Hopf unstable. For the steady bifurcating solutions in

the non-rotation case, we find symmetry restoration of the streamfunction at high Reynolds numbers. Similar phenomenon has been found in Kolmogorov problem by Okamoto and Shōji (1993) and Kim and Okamoto (2010). In the rotating case, on the other hand, we find the saddle-node bifurcations and a closed-loop branch. These results show that the bifurcation structure changes drastically, as the absolute value of the rotation rate increases.

We also carry out time integration of unsteady zonal flows at high Reynolds numbers on the non-rotating/rotating sphere. We reproduce the zonal-mean zonal velocity of the unsteady solution from those of the unstable steady and steady traveling solutions by making a linear mapping from the solution space to the zonal-mean zonal profiles. In the non-rotating case, we find that the solutions are chaotic, and the reproduction of the zonal-mean profiles is satisfactory although the linear mapping assumes the linear inter- and extra-polation of the profile of the steady and steady traveling solutions in the solution space. However, in the rotating cases, the solution tends to be less chaotic under the stabilizing effect of rotation, and we find that the reproduced zonal flow by the linear mapping method does not approximate well the zonal-mean zonal velocity of the solutions. These results suggest that in the non-rotating case even the chaotic orbits at high Reynolds number lies mostly within a relatively low-dimensional box, the vertices of which are the steady and steady traveling solutions, and in the rotating case the relation between the unsteady solutions and the steady or steady traveling solutions changes as the effect of rotation increases.

Contents

1	Introduction	9
1.1	Planetary atmospheres and two-dimensional fluids	9
1.2	Two-dimensional turbulence in a plane	10
1.3	Effect of rotation on two-dimensional turbulence	10
1.4	Two-dimensional turbulence on a rotating sphere	11
1.5	Inviscid stability problem of zonal jets	11
1.6	Viscous stability of the zonal jets and Kolmogorov problem	12
1.7	Results of the present study	14
2	Stability of inviscid zonal jet flows on a rotating sphere	16
2.1	Introduction	16
2.2	Governing equations	17
2.3	Semi-circle theorem	18
2.4	Re-examination of the stability of inviscid zonal flow	20
	2.4.1 Stability analysis with a spectral method	20
	2.4.2 Stability analysis with a shooting method	22
2.5	Conclusion and Discussion	28
3	Stability and bifurcation structure of viscous zonal jet flows on a rotating sphere	30
3.1	Introduction	30
3.2	Governing equations	31
3.3	Global stability of 2-jet zonal flow	33
3.4	Linear stability of the l -jet zonal flows	35
3.5	Bifurcation structure of nonlinear steady solutions arising from 3-jet zonal flow	41
	3.5.1 Bifurcation diagram in the non-rotating case	42
	3.5.2 Bifurcation diagrams in the rotating case	42
	3.5.3 Characteristics of steady traveling solutions at high Reynolds number	48
3.6	Numerical simulations at high Reynolds number under 3-jet zonal forcing . .	51
	3.6.1 Properties of chaotic solutions in the non-rotating case	51
	3.6.2 Properties of solutions orbits in the rotating case	61

3.7 Conclusion and Discussion	67
4 Conclusion	70

List of Figures

2.1	Eigenvalues of linear stability of inviscid 3-jet zonal flow.	21
2.2	Unstable eigenvalues around $\Omega = \Omega_B^-$	22
2.3	Vorticity of the unstable eigenfunctions at $\Omega = \Omega_B^-$	23
2.4	Unstable eigenvalues around $\Omega = \Omega_B^+$	23
2.5	Vorticity of the unstable eigenfunction at $\Omega = \Omega_B^+$	24
2.6	Schematic of the integral path on the complex plane.	26
2.7	Stability eigenvalues around the negative critical rotation rate.	28
3.1	Critical Reynolds number of l -jet zonal flow in the non-rotating case.	36
3.2	Neutral curves and real part of phase velocity of 3- and 4-jet zonal flow on R - Ω plane.	38
3.3	Growth rates of the most unstable mode of 3-jet zonal flow.	40
3.4	Growth rates of the most unstable mode in regions of inviscid zonal flow is stable while viscous zonal flow is unstable.	40
3.5	Streamfunction and longitudinal velocity of 3-jet zonal flow.	41
3.6	Bifurcation diagram at $\Omega = 0.0$	43
3.7	Stable regions of nonlinear steady solutions on R - Ω plane.	44
3.8	Bifurcation diagram at $\Omega = -0.5$ and -1.0	46
3.9	Bifurcation diagram at $\Omega = 0.5$ and 1.0	47
3.10	Streamfunctions of TW1 at high Reynolds number.	49
3.11	Zonal-mean zonal velocity of TW1 and TW5 at $\Omega = 0.0$	50
3.12	Streamfunctions of TW5 at $\Omega = 0.0$	50
3.13	Streamfunctions of nonlinear steady solutions at $\Omega = 0.0$ and $R = 10^4$	52
3.14	Zonal-mean zonal velocities of nonlinear steady solutions at $\Omega = 0.0$ and $R = 10^4$	52
3.15	Time series and power spectrum of energy density of the chaotic orbits.	53
3.16	Snapshots of streamfunction of chaotic solution at $\Omega = 0.0$ and $R = 10^4$	54
3.17	Snapshots of zonal-mean zonal velocity of chaotic solution at $\Omega = 0.0$ and $R = 10^4$	54
3.18	Zonal-mean zonal velocity of the chaotic orbits.	55
3.19	Reproduction of time-averaged zonal-mean zonal velocity of the chaotic orbits.	57

3.20	Zonal-mean zonal velocity obtained by the linear mapping using a single steady/steady traveling solution.	59
3.21	The time series of the error of the approximation.	59
3.22	Ensemble-time-averaged error of the approximation.	60
3.23	Time-mean and ensemble-mean relative error of the linear mapping.	63
3.24	Power spectrum of the energy density of unsteady solutions at $\Omega = 0.0, \pm 0.5, \pm 1.0$ with $R = 10^3, 10^4$	64
3.25	Streamfunctions of nonlinear steady solutions at $\Omega = -1.0$ and $R = 10^3$. . .	65
3.26	Snapshot of chaotic solution at $\Omega = -1.0, R = 10^3$	65
3.27	Snapshot of quasi-periodic solution at $\Omega = -1.0, R = 10^3$	65
3.28	Reproduction of time-averaged zonal-mean zonal velocity of the time-periodic solution at $\Omega = -1.0, R = 10^3$	66

List of Tables

2.1	Critical rotation rates of inviscid l -jet zonal flows.	27
3.1	Lowest critical Reynolds number of l -jet zonal flow.	37
3.2	Critical rotation rates of viscous l -jet zonal flows.	39
3.3	The solutions used in the linear mapping	62
3.4	The type of solutions obtained by time integration.	66

Chapter 1

Introduction

1.1 Planetary atmospheres and two-dimensional fluids

Dynamics of fluid motion of human size have been investigated for over one hundred years, and fruitful insights in fluid motions have been obtained together with new attractive problems by experimental and theoretical studies. We now have rich knowledge about a set of simple fundamental flows which serve as components of complex fluid motions encountered in daily life. Recently, large-scale fluid phenomena in planetary atmospheres has been observable by using satellites and high-performance telescopes. However, the observational data is still quite lacking, and experimental study of most of these flows is impossible. The understanding the large-scale flows are therefore far from satisfactory compared to the flows in daily life, and our knowledge is quite limited even about simplest fundamental flows.

In planetary atmospheres in Jupiter or Saturn, for example, strong zonal jets have been observed, with their zonal-band pattern consisting of the eastward and westward alternating jets. The zonal flow in the atmospheres is observed in other planets in our solar system, and the existence of the zonal jet flow has been considered as one of the robust properties of planetary atmospheres. The dynamics of the planetary atmospheres includes such various effects arising from rotation, stratification, radiation, phase change of gas, topography, vegetation, ice and thermal heating. A full model of the atmospheric dynamics should take into account these complicated factors. However, on the other hand, it is also a problem whether such robust property of the atmospheres as zonal flows still arises in a simplified model as two-dimensional fluids on a rotating sphere. In this thesis, we are interested in the simplified model dealing with fluid flows governed by the two-dimensional incompressible Navier-Stokes equations on a rotating sphere, which may be the simplest model taking into account the effect of the planetary rotation, neglecting all the effect due to the thermal heating and the density stratification of atmospheres. In this model, non-dimensional parameters determining the dynamics are Reynolds number and the Rossby number (inverse of the non-dimensional rotating rate). In general, as Reynolds number increases, a fluid

motion becomes turbulent and the Reynolds number of the planetary atmospheres is quite huge, the two-dimensional Navier-Stokes turbulence on a rotating sphere is considered to be a model of the atmospheric motions.

1.2 Two-dimensional turbulence in a plane

In a non-rotating plane, two-dimensional turbulence is known to produce coherent large vortices through mergers and disappearances of small vortices in the course of time development (McWilliams [17]). The coherent vortices are considered to be associated with the energy inverse cascade, the energy transfer from small-scale to large-scale motions. The energy inverse cascade was first suggested by Kraichnan [15] together with the enstrophy cascade as an outstanding feature of the two-dimensional turbulence, in contrast with the energy cascade in three-dimensional turbulence where the energy transfers from large-scale to small-scale motions. His scaling theory predicted the $k^{-5/3}$ energy spectrum for the wavenumber range of the energy inverse cascade, while k^{-3} energy spectrum for the enstrophy cascading range, which has been tested repeatedly by many researchers and mostly accepted. The statistical properties of the two-dimensional turbulence in forced and freely decaying cases have attracted many researchers' interests (Boffetta and Ecke [3]), where the forcing, if any in our case, may be interpreted as vorticity forcing and the energy injection by small-scale thermal convection, while the freely decaying case is studied to find turbulence properties independent of the form of the forcing.

1.3 Effect of rotation on two-dimensional turbulence

It is well-known that the uniform horizontal rotation has no effect on the planar and incompressible two-dimensional turbulence because the Coriolis terms can then be absorbed in the pressure term. However, the rotation of the Earth, for example, is not uniform over the Earth's surface, and this non-uniform effect is, in a simplest way, taken into account by assuming a position dependence of the Coriolis parameter. The planar two-dimensional turbulence with the variable Coriolis parameter is expected to describe local properties of fluid motion on a rotating sphere. Eventually the two-dimensional Navier-Stokes equations with the Coriolis term in which the Coriolis parameter f is a linear function of one coordinate, i.e. $f = f_0 + \beta y$, is often employed as a model equation of local fluid motion on a rotating sphere. The two-dimensional turbulence in this model equation (the β -plane equation) is called the β -plane turbulence.

The β -plane turbulence has been known to have properties different from the ordinary (non-rotating) two-dimensional turbulence since the pioneer work of Rhines [27], who found that multiple zonal jet flows emerge in the course of time development and are robustly maintained for a long time, even if the initial flow field is isotropically turbulent. He then

suggested that the energy inverse cascade ceases roughly at a characteristic wavenumber k_β (now called Rhines wavenumber) where the rotation and the nonlinear effects are of the same order, and that an accumulation of the energy at k_β provides the multiple zonal jet flows. This mechanism has been extensively studied by many researchers [4, 2, 20], and interpreted from several points of view as the two-dimensional energy spectrum, the pseudo conserved quantity and the wave turbulence.

1.4 Two-dimensional turbulence on a rotating sphere

Numerical study of the two-dimensional turbulence on a rotating sphere was first performed by Williams [38], who investigated the forced two-dimensional turbulence on a rotating sphere under a symmetry assumption of the flow field, and found that zonal jet flows, similar to those of Jovian atmospheres and of the β -plane turbulence, emerges in a turbulent flow field. His results raised an expectation that the forced two-dimensional flow on a rotating sphere can be a fundamental model to the planetary atmospheres. However, his computational domain was restricted to 1/16 of the entire sphere under the assumptions of a longitudinal periodicity and the equatorial symmetry. Later Yamada and Yoden [39] first studied asymptotic states of freely decaying two-dimensional turbulence on a rotating sphere with no assumption on the flow field, and showed that circumpolar west-ward strong jets emerge along with multiple weak jets at the low and middle latitudes. Further Takehiro *et al.* [35] showed that as the rotation rate Ω of the sphere increases, the width of the circumpolar west-ward jets decreases as $\Omega^{-1/4}$ and the velocity of the jets increases as $\Omega^{1/4}$.

As for the forced turbulence on a rotating sphere, Nozawa and Yoden [21] performed numerical simulation with Markovian random forcing, and found that at the final stage of their computation, the flow field consists of multiple zonal jet flow and/or west-ward circumpolar jets, depending on the Rhines wavenumber and the forcing wavenumber. However, recently, Obuse *et al.* [22] re-calculated the same problem as Nozawa and Yoden with the numerical integration time being more than 100 times of that of Nozawa and Yoden, and found that at an early stage of time integration, the multiple zonal jet flows and the circumpolar jets are observed, but as time goes on, the zonal jets merge with each other, and at the final stage of time integration, only two or three broad zonal jets are left in the flow field. The surviving broad jets are found to be quite *stable* to disturbance even in the ambient turbulent flows.

1.5 Inviscid stability problem of zonal jets

The zonal flows in planetary atmospheres survives for a long time, and, as seen in the numerical simulation, some zonal flows are robust even in a turbulent environment. These observations lead us to the stability problem of the steady zonal flows on a rotating sphere.

First we are concerned with the inviscid stability problem of the zonal flows. One of the fundamental theorems for the inviscid linear instability of a zonal flow on the β -plane is the (extended) inflection-point theorem which gives so-called Rayleigh-Kuo's criterion (Kuo [16]), a necessary conditions for instability of the inviscid zonal flow. This theorem is extended to a rotating sphere (Baines [1]), and says that the necessary condition of the linear instability of a zonal flow is that the potential vorticity (as a function of the sine latitude) has an inflection point.

Another fundamental theorem for the inviscid linear stability is the semi-circle theorem, which was first derived by Howard [7] in a non-rotating case. This theorem restricts the possible region of unstable eigenvalues for the linear stability problem of a zonal flow. The semi-circle theorem was extended to a β -plane by Pedlosky [24, 25], and to a rotating sphere by Thuburn and Haynes [36]. In this thesis we give a different version of the semi-circle theorem on a rotating sphere, and compare it to those previously obtained.

On a rotating sphere, Baines [1] studied the inviscid linear stability of typical zonal jet flows, the streamfunction of which is expressed by a single spherical harmonics Y_l^0 , as well as the inviscid Rossby wave solutions. He solved the eigenvalue problem numerically with a spectral method using the spherical harmonics with the truncation wavenumber up to 20. The inflection-point theorem says that the zonal jet is stabilized when the rotation rate is large enough. Therefore the zonal flow has a critical rotation rates at which the zonal jets obtain the stability. He obtained numerically the critical rotation rate, and found that it is only slightly different from the estimates obtained from the inflection-point theorem. The numerical calculation of the stability eigenvalues by Baines [1] was significantly challenging at the time prior to the major advance of computational environment, and the obtained values have been frequently employed by many researchers (Huang *et al.* [8]). However, the numerical calculation is difficult even at present because of an emergence of singularities (critical layers), while Skiba [31] also discussed the difficulty of stable calculation from a view point of an accumulation of the continuous spectrum. Actually, as shown in this thesis, the numerical results of Baines [1] included relative errors up to 20%, and we will discuss accurate calculation of the eigenvalues in Chapter 2.

1.6 Viscous stability of the zonal jets and Kolmogorov problem

The viscous stability problem of the zonal flows is formulated by introducing a forcing term, which consists of a single spherical harmonics, to balance with the viscous dissipation term to keep the flow steady. Our interest lies in the bifurcation structure of the steady or steady traveling solutions, taking the Reynolds number as a bifurcation parameter. The relation between the results of the inviscid stability problem and the inviscid limit problem is also one of the subject of this thesis. Further we are interested in whether the asymptotic state of

the two-dimensional turbulence on a rotating sphere (Obuse et al. [22]) can be interpreted by the stability results of laminar zonal flows. These problems are open so far, although they are basic problems for the fluid motions on a rotating sphere.

Here we should give a brief overview on a similar problem on a flat plane. This problem is called Kolmogorov problem which was first proposed by Kolmogorov in his seminar in 1959 as a typical and simplest example to get insight into the solution properties of the Navier-Stokes equations. Kolmogorov considered a two-dimensional flow (on xy -plane), which is periodic with respect to both x - and y -directions, and is governed by the incompressible Navier-Stokes equations with an external force $(\sin ky, 0)$ where k is an integer. The Kolmogorov problem is thus concerned with the flows on a flat torus. In our case, on the other hand, the problem is formulated on a two-dimensional sphere, and with the forcing term consisting of a single spherical harmonics function which is an eigenfunction of the Laplacian similar to the forcing term in the Kolmogorov problem. Both the problems are formulated on a two-dimensional boundary-less compact manifold, and are quite similar to each other with a difference in the topology of the flow domain (genus 0 for the sphere, and genus 1 for the torus), and both they are expected to give an insight into the solutions of the Navier-Stokes equations.

For the Kolmogorov problem, Iudovichi [13] proved that the trivial two-jet flow ($k = 1$)¹ is globally stable at any Reynolds number, while Meshalkin and Sinai [18] proved that the critical modes of the trivial flows are steady (not Hopf), and Iudovich [13] proved the existence of the bifurcation solution arising at the critical stability point. Gotoh and Yamada [6] and Gotoh *et al.* [5] studied the linear stability of a general parallel flow in the case where the domain is infinite in the flow direction, and obtained the critical Reynolds number analytically. They also showed that, as the number of jets increases, the critical Reynolds number increases monotonically.

The bifurcation diagram of steady solutions arising from the 2-jet trivial flow was studied by Okamoto and Shōji [23] for several aspect ratios of the planar torus. They found a pitchfork bifurcation arising from the 2-jet trivial flow, and also found that as the aspect ratio changes, there appear several types of bifurcations including the saddle-node bifurcation, Hopf bifurcation and the secondary bifurcation. Also Kim and Okamoto[14] studied the inviscid limit of the steady solutions arising from 4- and 6-jet trivial flows. In each case the first and the second branches arise through the pitchfork bifurcations, and they found that the flow fields of the bifurcating steady solutions consists of multiple vortices around the bifurcation points. However, as the Reynolds number increases along the branches, smaller vortices merge into larger vortices, and the flow field becomes dominated only by a pair of a negative and a positive vortices at high Reynolds number. They called this solution *unimodal* solution, and suggested that at high Reynolds number there is a steady unimodal solution independently of the value of k . Similar phenomena were found also by Okamoto and Shōji [23]. We add that the simplicity of Kolmogorov flows drives other researches on

¹We call a parallel steady flow a *parallel* solution or *trivial* solution.

dynamical system properties such as routes to turbulence [26] and the orbital instability of chaotic flows [9]. We will discuss in this thesis the Navier-Stokes flows on a rotating sphere, with an attention focused on the viscous stability problem, bifurcation structure of the zonal jet flows and chaotic solutions at high Reynolds numbers.

1.7 Results of the present study

This thesis consists of two parts; the first part (Chapter 2) is concerned with the inviscid stability of the zonal jet flows on a rotating sphere. The semi-circle theorem obtained by Howard [7] on a non-rotating planer domain is extended to the rotating sphere in a different way from Thuburn and Haynes [36] (Section 2.3). In Section 2.4 we obtain accurate values of the critical rotation rate, by reconsidering the calculation of Baines [1] for the zonal jet flows the streamfunction of which is expressed by a single spherical harmonics Y_l^0 . We find that the eigenvalues obtained by the spectral method adopted by Baines [1] included numerical errors which do *not* decrease even by increasing the truncation wavenumber as far as practically available in the computation. Taking a close look at the eigenvalue calculation, we show that these numerical errors are caused by an emergence of singularities, called as critical layers, near the north and the south poles when the zonal flow approaches the critical stability state. To obtain the critical eigenvalues and the critical rotation rates with sufficient accuracy, we make use of the shooting method together with the power series expansion method, taking into account the singular points. As a result, we find that the critical rotation rates of Baines [1] should be corrected by $\sim 10\%$.

In the second part (Chapter 3), we study the viscous stability and bifurcation diagram of the zonal jet flow (l -jet flow) the streamfunction of which is expressed by a single spherical harmonics Y_l^0 . In section 3.3 we prove rigorously that the 2-jet zonal flow is globally and asymptotically stable for arbitrary Reynolds number and rotation rate. In section 3.4 we discuss the linear stability of l -jet zonal flow ($3 \leq l$). In non-rotating case, as the number of jets increases, the critical Reynolds number increases monotonically, where each jet is Hopf unstable at its critical point. In the rotating case, when the rotation rate increases, the critical Reynolds number of each zonal jet flow increases rapidly. We find that at large Reynolds numbers, the unstable region of the rotation rate is larger than that for the inviscid zonal flows, and the former does *not* converge to the latter even in the inviscid limit. We show that this seeming contradiction between the inviscid limit and inviscid cases is resolved by an observation that the growth rates of the unstable modes at the rotation rate which is both in the regions of the viscous instability and the inviscid stability, converge to zero, when the Reynolds number increases. In the numerical simulation by Obuse et al. [22], the asymptotic states of forced two-dimensional turbulence are only the 2- or 3-jet zonal flow. We find that in their calculation, the rotation rate is always larger than the critical rotation rate of the laminar jet flows, in the course of time development, except for some initial period. This means that the jet flows found in the intermediate stages would

be mostly stable if the jet flows were laminar, and therefore the route to the asymptotic state of the forced turbulence is not explained in the framework of the linear stability of laminar zonal jet flows, while the stability of the resultant 3-jet flow is supported by the linear stability of the laminar 3-jet flow.

In Section 3.5 we study bifurcation structure arising from the 3-jet zonal flow. In the non-rotating case, at the critical Reynolds number, a steady traveling wave solution arises from the 3-jet zonal flow through Hopf bifurcation. As the Reynolds number increases, several traveling solutions arise only through the pitchfork bifurcations and at high Reynolds numbers the steady bifurcating solutions become Hopf unstable. For the steady bifurcating solutions in the non-rotation case, we find the symmetry restoration of the streamfunction at high Reynolds numbers, while the 3-jet zonal flow does not have this symmetry. Similar phenomenon has been found in Kolmogorov problem by Okamoto and Shōji [23] and Kim and Okamoto [14]. In the rotating case, on the other hand, we find the saddle-node bifurcations and a closed-loop branch. These results show that the bifurcation structure changes drastically, as the absolute value of the rotation rate increases. It should be noted that no symmetry restoration is found in the rotating cases.

In Section 3.6 we carry out time integration of the unstable zonal flows at high Reynolds numbers on the non-rotating/rotating sphere. In the non-rotating case, we find that the solutions are chaotic. Observing the streamfunctions, we expect that properties of the chaotic solutions can be obtained by using unstable steady solutions. As an example, we reproduce the zonal-mean zonal velocity of the chaotic solutions by using those of the unstable steady and steady traveling solutions, by making a linear mapping from the solution space to the zonal-mean zonal profiles. We find that the reproduction of the zonal-mean profiles is satisfactory, although the linear mapping assumes the linear inter- and extrapolation of the profile of the steady and steady traveling solutions in the solution space. This result suggests that even the chaotic orbits at high Reynolds number lies mostly within a relatively low-dimensional box, the vertices of which are the steady and steady traveling solutions. In the rotating cases, on the other hand, the solution tends to be less chaotic under the stabilizing effect of rotation, and we find that the reproduced zonal flow by the linear mapping method does not approximate well the zonal-mean zonal velocity of the unsteady solutions at several Reynolds numbers and rotation rates. This result suggests that the relation between the unsteady solutions and the steady or steady traveling solutions changes as the effect of rotation increases.

Chapter 2

Stability of inviscid zonal jet flows on a rotating sphere

1

2.1 Introduction

Characteristics of two-dimensional barotropic fluid on a rotating sphere, which is one of the simplest models of planetary atmospheres taking into account the effects of planetary rotation and density stratification, have long been investigated [35, 22], and on the β -plane [16, 37]. The stability problem of barotropic zonal flows on a rotating sphere has also been studied in relation to the existence of large-scale zonal flows in the planetary atmospheres.

The first aim of this chapter is to develop a semi-circle theorem for the inviscid instability of zonal flows on a rotating sphere. The semi-circle theorem was first derived by Howard [7] for zonal flows in the non-rotating case, and was extended to the β -plane by Pedlosky [24, 25]. We extend the semi-circle theorem to zonal flows on a rotating sphere, where the radius of the circle depends on the angular velocity of the rotating frame of reference and we minimize the radius by choosing the most convenient frame of reference. A similar method was employed by Thuburn and Haynes [36] who obtained a semi-circle theorem in which the radius does not coincide with that given in this chapter.

The second aim of this chapter is to give corrected values of the critical rotation rate of stability. Baines [1] numerically studied the linear stability of inviscid barotropic zonal flow solutions on a rotating sphere, the streamfunction of which is expressed by the zonal spherical harmonics Y_l^0 , as well as inviscid Rossby wave solutions expressed by the spherical harmonics Y_l^m where $m \neq 0$. He solved the eigenvalue problem numerically with a spectral method with the truncation wavenumber up to 20. As suggested by the inflection-point theorem (Rayleigh's criterion), the zonal jet flows are stabilized when the rotation rate of

¹Published in Sasaki *et al.* [28]

the sphere is increased. He obtained for various zonal jet solutions the critical rotation rates at which the stability of zonal jets changes from unstable to stable. He also argued that the values of the critical rotation rates are only slightly above those estimated by the inflection-point theorem. The numerical calculation of eigenvalues by Baines [1] was significantly challenging at the time prior to the major advance of computational environment, and the obtained values have been frequently employed by many researchers. However, re-examining the numerical calculation, we find that the eigenvalues obtained by the spectral method adopted by Baines [1] include numerical errors which do not decrease even by increasing the truncation wavenumber as far as practically available in the computation. We should also note Skiba's argument that numerical calculation of some eigenvalues is not stable because of an accumulation of the continuous spectrum [31].

This chapter re-examines the stability of inviscid barotropic zonal flows on a rotating sphere, especially taking special care with the convergence of the eigenvalues. In section 2.2, the governing equation and its linearized equation are presented. A semi-circle theorem is derived in section 2.3. Section 2.4 elucidates imperfections of the numerical results of the stability eigenvalues obtained by a spectral method, and instead a shooting method is employed to overcome the problems. A conclusion follows in Section 2.5.

2.2 Governing equations

A two-dimensional incompressible barotropic inviscid flow on a rotating sphere is governed by the equation of vorticity,

$$\frac{\partial \Delta \psi}{\partial t} + J(\psi, \Delta \psi) + 2\Omega \frac{\partial \psi}{\partial \lambda} = 0. \quad (2.1)$$

Here t is the time, λ and ϕ are the longitude and the latitude, and $\mu = \sin \phi$ is the sine latitude; ψ is the streamfunction and $\Delta \psi$ is the vorticity, where Δ is the horizontal Laplacian on an unit sphere. The longitudinal and latitudinal components of velocity (u_λ, u_μ) are given by $u_\lambda = -\sqrt{1 - \mu^2}(\partial \psi / \partial \mu)$ and $u_\mu = 1/\sqrt{1 - \mu^2}(\partial \psi / \partial \lambda)$, respectively. $J(A, B) = (\partial A / \partial \lambda)(\partial B / \partial \mu) - (\partial B / \partial \lambda)(\partial A / \partial \mu)$ is the Jacobian operator, and Ω is the non-dimensional constant rotation rate of the sphere.

A general zonal flow $\psi = \psi_0(\mu)$ is a steady solution of the equation of vorticity (2.1), regardless of the rotation rate. Here we consider steady zonal flow solutions with l jets described by a 4π normalized spherical harmonic function $Y_l^m(\lambda, \mu)$ as

$$\psi_0 = \Psi_0(\mu) = -\frac{1}{l(l+1)} Y_l^0(\mu), \quad (2.2)$$

which we call l -jet flow. Here, the number of jets is defined as the number of extreme points of the longitudinal velocity, which is equal to the number of nodes of the latitudinal distribution of the streamfunction.

In order to examine the linear stability of the inviscid zonal flow $\psi_0(\mu)$, we substitute $\psi = \psi_0(\mu) + \psi'(\lambda, \mu, t)$ into (2.1) and neglect the second order terms of ψ' . Assuming that $\psi' = \hat{\psi}(\mu)e^{im(\lambda-ct)}$, we finally have a linearized equation of vorticity

$$[U(\mu) - c]\Delta_m \hat{\psi} + \left\{ 2\Omega - \frac{d^2}{d\mu^2} [(1 - \mu^2)U(\mu)] \right\} \hat{\psi} = 0. \quad (2.3)$$

Here, $U(\mu) = -d\psi_0(\mu)/d\mu$ is the angular velocity of the basic zonal flow and Δ_m is defined as $\Delta_m = \frac{d}{d\mu}(1 - \mu^2)\frac{d}{d\mu} - \frac{m^2}{1 - \mu^2}$. The boundary conditions at the north and the south poles are given by

$$\hat{\psi}(\pm 1) = 0. \quad (2.4)$$

Equations (2.3) and (2.4) constitute an eigenvalue problem with the eigenvalue c being the complex angular phase velocity.

2.3 Semi-circle theorem

We introduce the latitudinal displacement of the perturbation $\eta = \hat{\eta}(\mu) \exp[im(\lambda - ct)]$. The material derivative of η is related to the latitudinal component of the perturbation velocity u'_μ as

$$u'_\mu = \frac{D\eta}{Dt} = \left(\frac{\partial}{\partial t} + U \frac{\partial}{\partial \lambda} \right) \eta.$$

Then, $\hat{\psi}$ can be expressed by $\hat{\eta}$ as $\hat{\psi} = \sqrt{1 - \mu^2}(U - c)\hat{\eta}$. Substituting $\hat{\eta}$ into (2.3) and taking the inner product with $\sqrt{1 - \mu^2}\hat{\eta}^*$, where $*$ indicates complex conjugate, we obtain

$$\int d\mu [(U - c_r)^2 - c_i^2] P = 2(\Omega + c_r) \int d\mu (U - c_r) Q + 2c_i^2 \int d\mu Q, \quad (2.5)$$

$$c_r \int d\mu (P + 2Q) = \int d\mu U (P + Q) - \Omega \int d\mu Q. \quad (2.6)$$

Here, c_r and c_i are the real and imaginary parts of c , and $P = P(\mu)$ and $Q = Q(\mu)$ denote $P(\mu) = (1 - \mu^2)^2 \left| \frac{d\hat{\eta}}{d\mu} \right|^2 + (m^2 - 1)|\hat{\eta}|^2 > 0$, and $Q(\mu) = (1 - \mu^2)|\hat{\eta}|^2 > 0$. Expansion of $\phi = \sqrt{1 - \mu^2}\hat{\eta}$ by the associated Legendre polynomials, $\phi = \sum_{n=m}^{\infty} \phi_n^m P_n^m(\mu)$ gives

$$\int d\mu (P + 2Q) \geq m(m + 1) \int d\mu Q. \quad (2.7)$$

When $\Omega \geq 0$, (2.6) yields

$$\begin{aligned} c_r &\leq \frac{\int d\mu U_{max}(P + Q)}{\int d\mu (P + 2Q)} \leq U_{max}, \\ c_r &\geq \frac{\int d\mu U_{min}(P + Q)}{\int d\mu (P + 2Q)} - \Omega \frac{\int d\mu Q}{\int d\mu (P + 2Q)} \geq U_{min} - \frac{\Omega}{m(m + 1)}, \end{aligned}$$

where we have made an assumption for the angular velocity,

$$U_{max} = \max_{-1 \leq \mu \leq 1} U(\mu) > 0, \quad U_{min} = \min_{-1 \leq \mu \leq 1} U(\mu) < 0. \quad (2.8)$$

Thus, we obtain the following condition for the phase velocity:

$$U_{min} - \frac{\Omega}{m(m+1)} \leq c_r \leq U_{max}, \quad (\text{for } \Omega \geq 0). \quad (2.9)$$

The assumption (2.8) is temporal, and we will remove it at the end of this proof.

An obvious inequality,

$$0 \geq \int d\mu (U - U_{min})(U - U_{max})P = \int d\mu [U^2 - (U_{max} + U_{min})U + U_{min}U_{max}]P,$$

with (2.5) and (2.6) yields

$$0 \geq \int d\mu (c_r^2 + c_i^2)(P + 2Q) - (U_{max} + U_{min})UP + U_{max}U_{min}P + 2\Omega UQ$$

which leads to

$$\begin{aligned} & \left[\left(c_r - \frac{U_{max} + U_{min}}{2} \right)^2 + c_i^2 - \left(\frac{U_{max} - U_{min}}{2} \right)^2 \right] \int d\mu (P + 2Q) \\ & \leq |\Omega| (U_{max} - U_{min}) \int d\mu Q. \end{aligned}$$

Then, using (2.7), we obtain

$$\left(c_r - \frac{U_{max} + U_{min}}{2} \right)^2 + c_i^2 - \left(\frac{U_{max} - U_{min}}{2} \right)^2 \leq \frac{|\Omega|}{m(m+1)} (U_{max} - U_{min}). \quad (2.10)$$

Here we should note that if the angular velocity of the system of coordinates is changed from Ω to $\Omega + \omega$, where $U_{min} \leq \omega \leq U_{max}$ (see (2.8)), then U and c_r become $U - \omega$ and $c_r - \omega$ with c_i unchanged, i.e. the left hand side of (2.10) is unchanged. Therefore, by taking ω which minimizes $|\Omega + \omega|$ we obtain more restricted ranges for c_r and c_i as

$$U_{min} - \frac{|\Omega + U|_{min}}{m(m+1)} \leq c_r \leq U_{max} \quad (\text{for } \Omega > 0),$$

and

$$\left(c_r - \frac{U_{max} + U_{min}}{2} \right)^2 + c_i^2 \leq \left(\frac{U_{max} - U_{min}}{2} \right)^2 + \frac{|\Omega + U|_{min}}{m(m+1)} (U_{max} - U_{min}), \quad (2.11)$$

which gives the semi-circle theorem. Remarkably this semi-circle theorem is valid even when $U(\mu)$ does not satisfy (2.8), because then we can choose rotating coordinates where $U_{min} - \omega < 0 < U_{max} - \omega$. Therefore the assumption (2.8) is unnecessary for the semi-circle theorem to hold.

A semi-circle theorem has been obtained by Thuburn and Haynes [36], in which the radius of the circle is different from that obtained here. Our derivation is different in that the present P and Q allow us to utilize a property of Legendre functions. We note that the radius of (2.11) is smaller than or equal to that of Thuburn and Haynes [36] except when $3 - 2\sqrt{2} \leq |\Omega + U|_{min}/|\Omega + U|_{max} < 1/3$ and both $|\Omega + U|_{min}$ and $|\Omega + U|_{max}$ are sufficiently small. We should note that another semi-circle theorem was stated in the Appendix of Ishioka and Yoden [12], where $|\Omega + U|_{min}/(m(m + 1))$ in (2.11) is replaced by $|\Omega + U|_{max}/(m^2 + 1 + m^2/(2|m| + 3))$.

2.4 Re-examination of the stability of inviscid zonal flow

In this section, we re-examine the linear stability of the inviscid zonal flow (2.2) on a rotating sphere. This problem was previously investigated by Baines [1], but we show that some numerical corrections are necessary, taking into account singular behavior of eigenfunctions. The 1-jet and 2-jet zonal flows are linearly stable due to conservation laws of angular momentum, energy and enstrophy [1]. However, l -jet zonal flows with $l \geq 3$ can be unstable, and we consider the cases of $3 \leq l \leq 9$, the same range of l as Baines. The unstable modes of l -jet zonal flow do not contain the spherical harmonics $Y_n^m(\lambda, \mu)$ with $|m| \geq l$ as proved by Skiba [30] and Ishioka and Yoden [12]. Also, zonal modes $Y_n^0(\mu)$ are all neutral modes. Therefore, it is sufficient to study disturbances with the azimuthal wavenumber $1 \leq |m| \leq l - 1$.

2.4.1 Stability analysis with a spectral method

First, we present numerical results of stability obtained by a spectral method, essentially in the same way as Baines [1]. In order to solve the eigenvalue problem of (2.3) and (2.4) for a given azimuthal wavenumber m of the disturbance, we assume the streamfunction $\hat{\psi}(\mu) = \sum_{n=m}^N \psi_n^m P_n^m(\mu)$ where ψ_n^m are the expansion coefficients and N is the truncation wavenumber. On evaluating the terms $U(\mu)\Delta_m\hat{\psi}(\mu)$ and $(d^2/d\mu^2)[(1-\mu^2)U(\mu)]\hat{\psi}(\mu)$ in (2.3), we adopt a transform method, employing in the physical space the numbers of longitudinal and latitudinal grid points I and J satisfying $I \geq 3N + 1$ and $J > 3N/2$ in order to eliminate aliasing errors.

Figure 2.1 shows the numerical eigenvalues for $m = 1, 2$ in the case of the 3-jet zonal flow. Baines calculated the eigenvalue for the same problem, and concluded that the 3-jet flow is unstable for $\Omega_B^- = -5.35 < \Omega < 1.76 = \Omega_B^+$ [1]. We show in figure 2.2 the

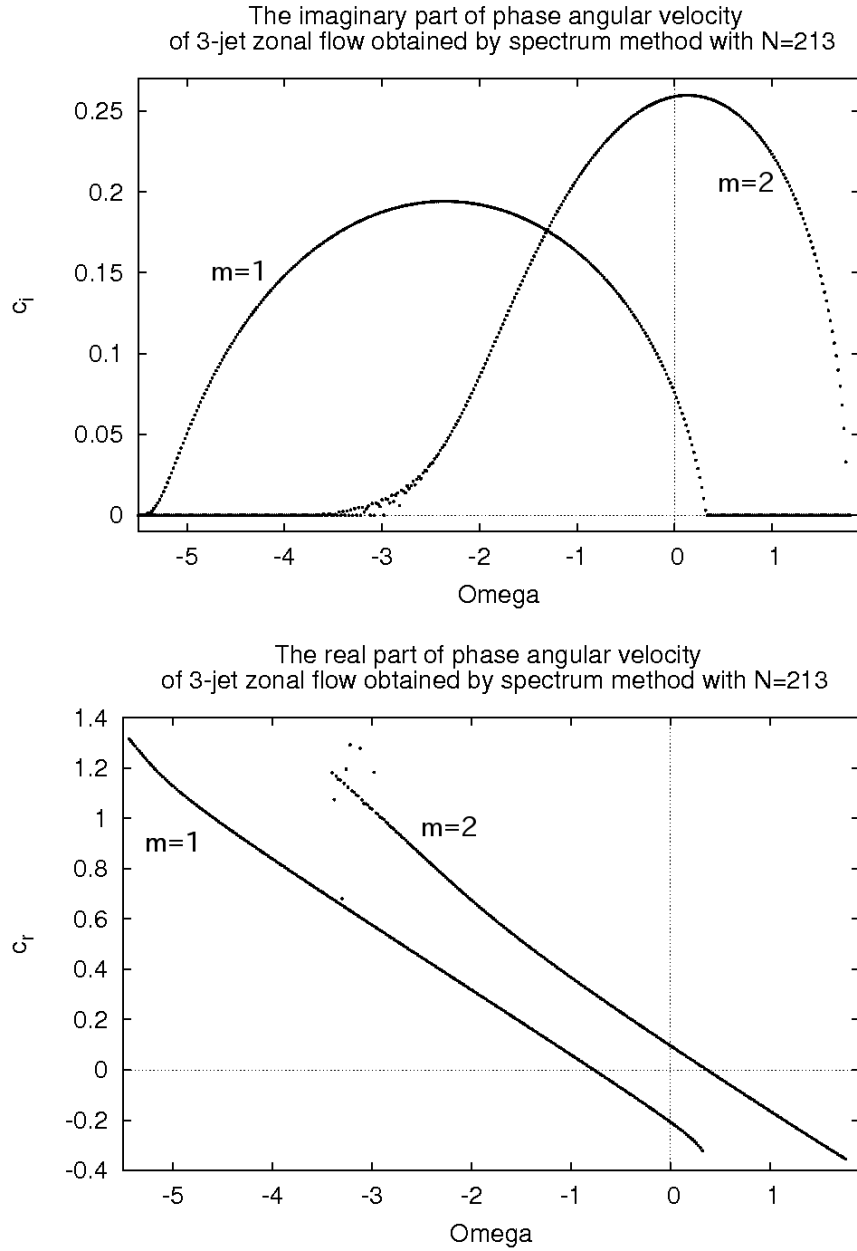


Figure 2.1: The eigenvalues of linear stability of 3-jet zonal flow for $m = 1$ and 2 obtained with the spectrum method with the truncation wavenumber $N = 213$: the left and right figures show the imaginary and real parts of the phase angular velocity c_i and c_r , respectively. The horizontal and vertical axes are the rotation rate Ω and the eigenvalues respectively.

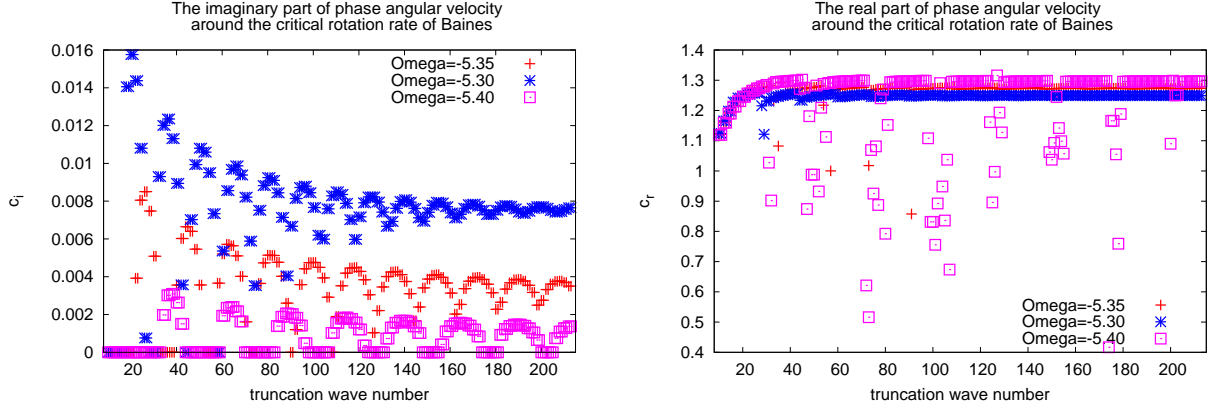


Figure 2.2: The unstable eigenvalues around $\Omega = \Omega_B^-$, which is the critical rotation rate obtained by Baines: the left and right figures show the imaginary and real parts of phase angular velocity, c_i and c_r , respectively. The horizontal and vertical axes are the truncation wavenumber N and the eigenvalues, respectively.

eigenvalues obtained in our numerical calculation around Baines' negative critical rotation rate $\Omega_B^- = -5.35$ as a function of the truncation wavenumber N . The imaginary part of phase angular velocity c_i does not converge even when the truncation wavenumber is increased up to 10 times of that used by Baines, although the real part c_r can be obtained with three-digit accuracy, which is equal to 1.27 at $\Omega = \Omega_B^-$.

The eigenfunction at $\Omega = \Omega_B^-$ is shown in figure 2.3 (left). It is observed that the vorticity diverges near $\mu = \pm 1$, indicating singularities near the north and south poles. The critical points, where $U(\mu) - c_r = 0$, appear around $\pm 79.7^\circ$ in latitude. The divergence behavior of c_i is caused by lack of resolution around the critical layers of the eigenfunction emerging near the poles.

On the other hand, when $\Omega > 0$, the eigenvalues converge fairly well. We find that the positive critical rotation rate Ω_c^+ is 1.77194, and the critical azimuthal wavenumber $m_c = 2$. Figure 2.4 shows the eigenvalues around $\Omega = \Omega_B^+$. The eigenvalues can be obtained with 0.1% accuracy when the truncation wavenumber is increased up to 63. The slightly unstable eigenfunction at $\Omega = 1.7719$ is shown in figure 2.5. Obviously, no critical point is found, in contrast to the cases near the negative critical rotation rate.

2.4.2 Stability analysis with a shooting method

In the previous subsection, it is shown that in the spectral method c_i does not converge even when the truncation wavenumber is increased, because the critical layers appear in the eigenfunctions. In this subsection, instead of the spectral method, we make use of a shooting method to overcome the difficulty.

2.4 Re-examination of the stability of inviscid zonal flow

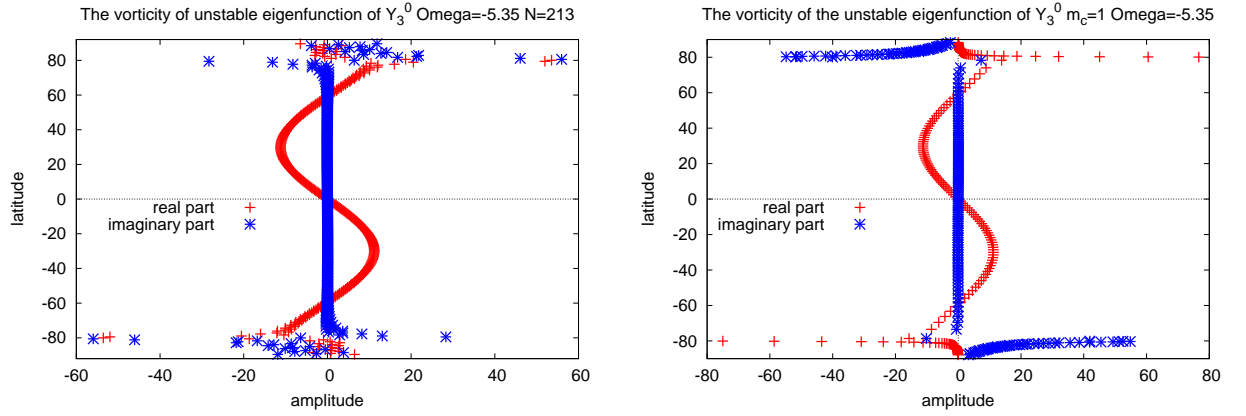


Figure 2.3: The vorticity of unstable eigenfunctions in the case of 3-jet zonal flow at $\Omega = \Omega_B^-$ with azimuthal wavenumber $m = 1$: the left and right figures are obtained by the spectral method with truncation wavenumber $N = 213$ and by the shooting method, respectively.

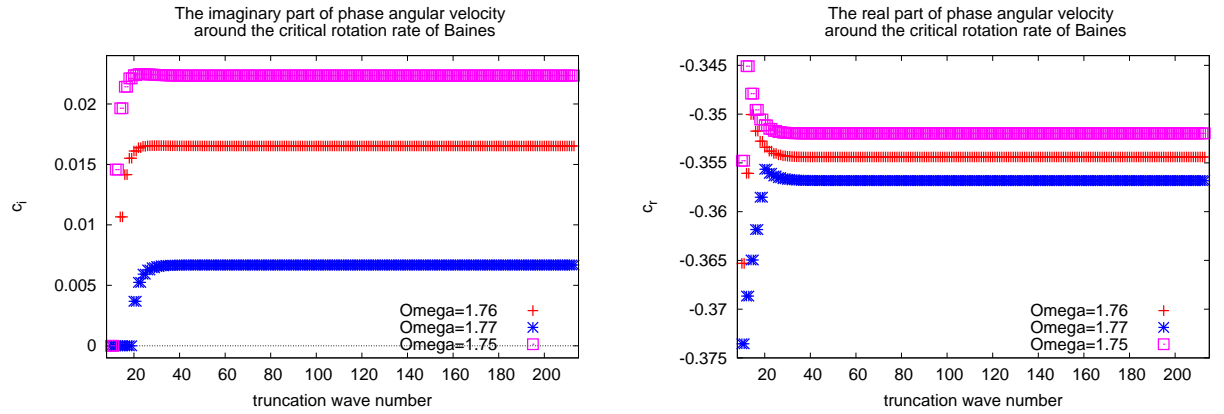


Figure 2.4: Same as figure 2.2 but for the unstable eigenvalues around $\Omega = \Omega_B^+$: the left and right figures show the imaginary part and the real part respectively.

2 Stability of inviscid zonal jet flows on a rotating sphere

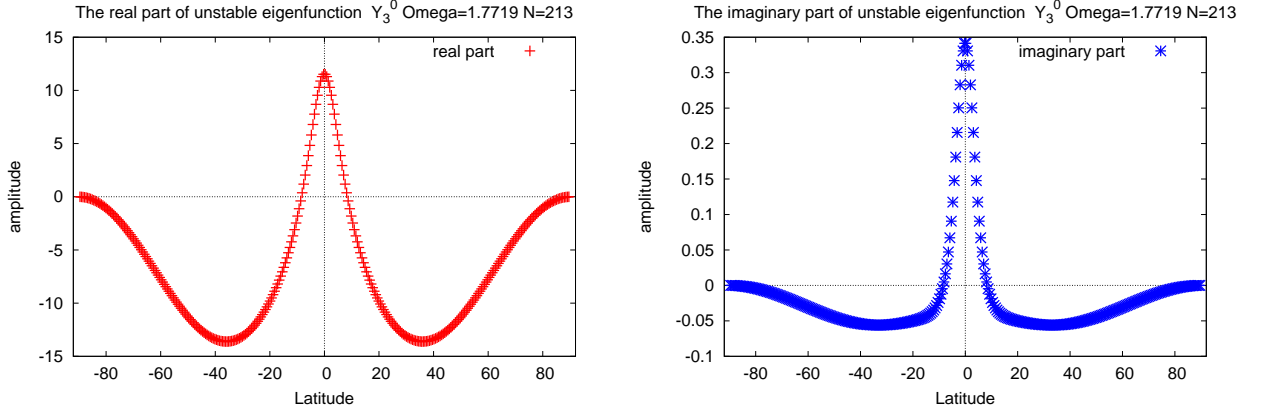


Figure 2.5: Same as figure 2.3 but for the vorticity of unstable eigenfunctions of 3-jet zonal flow Y_3^0 at $\Omega = 1.7719$ with azimuthal wavenumber $m = 2$ with the truncation wavenumber $N = 213$: the left and right figures shows the imaginary part and the real part, respectively.

Equation (2.3) is expressed in the normal form as follows:

$$\frac{d}{d\mu} \begin{pmatrix} \hat{\psi} \\ \hat{\phi} \end{pmatrix} = \begin{pmatrix} 0 & 1 \\ -\frac{l(l+1)U(\mu) + 2\Omega}{\{U(\mu) - c\}(1 - \mu^2)} + \frac{m^2}{(1 - \mu^2)^2} & \frac{2\mu}{1 - \mu^2} \end{pmatrix} \begin{pmatrix} \hat{\psi} \\ \hat{\phi} \end{pmatrix}, \quad (2.12)$$

where $\hat{\phi} = d\hat{\psi}/d\mu$.

For a given value of Ω , we obtain the solution $\hat{\psi}^-$ and $\hat{\phi}^-$ by integrating the normal form of the equation (2.12) from the edge point $\mu = -1$ to a certain point $\mu_0 \in (-1, 1)$ with the boundary conditions (2.4). Then we obtain the other solution $\hat{\psi}^+$ and $\hat{\phi}^+$ by integrating it from $\mu = 1$ to $\mu = \mu_0$.

The matching condition consists of continuity of streamfunction $\hat{\psi}$ and its derivative $\hat{\phi}$, which is expressed by

$$f(\Omega, c_r, c_i) = \begin{vmatrix} \hat{\psi}^+(\mu_0) & \hat{\psi}^-(\mu_0) \\ \hat{\phi}^+(\mu_0) & \hat{\phi}^-(\mu_0) \end{vmatrix} = 0.$$

The point μ_0 can be chosen at any point on the integral path. However, in this problem, the critical points are expected to exist around both the poles $\mu = \pm 1$. We then select μ_0 as the end point of each integration and take $\mu_0 = 0.1$ which is far from both the poles.

In the above integrations, we should consider the singular points $\mu = \pm 1$ and critical points μ_c such that $U(\mu_c) - c = 0$.

First, in order to avoid the difficulty arising from the singular points, we change the starting point of the numerical integration from $\mu = \pm 1$ to certain nearby points. The values of $\hat{\psi}$ and $\hat{\phi}$ are obtained by using a power series expansion of the solution: At the

south pole $\mu = -1$, $\hat{\psi}$ is expanded into a power series of $z = \mu + 1$ as

$$\hat{\psi} = z^{m/2} \left(1 + \sum_{j=1}^{J_t} a_j z^j \right) \quad (2.13)$$

where J_t is a sufficiently large number and is taken up to 20. The coefficients a_j of the series are successively determined by expanding (2.3) around $\mu = -1$. The starting point should be close to the south pole to keep the accuracy of the power series expansion. Moreover, near marginal stability, the critical layer approaches the pole, which means that the convergence radius becomes small, and therefore we have to pay attention to the choice of the starting point. The same scenario holds also for the north pole. Second, we have to solve the singular behavior of the solution around the critical point $\mu = \mu_c$. Near marginal stability, the critical point approaches the interval $[-1, 1]$, and the numerical integration along the μ -axis rapidly becomes difficult. Then, in order to find the marginal stability eigenvalue as the limit of unstable eigenvalues, we deform the integral path in the complex μ -plane to bypass the critical points in such a way that $\pi \leq \arg \mu \leq 2\pi$ or $0 \leq \arg \mu \leq \pi$ if $U'(\mu_c) > 0$ or $U'(\mu_c) < 0$, respectively.

Specifically, we employ a piecewise linear path as shown in figure 2.6. On integrating the normal form (2.12) from the south pole (A) $\mu = -1$ to (E) μ_0 , we divide the integration path into four sections: (A)→(B)→(C)→(D)→(E), where the power series expansion is employed for the section (A)→(B), and the integrals for the other sections are performed by the 4th-order Runge-Kutta method with the number of grid points being about 3×10^4 . From the north pole (I) $\mu = 1$ to (E), we perform the calculation in a similar way to the above in the order of (I)→(H)→(G)→(F)→(E).

We perform this shooting method to determine $c = c_r + ic_i$ for given values of Ω by use of the Newton method. The stopping condition of the Newton method is that the rate of the correction of the eigenvalues is less than 10^{-8} . The Jacobi matrix

$$\begin{pmatrix} \frac{\partial \text{Re}[f]}{\partial c_r} & \frac{\partial \text{Re}[f]}{\partial c_i} \\ \frac{\partial \text{Im}[f]}{\partial c_r} & \frac{\partial \text{Im}[f]}{\partial c_i} \end{pmatrix}$$

is evaluated by the central finite difference method with $\delta c_r, \delta c_i = 10^{-6}$.

We also perform this shooting method to determine Ω_c and c_r for $c_i = 0$. Skiba [31] argued that numerical calculation of some eigenvalues is not stable because of the accumulation of the continuous spectrum. In our calculation we checked the numerical convergence of the eigenvalue by changing the number of grid points to 6×10^3 and 6×10^5 and confirmed that the relative errors of c_r and c_i (or Ω_c and c_r) are less than 0.1%. Also, we have changed the increments of δc_r and δc_i for the evaluation of the Jacobi matrix from 10^{-6} to 10^{-5} and found that the relative errors of the critical rotation rates and the eigenvalues remain less than 0.1%. Further, we have checked that the obtained eigenvalues and eigenfunctions are

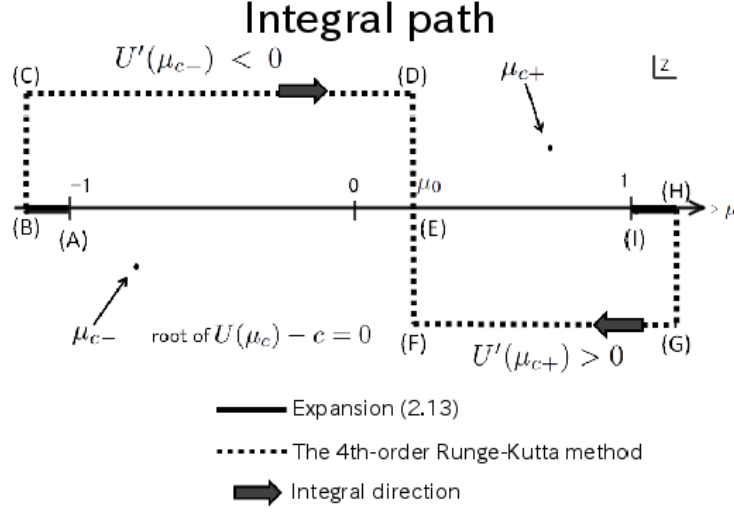


Figure 2.6: Schematic of the integral path on the complex plane $\mu \in \mathbb{C}$. The solid and the dashed lines indicate the integrations by the expansion method and the Runge-Kutta method, respectively.

consistent with the inflection-point theorem and the semi-circle theorem, and that the ratio of the energy and the enstrophy of the eigenfunction is $l(l+1)$ as derived by Skiba [32] for the zonal flow Y_l^0 .

Figure 2.7 shows the stability eigenvalues obtained for the 3-jet zonal flow. For the sake of comparison, the eigenvalues obtained by the spectral method are also shown. It is seen that the eigenvalues obtained by the shooting method converge better than those obtained by the spectral method. We find the negative critical rotation rate $\Omega_c^- = -5.45685$ and the critical azimuthal wavenumber $m_c = 1$. The unstable eigenfunction at $\Omega = \Omega_B^-$ is shown in figure 2.3 (right). The vorticity around the critical layers is more accurately shown in the shooting method solution, compared with the spectral method solution in figure 2.3 (left).

We also show the critical rotation rates of other zonal jet solutions (2.2) in table 3.2. There are a $\sim 10\%$ differences between the critical rotation rates of Baines, Ω_B^\pm , and of the present study, Ω_c^\pm . When the number of zonal jets l is odd and $\Omega < 0$, the critical layers emerge around both the north and the south poles. When l is even, the critical layer arises around the south (north) pole for $\Omega > 0 (< 0)$. When l is odd and $\Omega > 0$, the critical eigenfunction does not have a singularity.

The inflection-point theorem states that when the basic flow is unstable, there is at least one zero point of $\tilde{\beta} = 2\Omega + dY_l^0(\mu)/d\mu$ in the interval $\mu \in [-1, 1]$. This condition gives the possible range of the critical rotation rates, the upper and the lower bounds of which are given in table 3.2 as Ω_I^\pm . However, Ω_I^\pm do not coincide with Ω_c^\pm , with relative differences up

l -jet	Ω_c^\pm	m_c^\pm	μ_c^\pm	Baines Ω_B^\pm	m_B^\pm	relative error	Ω_I^\pm	relative difference
3	-5.4568	1	± 1	-5.35	1	1.95%	$-3\sqrt{7}$	45.4%
	1.7719	2	-	1.76	2	0.673%	$3\sqrt{7}/4$	11.9%
4	-9.7700	1	1	8.78	1	9.49%	-15	53.5%
	9.7700	1	-1	8.78	1	9.49%	15	53.5%
5	-19.22	1	± 1	-18.2	1	5.21%	$-15\sqrt{11}/2$	29.4%
	4.022	3	-	3.90	3	3.03%	$-15\sqrt{11}/16$	177%
6	-28.389	1	1	-25.0	1	11.9%	$-21\sqrt{13}/2$	33.3%
	28.389	1	-1	25.0	1	11.9%	$21\sqrt{13}/2$	33.3%
7	-44.445	1	± 1	-40.0	1	10.0%	$-14\sqrt{15}$	24.2%
	7.8929	3	-	7.226	3	8.44%	$35\sqrt{15}/32$	86.3%
8	-59.618	1	1	-48.4	1	18.8%	$-18\sqrt{17}$	24.4%
	59.618	1	-1	48.4	1	18.8%	$18\sqrt{17}$	24.4%
9	-83.340	1	± 1	-69.3	1	16.8%	$-45\sqrt{19}/2$	17.6%
	13.665	3	-	11.5	1	15.8%	$-315\sqrt{19}/256$	139%

Table 2.1: The critical rotation rates of inviscid zonal flows $\Psi_0 = -Y_l^0(\mu)/l(l+1)$. Column 1 shows the number of jets l of the basic flows. Columns 2, 3, and 4 indicate the results of the present study: the critical rotation rate Ω_c^\pm , the critical azimuthal wavenumber m_c^\pm , and the sine latitude of critical layers μ_c^\pm . Columns 5, 6, and 7 are the results of [1] for the sake of comparison: the critical rotation rate Ω_B^\pm , the critical azimuthal wavenumber m_B^\pm , and the relative errors of critical rotation rates between [1] and the present study. Columns 8 and 9 indicate the critical rotation rates Ω_I^\pm estimated by the inflection-point theorem and their relative difference from the critical rotation rate Ω_c^\pm obtained by the present study.

2 Stability of inviscid zonal jet flows on a rotating sphere

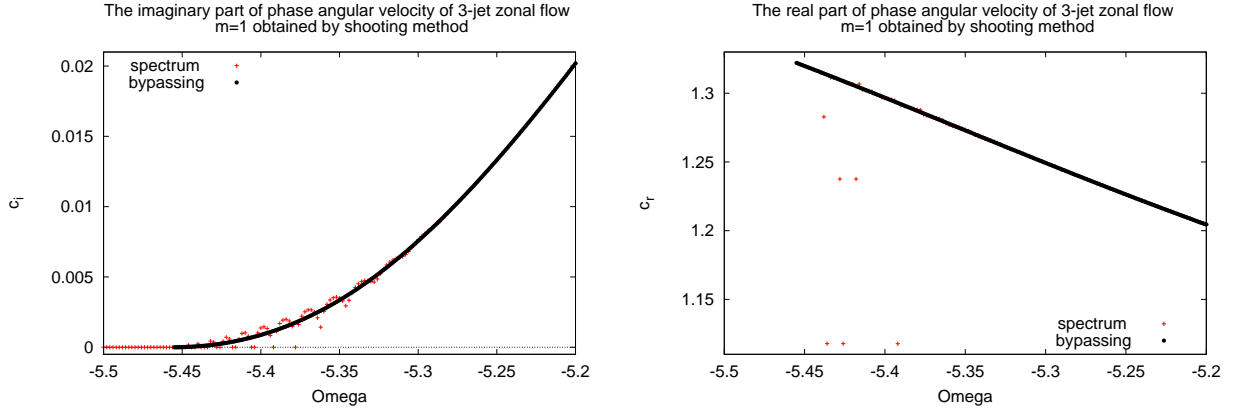


Figure 2.7: The stability eigenvalues for the 3-jet zonal flow $m = 1$ around the negative critical rotation rate: the left and right figures show the imaginary and real parts of phase angular velocity c_i and c_r , respectively. The horizontal and vertical axes indicate the rotation rate Ω and the eigenvalues, respectively. The black dots are the results by the shooting method, while the red crosses are those by the spectral method with $N = 213$.

to $\sim 170\%$. This suggests that stability characteristics of zonal flows on a rotating sphere are rather different from those of parallel flows on a plane where the inflection point is often related to the emergence of instability.

We remark that in the case of the 3-jet flow, the critical rotation rate Ω_c^- can be obtained analytically. In the 3-jet case, under the assumption that the critical point exists at each pole, we find $c = c_r = \sqrt{7}/2$ and $U - c_r = 5\sqrt{7}(\mu - 1)(\mu + 1)/8$. Substituting these into equation (2.3) with $\{(1 - \mu^2)U\}'' = -3(3 + 1)U$, we have

$$\frac{d}{d\mu} \left\{ (1 - \mu^2) \frac{d\hat{\psi}}{d\mu} \right\} - \frac{\alpha}{1 - \mu^2} \hat{\psi} = -3(3 + 1)\hat{\psi}, \quad (2.14)$$

where $\alpha = m^2 + 16\Omega/5\sqrt{7} + 48/5$. If α is a square of an integer number, $\alpha = \tilde{m}^2$, the linear operator of the left hand side of equation (2.14) becomes $\Delta_{\tilde{m}}$ and the eigenfunction is the associated Legendre function $P_3^{\tilde{m}}(\mu)$. Figure 2.3 shows the similarity of $\hat{\psi}$ to $P_3^2(\mu)$, and we choose $\tilde{m} = 2$, which yields $\Omega_c = -33\sqrt{7}/16 = -5.456862 \dots$, in agreement with the numerical result. The case of $m = 2, \tilde{m} = 3$ corresponds to $\Omega_c = -3.807$ where an unstable mode arises from the neutral mode. According to the numerical results, for all other combinations of m, \tilde{m} , unstable modes do not arise from the neutral modes.

2.5 Conclusion and Discussion

In this chapter we re-examine the linear stability of inviscid barotropic zonal flows on a rotating sphere. A semi-circle theorem for zonal flows on a rotating sphere is derived. The

critical rotation rates for stability of zonal flows are obtained more accurately than the previous study by Baines [1].

By the spectral method, the critical eigenvalues could not be obtained accurately for an even number of jets, because of the emergence of the critical layers near the north and the south poles when the zonal flow approaches the marginal stability state. A similar difficulty also arises for an odd number of jets with a negative rotation rate. To obtain the critical eigenvalues and critical rotation rates with sufficient accuracy, we make use of the shooting method and the power series expansion method, taking into account the singular points. As a result, we find that the critical rotation rates of Baines [1] should be corrected by $\sim 10\%$. On the other hand, in the cases of an odd number of jets, the positive critical rotation rates are obtained without difficulty by the spectral method, because of the absence of the critical layers.

So far in this chapter, we have discussed the stability problem of Rossby waves each streamfunction of which is expressed by a single spherical harmonic of Y_l^0 , i.e. zonal flows. In the aforementioned paper, Baines also studied the stability of non-zonal Rossby waves, i.e. ψ_0 proportional to $Y_l^m(\lambda, \mu)$, ($m \neq 0$). However, we have found in high-resolution computations, that some of the stability results for these flows in Baines [1] also suffer from inaccuracy due to the singular point where the coefficient of the highest-order derivative of the eigenfunction vanishes. The traditional technique of bypassing the singular point in the complex plane, which we have employed in this chapter, is applicable only to the problems of space dimension one. Accurate results of the stability eigenvalues for the two-dimensional problem is therefore still open to further study.

Chapter 3

Stability and bifurcation structure of viscous zonal jet flows on a rotating sphere

3.1 Introduction

Two-dimensional incompressible Navier-Stokes turbulence on a rotating sphere has been studied, the planetary atmospheres are considered to be turbulence. Nozawa and Yoden [21] performed numerical simulation with Markovian random forcing, and found that at the final stage of their computation, the flow field consists of multiple zonal jet flow and/or westward circumpolar jets, depending on the Rhines wavenumber and the forcing wavenumber. However, recently, Obuse *et al.* [22] re-calculated the same problem as Nozawa and Yoden with the numerical integration time being more than 100 times of that of Nozawa and Yoden, and found that at an early stage of time integration, multiple zonal jet flow and circumpolar jets are observed, but at the final stage of time integration, only two or three broad zonal jets are left in the flow field. The surviving broad jets are found to be quite *stable* to disturbance even in the ambient turbulent flows.

The zonal flows in planetary atmospheres survives for a long time, and, as seen in the numerical simulation, some zonal flows are robust even in a turbulent environment. These observations lead us to the stability problem of the steady zonal flows on a rotating sphere. In Chapter 2, we and gave correct values of the critical rotation rate obtained by Baines [1] taking into account the singularities. In this chapter we study the stability of *viscous* zonal jets flows on a rotating sphere.

The viscous stability problem of the zonal flows is formulated by introducing a forcing term, which consists of a single spherical harmonics Y_l^0 , to balance with the viscous dissipation term to keep the flow steady. This problem setting is similar to so-called Kolmogorov problem which has been considered as a typical and simplest example to get insight

into the solution properties of the Navier-Stokes equations. On the Kolmogorov problem the flow field exists two-dimensional and double-periodic domain, flat torus, and is governed by the incompressible Navier-Stokes equations with an external sine type force. In our case, on the other hand, the problem is formulated on a two-dimensional sphere, and with the forcing term consisting of a single spherical harmonics function which is an eigenfunction of the Laplacian similar to the forcing term in the Kolmogorov problem. Both the problems are formulated on a two-dimensional boundary-less compact manifold, and are quite similar to each other with a difference in the topology of the flow domain (genus 0 for the sphere, and genus 1 for the torus), and both they are expected to give an insight into the solutions of the Navier-Stokes equations.

For the Kolmogorov problem, Iudovich [13] proofed that two-jet parallel flow on the planar torus is globally stable for any Reynolds number. Kim and Okamoto [14] studied bifurcation structure of steady solutions arising from 4- or 6-jet parallel flows with an assumption of the streamfunctions have origin-point symmetry. They showed that these bifurcating steady solutions have multiple vortices around bifurcation points, however, as Reynolds number increases, multiple vortices merge with each other and one of the steady solutions constructs only one negative vortex and one positive vortex at high Reynolds number. They called these solutions unimodal solutions. Similar phenomena were found also by Okamoto and Shōji [23].

In this chapter, we study stability and bifurcation structure of two-dimensional incompressible viscous zonal flow. The first aim of this chapter is to explain the transition of two-dimensional turbulence on a rotating sphere from multiple zonal jets to quasi-steady zonal jets obtained by Obuse *et al.* [22] utilizing the stability of the steady viscous zonal flows. The second aim is to compare the sphere case and the planar torus case on the bifurcation diagrams and nonlinear steady solutions and study the dependency of the rotation rate on the bifurcation structure of steady solutions. The third aim is to study chaotic solutions at high Reynolds number.

This chapter is constructed as below. In section 3.2, the governing equation and its linearized equation are presented. A global stability of 2-jet zonal flow is shown in section 3.3. In section 3.4 we report linear stability of l -jet zonal flows and compare the stability property of inviscid limit and that of inviscid flow. Section 3.5 shows bifurcation structure of 3-jet zonal flows. Discussion and conclusion follow in section 3.6.

3.2 Governing equations

The two-dimensional incompressible viscous flow on a rotating sphere is governed by the vorticity equation

$$\frac{\partial \Delta \psi}{\partial t} + J(\psi, \Delta \psi) + 2\Omega \frac{\partial \psi}{\partial \lambda} = \frac{1}{R} \{(\Delta + 2) \Delta \psi + (l(l+1) - 2) Y_l^0(\mu)\}, \quad (3.1)$$

where quantities are made non-dimensional and the radius of the sphere is unity. Here t is the time, λ and μ the longitude and the sine latitude $\mu = \sin \phi$ where ϕ is the latitude, ψ the streamfunction and $\Delta\psi = \zeta$ the vorticity, where Δ is the horizontal Laplacian on the unit sphere. The longitudinal and latitudinal components of velocity (u_λ, u_μ) are given by $u_\lambda = -\sqrt{1-\mu^2}(\partial\psi/\partial\mu)$ and $u_\mu = 1/\sqrt{1-\mu^2}(\partial\psi/\partial\lambda)$. R and Ω are the Reynolds number and a non-dimensional rotation rate of the sphere, respectively, $J(A, B) := (\partial A/\partial\lambda)(\partial B/\partial\mu) - (\partial A/\partial\mu)(\partial B/\partial\lambda)$ the Jacobian and $(l(l+1)-2)Y_l^0(\mu)/R$ the vorticity forcing where $Y_l^m(\lambda, \mu)$ is a 4π normalized spherical harmonics with total wavenumber l and azimuthal wavenumber m . The term of $2\Delta\psi/R$ in the viscosity term is necessary for the conservation of the total angular momentum of the system[29].

The vorticity equation (3.1) has a steady l -jet zonal flow solution for any Reynolds number and any rotation rate, expressed by

$$\psi_0(\mu) = -\frac{1}{l(l+1)}Y_l^0(\mu), \quad \zeta_0(\mu) = Y_l^0(\mu), \quad (3.2)$$

Here, the number of jets is defined as the number of extreme points of the longitudinal velocity, which is equivalent to the number of nodes of the latitudinal distribution of streamfunction. We note that Kolmogorov problem on a planar torus deals with bifurcated solutions from $2n$ -jet parallel flow solutions $-\cos(ny)/n^2$ driven by vorticity forcing $n^2 \cos ny/R$. The trigonometric functions $\cos ny$ are the eigenfunction of Laplacian on the planar torus while the spherical harmonics $Y_l^0(\mu)$ are the eigenfunction of Laplacian on the sphere. This problem setting is therefore similar to Kolmogorov problem.

The linear stability of the l -jet zonal flow $\psi_0(\mu)$ is given by substituting $\psi = \psi_0(\mu) + \hat{\psi}(\mu)e^{im(\lambda-ct)}$ into the equation (3.1) and neglecting the second order terms,

$$\{U(\mu) - c\} \Delta_m \hat{\psi} + \left\{ 2\Omega - \frac{d^2}{d\mu^2} [(1-\mu^2)U(\mu)] \right\} \hat{\psi} = \frac{1}{imR} (\Delta_m + 2) \Delta_m \hat{\psi}. \quad (3.3)$$

Here, $U(\mu) = -d\psi_0(\mu)/d\mu$ is the angular velocity of the l -jet zonal flow and Δ_m is defined as,

$$\Delta_m = \frac{d}{d\mu}(1-\mu^2)\frac{d}{d\mu} - \frac{m^2}{1-\mu^2}.$$

The solution is continuous on the entire sphere, and therefore satisfies

$$\hat{\psi}(\mu) \sim (1 \mp \mu)^{\frac{m}{2}} \quad (\mu \rightarrow \pm 1), \quad (3.4)$$

which is actually the boundary condition for $\hat{\psi}(\mu)$. The equations (3.3) and (3.4) constitute an eigenvalue problem with respect to the eigenfunction $\hat{\psi}(\mu)$ and the eigenvalue $c = c_r + ic_i$ ($c_r, c_i \in \mathbb{R}$) being the complex angular phase velocity. The equation (3.3) is invariant by the transformation $m \rightarrow -m, \psi \rightarrow \psi^*, c \rightarrow c^*$, where \cdot^* indicates complex conjugate. If

$U(\mu)$ is even function as in the case of odd l the eigenfunction $\hat{\psi}(\mu)$ have anti-/symmetry, because the equation (3.3) is invariant by the transformation $\mu \rightarrow -\mu$. On the other hand, if $U(\mu)$ is odd as in the case of even l , the equation (3.3) is invariant by the transformation $\Omega \rightarrow -\Omega, \psi \rightarrow \psi^*, \mu \rightarrow -\mu, c \rightarrow -c^*$.

3.3 Global stability of 2-jet zonal flow

1-jet zonal flow ($l = 1$) is stable due to the conservation of total angular velocity. As we will show below, 2-jet zonal flow is globally asymptotic stable for any Reynolds number and rotation rate. In this section, $C_i (i = 1, \dots, 5)$ indicate constants corresponding to an initial condition of disturbance.

Theorem

2-jet zonal flow is globally asymptotic stable for any R and Ω .

Proof

Substituting $\psi(\lambda, \mu, t) := AY_2^0(\mu) + \tilde{\psi}(\lambda, \mu, t)$ into the equation (3.1), where $A = -1/6$, leads to

$$\partial_t \Delta \tilde{\psi} + J(AY_2^0, (\Delta + 6)\tilde{\psi}) + 2\Omega \partial_\lambda \tilde{\psi} + J(\tilde{\psi}, \Delta \tilde{\psi}) - \frac{1}{R}(\Delta + 2)\Delta \tilde{\psi} = 0. \quad (3.5)$$

The $\tilde{\cdot}$ is omitted below. Considering inner product with ψ and $\Delta\psi$, we obtain

$$\frac{1}{2} \partial_t \|\nabla \psi\|^2 + \frac{1}{R} (\|\Delta \psi\|^2 - 2\|\nabla \psi\|^2) + \int \psi A (\partial_\mu Y_2^0) (\Delta \partial_\lambda \psi) = 0, \quad (3.6)$$

$$\frac{1}{2} \partial_t \|\Delta \psi\|^2 + \frac{1}{R} (\|\nabla \Delta \psi\|^2 - 2\|\Delta \psi\|^2) + 6 \int \psi A (\partial_\mu Y_2^0) (\Delta \partial_\lambda \psi) = 0. \quad (3.7)$$

Here we use the periodic boundary condition of λ and

$$\int J(f, g)h = \int fJ(g, h). \quad (3.8)$$

The $\|\cdot\|$ is defined as

$$\|f(\lambda, \mu)\|^2 := \int dS f^2(\lambda, \mu) = \int_{-1}^1 d\mu \int_0^{2\pi} d\lambda f^2(\lambda, \mu). \quad (3.9)$$

The equations (3.6) and (3.7) yield

$$\begin{aligned} & \partial_t \left\{ \frac{1}{2} \left(\frac{1}{6} \|\Delta \psi\|^2 - \|\nabla \psi\|^2 \right) \right\} \\ & + \frac{1}{R} \left\{ \frac{1}{6} \|\nabla \Delta \psi\|^2 - \|\Delta \psi\|^2 \right\} - \frac{2}{R} \left\{ \frac{1}{6} \|\Delta \psi\|^2 - \|\nabla \psi\|^2 \right\} = 0 \end{aligned} \quad (3.10)$$

We split the disturbance ψ into ψ_2 and ψ_{rest} defined as

$$\psi_2 = \sum_m \psi_2^m(t) Y_2^m(\lambda, \mu), \quad \psi_{rest} = \sum_{n \geq 3, m} \psi_n^m(t) Y_n^m(\lambda, \mu).$$

Substituting $\psi(\lambda, \mu, t) = \psi_2 + \psi_{rest}$ into the equation (3.10), we obtain

$$\begin{aligned} & \partial_t \left\{ \frac{1}{2} \left(\frac{1}{6} \|\Delta \psi_{rest}\|^2 - \|\nabla \psi_{rest}\|^2 \right) \right\} \\ & + \frac{1}{R} \left\{ \frac{1}{6} \|\nabla \Delta \psi_{rest}\|^2 - \|\Delta \psi_{rest}\|^2 \right\} - \frac{2}{R} \left\{ \frac{1}{6} \|\Delta \psi_{rest}\|^2 - \|\nabla \psi_{rest}\|^2 \right\} = 0. \end{aligned} \quad (3.11)$$

The second term of the equation (3.11) can be evaluated

$$\begin{aligned} \frac{1}{6} \|\nabla \Delta \psi_{rest}\|^2 - \|\Delta \psi_{rest}\|^2 & \geq 12 \sum_{n \geq 3, m} n(n+1) \left(\frac{n(n+1)}{6} - 1 \right) |\psi_n^m|^2 \\ & = 12 \left(\frac{1}{6} \|\Delta \psi_{rest}\|^2 - \|\nabla \psi_{rest}\|^2 \right), \end{aligned} \quad (3.12)$$

then we obtain

$$\frac{1}{6} \|\Delta \psi_{rest}\|^2 - \|\nabla \psi_{rest}\|^2 \leq C_0 \exp\left(-\frac{20}{R}t\right). \quad (3.13)$$

Considering an obvious inequality

$$\|\Delta \psi_{rest}\|^2 \geq 12 \|\nabla \psi_{rest}\|^2 \geq 12^2 \|\psi_{rest}\|^2, \quad (3.14)$$

leads to

$$\|\psi_{rest}\| \leq C_1 \exp\left(-\frac{10}{R}t\right), \quad (3.15)$$

Next, taking an inner product between ψ_2 and the equation (3.5) we obtain

$$\partial_t \|\psi_2\| + \frac{8}{R} \|\psi_2\| = \frac{1}{3} \left\{ \int \frac{\psi_2}{\|\psi_2\|} J(AY_2^0, (\Delta + 6)\psi_{rest}) + \int \frac{\psi_2}{\|\psi_2\|} J(\psi_{rest}, \Delta \psi_{rest}) \right\}. \quad (3.16)$$

The first term of right hand side of the equation (3.16) can be evaluated

$$\begin{aligned} \left| \int \frac{\psi_2}{\|\psi_2\|} J(AY_2^0, (\Delta + 6)\psi_{rest}) \right| & \leq \left| \int \frac{1}{\|\psi_2\|} J(\psi_2, AY_2^0) \Delta \psi_{rest} \right| + 6 \left| \int \frac{1}{\|\psi_2\|} \psi_2 J(AY_2^0, \psi_{rest}) \right| \\ & \leq \frac{1}{\|\psi_2\|} \|\nabla \psi_2 \times \nabla AY_2^0\| \cdot \|\Delta \psi_{rest}\| \\ & \quad + 6 \frac{1}{\|\psi_2\|} \|\psi_2\| \cdot \|\nabla AY_2^0 \times \nabla \psi_{rest}\| \\ & \leq \|A \nabla Y_2^0\| (\sqrt{6} \|\Delta \psi_{rest}\| + 6 \|\nabla \psi_{rest}\|) \\ & \leq C_2 \exp\left(-\frac{10}{R}t\right), \end{aligned} \quad (3.17)$$

and the second term of right hand side of the equation (3.16) can be also

$$\begin{aligned} \left| \int \frac{\psi_2}{\|\psi_2\|} J(\psi_{rest}, \Delta\psi_{rest}) \right| &\leq \frac{1}{\|\psi_2\|} \|\nabla\psi_2 \times \nabla\psi_{rest}\| \cdot \|\Delta\psi_{rest}\| \\ &\leq \sqrt{6} \|\nabla\psi_{rest}\| \cdot \|\Delta\psi_{rest}\| \\ &\leq C_3 \exp\left(-\frac{20}{R}t\right), \end{aligned} \quad (3.18)$$

here we use the Cauchy-Schwartz inequality and the equation (3.15). Therefore,

$$\partial_t \|\psi_2\| + \frac{8}{R} \|\psi_2\| \leq C_4 \exp\left(-\frac{10}{R}t\right). \quad (3.19)$$

Finally the estimation of the disturbance $\psi = \psi_2 + \psi_{rest}$ is given by

$$\|\psi(t)\| \leq C_5 \exp\left(-\frac{8}{R}t\right) \quad \text{then} \quad \psi(t) \rightarrow 0 \quad (t \rightarrow +\infty), \quad (3.20)$$

Therefore, we can conclude that 2-jet zonal flow is globally asymptotic stable for any Reynolds number and the rotation rate. \square

3.4 Linear stability of the l -jet zonal flows

Then, we investigate l -jet zonal flows with $3 \leq l \leq 9$, where the same range of l as the study of stability of inviscid l -jet zonal flows[28]. It can be proved that the unstable modes of l -jet zonal flows do not contain the spherical harmonics $Y_n^m(\lambda, \mu)$ with $m \geq l$ by extending the proof of the inviscid case[12]. Also, the zonal modes $Y_l^0(\mu)$ are all stable modes. Therefore, it is sufficient to study disturbances with the azimuthal wavenumber $1 \leq m \leq l-1$. In order to solve the eigenvalue problem of (3.3) and (3.4) for a given azimuthal wavenumber m , we employ the spectral method as same as chapter 2. The streamfunction $\hat{\psi}$ is expressed by

$$\hat{\psi}(\mu) = \sum_{n=m}^N \psi_n^m P_n^m(\mu),$$

where ψ_n^m are the expansion coefficients and N is the truncation wavenumber. Note that the boundary condition (3.4) is satisfied by the associated Legendre functions. On evaluating the terms $U(\mu)\Delta_m\hat{\psi}$ and $\left\{2\Omega - \frac{d^2}{d\mu^2} [(1-\mu^2)U(\mu)]\right\}\hat{\psi}$ in (3.3), we adopt the transform method, employing in the physical space the numbers of longitudinal and latitudinal grid points I and J satisfying $I \geq 3N+1$ and $J > 3N/2$ in order to eliminate aliasing errors. We have checked the accuracy by changing the truncation wavenumber up to 213.

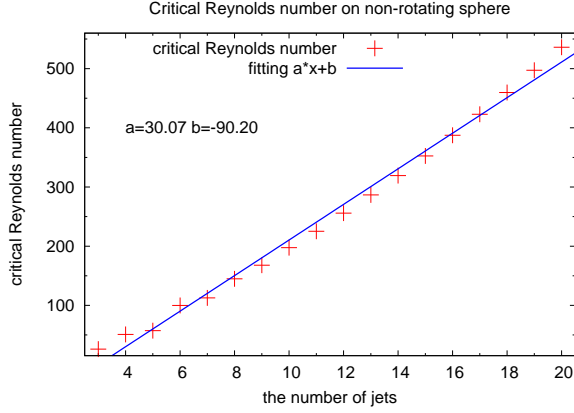


Figure 3.1: The critical Reynolds number of l -jet zonal flow in the non-rotating case. The horizontal and vertical axes indicate the number of jets and critical Reynolds number, respectively. The red cross and blue line denote the critical Reynolds number and fitting line given by least-square method, respectively.

Figure 3.1 shows the critical Reynolds numbers of l -jet zonal flow R_c^0 in the non-rotation case, $\Omega = 0$, as a function of the number of jets l . We find that, as the number of jets increases, the critical Reynolds number increases monotonically where each l -jet zonal flow is Hopf unstable at its critical point the critical azimuthal wavenumbers are $m_c = 2$.

Figure 3.2 shows the neutral curves of the 3- and the 4-jet zonal flow in the rotating cases together with the real part of phase angular velocity of the critical modes. Note that the 3-jet zonal flow is symmetric with respect to the equator, while the 4-jet zonal flow is anti-symmetric. As the rotation rate increases, the real part of angular phase velocities of neutral mode decrease monotonically from positive to negative values, i.e. the direction of the propagation of the marginal mode changes from eastward to westward. In the case of the 3-jet zonal flow, we have smooth the marginal mode is given by modes of $m = 1$ and 2 depending on the rotation rate Ω , and the neutral curves of these modes are not an even function of Ω , which reflects the fact that the 3-jet zonal flow does not have the west-east symmetry even if the transformation $\mu \rightarrow -\mu$ is taken into account. On the other hand, in the case of the 4-jet zonal flow, the neutral curves are even functions of Ω , but has a discontinuity of the first derivative at $\Omega = 0$ for $m = 1$ and 2, while the neutral curve is smooth at $\Omega = 0$ for $m = 3$. This phenomenon is related to the symmetry of the linearized equation (3.3), where $(-\Omega, \psi^*, -\mu, -c^*)$ gives a solution if (Ω, ψ, μ, c) is a solution. This symmetry means that the neutral curves are all even function of Ω . It also suggests that, the neutral curve is smooth if $\psi(\mu) = \psi^*(-\mu)$ and $c = -c^*$ hold at $\Omega = 0$, while the neutral curve has a cusp if $\psi(\mu) \neq \psi^*(-\mu)$ or $c \neq -c^*$ at $\Omega = 0$. Actually we can confirm numerically that the neutral mode for $m = 3$ has the real phase angular velocity c and satisfies $\psi(\mu) = \psi^*(-\mu)$ at $\Omega = 0$, while those for $m = 1$ and 2 do not. We note that as far as we calculated (Table

3.1), similar discontinuity of the first derivative of the neutral curve is found for the zonal flow with the even number of jets anti-symmetric with respect to the equator.

We find in Figure 3.2 and Table 3.1 that the critical Reynolds number takes its lowest value at non-zero rotation rate; at a small negative rotation rate for the 3-jet zonal flow, and at a small positive rotation rate for the 4-jet zonal flow, while the critical azimuthal wavenumber m at $R = R_c^{\text{low}}$ is 2 in all the cases we have calculated. Table 3.1 also shows that the difference between the lowest critical Reynolds number R_c^{low} and the critical Reynolds number R_c^0 in the non-rotating case becomes large as the number of jets increases. We also note that Ω_c^{low} is negative for the zonal flows with an odd number of jets, while both the signs are possible for Ω_c^{low} because of the symmetry described above. This means that the effect of small rotation is not always the stabilization of the zonal flows, while the zonal flows are stabilized by the large rotation rates and appears linearly stable at an arbitrary Reynolds numbers for $\Omega < -5.726$ and $2.171 < \Omega$ for the 3-jet flow, and for $9.750 < |\Omega|$ for the 4-jet flow.

# jets	R_c^{low}	Ω_c^{low}	m_c^{low}	R_c^0	m_c^0
3	26.085	-0.1085	2	26.123	2
4	45.957	± 0.7321	2	50.886	2
5	46.721	-0.8488	2	57.263	2
6	71.067	± 0.6549	2	99.824	2
7	75.914	-0.6662	2	112.62	2
8	105.72	± 0.6101	2	144.82	2
9	111.81	-0.6275	2	167.91	2

Table 3.1: The lowest critical Reynolds number of l -jet zonal flow. The first column shows the number of jets l . The second to fourth columns show respectively the lowest critical Reynolds number R_c^{low} , the rotation rate Ω_c^{low} and the azimuthal wavenumber m_c^{low} at R_c^{low} . The fifth and sixth columns show the critical Reynolds number R_c^0 and the critical azimuthal wavenumber m_c^0 at R_c^0 in the non-rotating case.

Considering the inflection point theorem (see Chapter 2) stabilization by rotation effect is unsurprising fact. On the 3-jet zonal flow, we find the critical rotation rate $\Omega_c^+ = 2.17169$ and $\Omega_c^- = -5.72700$ at which the 3-jet zonal flow is stable for $R \leq 10^6$. On the other hand, the critical rotation rates of *inviscid* 3-jet zonal flow are $\Omega_c^{E+} = 1.7719 (< \Omega_c^+)$, $\Omega_c^{E-} = -5.4568 (> \Omega_c^-)$ (see Chapter 2 and [28]). The unstable region of the rotation rate for *inviscid* zonal flows is smaller than that for the *viscous* zonal flows. This seeming contradiction of critical rotation rates between inviscid limit and inviscid cases is resolved as below. Figure 3.3 shows the growth rate mc_i of the most unstable mode on the R - Ω plane. In the regions where the inviscid zonal flow is stable while the viscous zonal flow is unstable ($\Omega_c^{E+} < \Omega < \Omega_c^+$ and $\Omega_c^{E-} > \Omega > \Omega_c^-$), the growth rate converges to zero as the Reynolds

3 Stability and bifurcation structure of viscous zonal jet flows on a rotating sphere

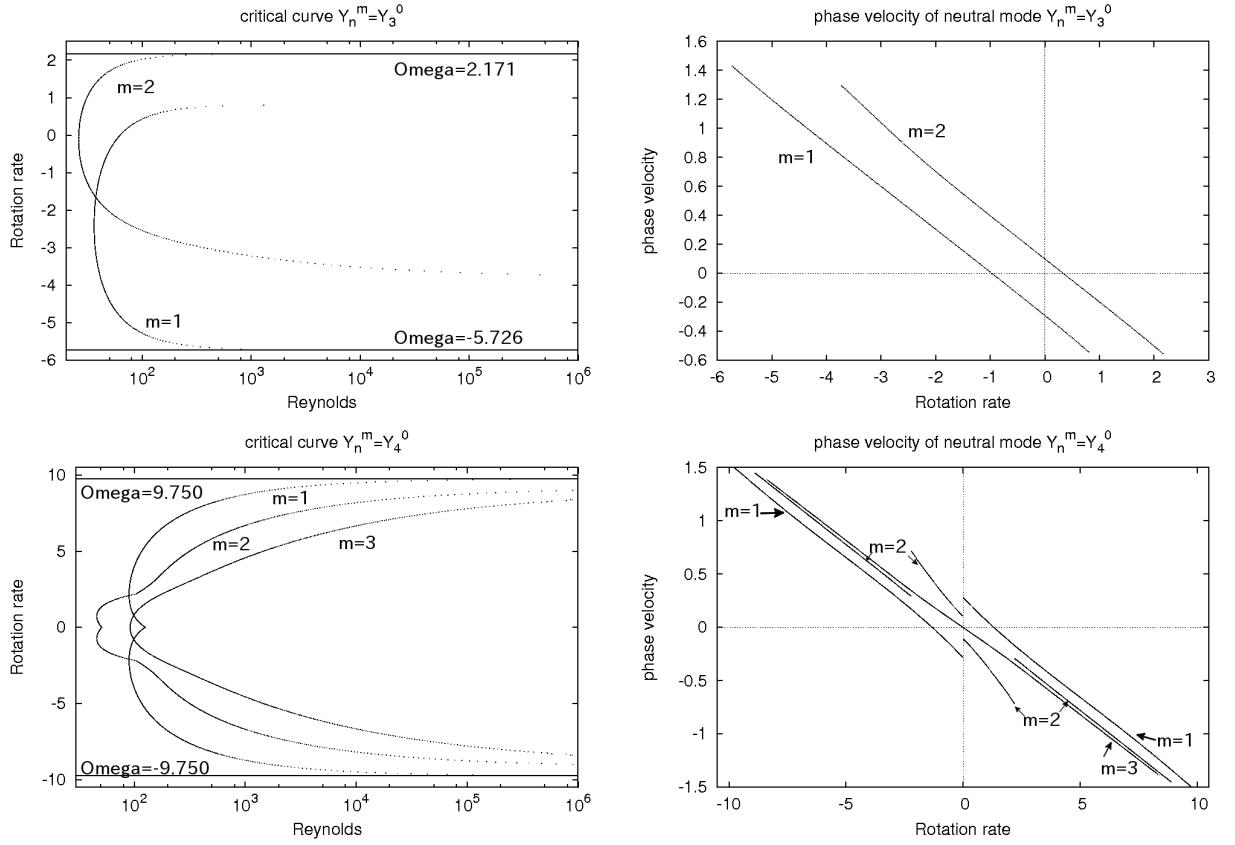


Figure 3.2: The neutral curves and real part of angular phase velocity of the critical mode in the cases of 3-jet (top) and 4-jet (bottom) profiles. The left and right columns show the neutral curves and real part of angular phase velocity, respectively. In the left figures, the horizontal and vertical axes indicate Reynolds number R in log scale and the rotation rate Ω , respectively. In the right figures, the horizontal and vertical axes indicate Ω and the real part of angular phase velocity c_r , respectively.

number increases, and the stability properties for the inviscid limit becomes consistent with that for inviscid case.

Table 3.2 shows the critical rotation rate of the l -jet zonal flows. When the number of jets is odd, the unstable region of the rotation rate for viscous zonal flows is greater than that for inviscid zonal flows. In this case, the growth rates of most unstable modes converge to zero as the Reynolds number increases in the regions where inviscid zonal flows are stable but viscous zonal flows are unstable, similar to 3-jet zonal flow case. On the other hand, when the number of jets is even, the absolute value of critical rotation rates of viscous zonal flows are smaller than that of inviscid zonal flows. We find that as the Reynolds number increases the absolute values of the rotation rates, where the even-jet zonal flow losses the stability increases monotonically but less than the critical rotation rate of inviscid zonal flow. We expect that the inviscid limit of the viscous critical rotation rate coincides with the inviscid critical rotation rate when the number of jets is even.

# jets	Ω_c^\pm	m_c^\pm	$\Omega_c^{E\pm}$	$m_c^{E\pm}$
3	-5.72700	1	-5.4568	1
	2.17169	2	1.7719	2
4	-9.750	1	-9.7700	1
	9.750	1	9.7700	1
5	-19.44	1	-19.22	1
	4.494	3	4.022	3
6	-28.37	1	28.389	1
	28.37	1	28.389	1
7	-44.77	1	-44.445	1
	8.617	3	7.8929	3
8	-59.58	1	-59.618	1
	59.58	1	59.618	1
9	-83.79	1	-83.340	1
	14.73	3	13.665	3

Table 3.2: The critical rotation rates of viscous zonal flows. Column 1 shows the number of jets l of the basic flows. Column 2 and 3 show the critical rotation rate of the viscous zonal flows Ω_c^\pm and the critical azimuthal wavenumbers m_c^\pm , respectively. Column 4 and 5 shows the critical rotation rate of the inviscid zonal flows $\Omega_c^{E\pm}$ and the critical azimuthal wavenumbers $m_c^{E\pm}$, respectively, which is already shown in Chapter 2.

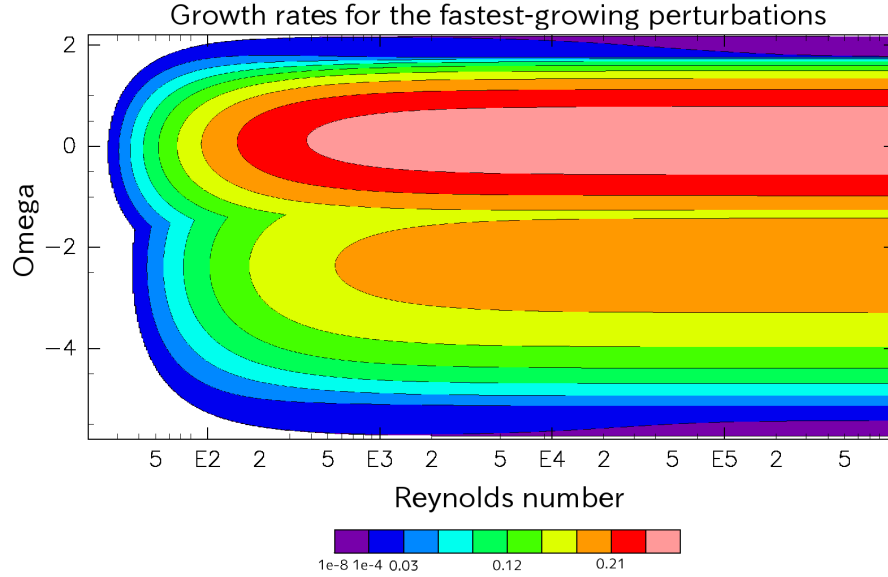


Figure 3.3: Growth rates for the fastest-growing perturbations. The horizontal and vertical axes indicate the Reynolds number and the rotation rate, respectively. The contour shows growth rate of most unstable perturbation. The white region indicates that the 3-jet zonal flow is linearly stable.

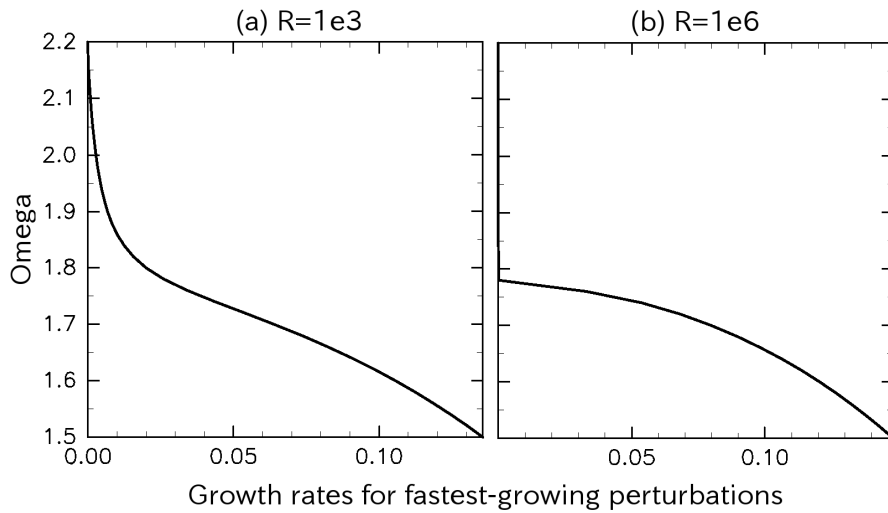


Figure 3.4: The growth rates for the fastest-growing perturbations at $1.5 \leq \Omega \leq 2.2$. The left and right figures show growth rates of most unstable perturbation at $R = 10^3$ and $R = 10^6$, respectively. The horizontal and vertical axes indicate the growth rate mc_i and the rotation rate, respectively.

3.5 Bifurcation structure of nonlinear steady solutions arising from 3-jet zonal flow

In this section we show bifurcation diagrams of nonlinear steady solutions arising from 3-jet zonal flow. Figure 3.5 shows the streamfunction and the longitudinal velocity of 3-jet zonal flow. As below we call this flow the trivial solution.

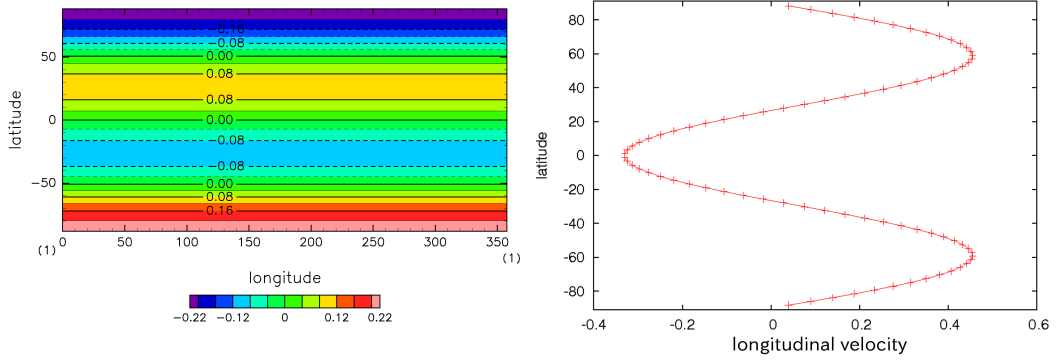


Figure 3.5: The 3-jet zonal flow. The left and right figure show the streamfunction and longitudinal velocity, respectively. In left figure, the horizontal and vertical axes indicate the longitude and the latitude, respectively. In right figure, the horizontal and vertical axes indicate the longitudinal velocity and the latitude, respectively.

In order to solve the problem numerically, we employ the spectral method which is the same as before section but the streamfunction ψ is expressed by

$$\psi(\lambda, \mu) = \sum_{n=1}^N \sum_{m=-n}^n \psi_n^m Y_n^m(\lambda, \mu),$$

where ψ_n^m are the expansion coefficient and N is the truncation wavenumber. By use of Newton method we seek to nonlinear steady solutions $R \leq 10^6$. The stopping condition of the Newton method is that, if $R < 10^3$, the maximum absolute value of correction of the real/imaginary part of the spectral components is less than 10^{-8} , and if $R \leq 10^3$ that is less than 10^{-12} . We have checked the accuracy by changing the truncation wavenumber upto $N = 170$. We seek nonlinear steady solutions arising from trivial solution at $\Omega_c^- < -5.6 \leq \Omega \leq 2.1 < \Omega_c^+$ and study stability of the nonlinear solutions until $R = 10^4$. Moreover, when $\Omega = 0, \pm 0.5, \pm 1.0$ we find nonlinear steady solutions the bifurcation points of which exist in $0 < R \leq 10^4$ and the branches of which finally link to trivial solution along the steady solution branches.

3.5.1 Bifurcation diagram in the non-rotating case

The nonlinear steady solutions arising from the trivial solution are *Traveling Wave* solutions through Hopf bifurcation at the critical Reynolds number of the trivial solution where the trivial solution becomes Hopf unstable (see Section 3.4). Furthermore, all nonlinear steady solutions which we find numerically are traveling wave solutions. Therefore we call these solutions as TW with serial characters.

We find that TW1 ($m = 2$) bifurcates from trivial solution at $R = 26.123$ through the super-critical Hopf bifurcation. Figure 3.6 shows bifurcation diagram. Tracing TW1 branch, we find two secondary pitchfork bifurcation points. At $R = 70.66$, where TW1 loses the stability, TW2-N and TW2-S bifurcate through the pitchfork bifurcation. We find that TW2-N has two negative vortices at the mid-latitudes in the *northern* hemisphere, TW2-S has two positive vortices at the mid latitudes in the *southern* hemisphere, and the TW2-N and TW2-S are antisymmetric with respect to the equator. Notice that -N and -S indicate the hemisphere where the solution has large vortices. As the Reynolds number increases, TW2-N and TW2-S become Hopf unstable at $R = 103.2$. On TW1 branch we find that, as the Reynolds number increases, TW1 becomes stable again at $R = 203.8$ where TW3-N and TW3-S bifurcate through the pitchfork bifurcation. We confirm that TW3-N and TW3-S are Hopf unstable for $203.8 \leq R \leq 10^4$. TW1 becomes Hopf unstable again at $R = 249.4$. On the TW3-N we find that TW6-N bifurcates at $R = 2687$ through the pitchfork bifurcation. TW6-N is a single branch because the another pitchfork bifurcation branch is longitudinal translated TW6-N. We also find that TW6-S bifurcate from TW3-S at the same Reynolds number ($R = 2687$) through the pitchfork bifurcation. We confirm that TW6-N and TW6-S are Hopf unstable for $2687 \leq R \leq 10^4$. On the trivial solution we find that TW4 ($m=1$) bifurcates at $R = 62.51$ through Hopf bifurcation (see also figure 3.2), and TW4 is Hopf unstable for $62.5 \leq R \leq 10^4$. On TW4 branch, we find that TW5-N and TW5-S bifurcate at $R = 136.2$ through the pitchfork bifurcation, and TW5-N and -S are Hopf unstable except for the interval $143.5 \leq R \leq 161.9$, both ends of which are considered to be associated with bifurcations of time-periodic solutions.

All secondary bifurcation points which we can find are pitchfork and all the nonlinear steady solutions become Hopf unstable until at $R = 249.4$. Finally we note that, as Reynolds number increases, the absolute values of phase velocity of the nonlinear solutions decrease monotonically.

3.5.2 Bifurcation diagrams in the rotating case

First we seek only supercritical bifurcating branches arising at critical Reynolds number of trivial/steady traveling solutions. Figure 3.7 shows stable regions of these nonlinear solutions on R - Ω plane. In the figure 3.7 white regions indicate Hopf unstable regions of these nonlinear solutions. As the rotation rate increases sufficiently large, critical Reynolds number of nonlinear solutions increases, *i.e.*, the large rotation effect makes nonlinear steady

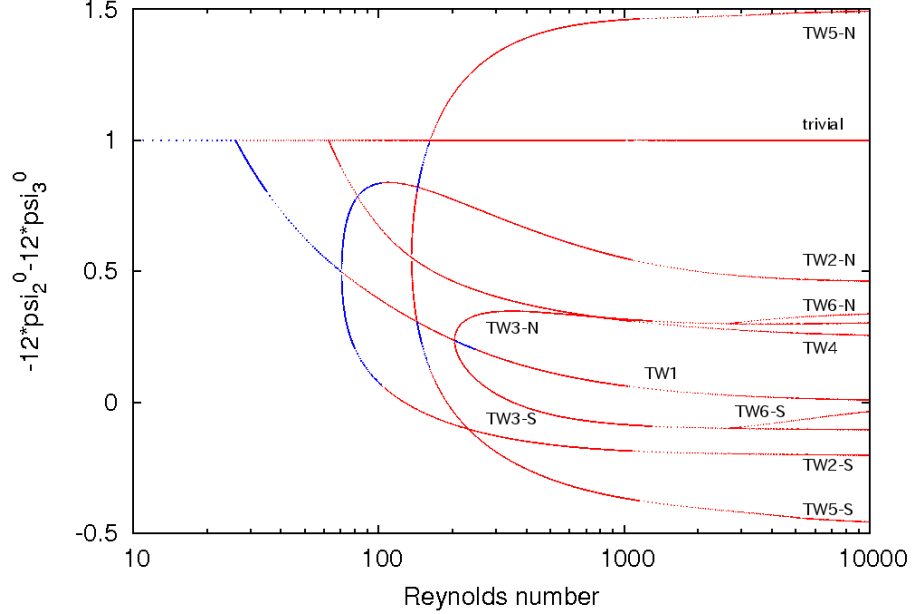


Figure 3.6: Bifurcation diagram in the non-rotating case, $\Omega = 0$. Blue asterisks and red crosses denote that the solutions are stable and unstable, respectively. The horizontal and vertical axes indicate Reynolds number and $-12\psi_2^0 - 12\psi_3^0$, respectively. Note is that the horizontal axis is Log-scale in order to describe all bifurcation points.

solutions stable similar to zonal jet flows. At $\Omega = \pm 0.5, \pm 1.0$ we seek steady traveling solutions which bifurcate until $R = 10^4$.

In the case of $\Omega < 0$, the properties of the bifurcation diagrams are so different from the non-rotating case. Figure 3.8 top shows the bifurcation diagram at $\Omega = -0.5$. We find that as Reynolds number increases the trivial solution become Hopf unstable at $R = 26.58$ where TW1 ($m = 2$) bifurcates through the super-critical Hopf bifurcation. As the Reynolds number further increases TW1 become Hopf unstable at $R = 81.08$. On the trivial solution we find a another Hopf bifurcation point at $R = 48.15$ where TW4 ($m = 1$) bifurcates. We confirm that TW4 is Hopf unstable for $48.15 \leq R \leq 10^4$. On TW4 branch we find two secondary pitchfork bifurcation points at $R = 98.57$ and $R = 3099$. At $R = 98.57$, TW5-N and TW5-S bifurcating, are Hopf unstable for $98.57 \leq R \leq 10^4$. As Reynolds number increases the growth rate of a steady unstable mode of TW4 (no-Hopf mode) becomes positive to negative at $R = 3099$, where TW6-N and TW6-S bifurcate. Tracing TW6-N and TW6-S with Reynolds number decreasing, we find saddle-node bifurcation points at $R = 299.517$ where the growth rate of steady modes of TW6-N and TW6-S become negative to zero. The TW6-N and TW6-S branches which connect to TW4 with no bifurcation points are *Node* branches while the branches arising from the saddle-node bifurcation points at $R = 299.517$ are *Saddle* solutions. Note is that TW6-N and TW6-S are Hopf unstable except for the

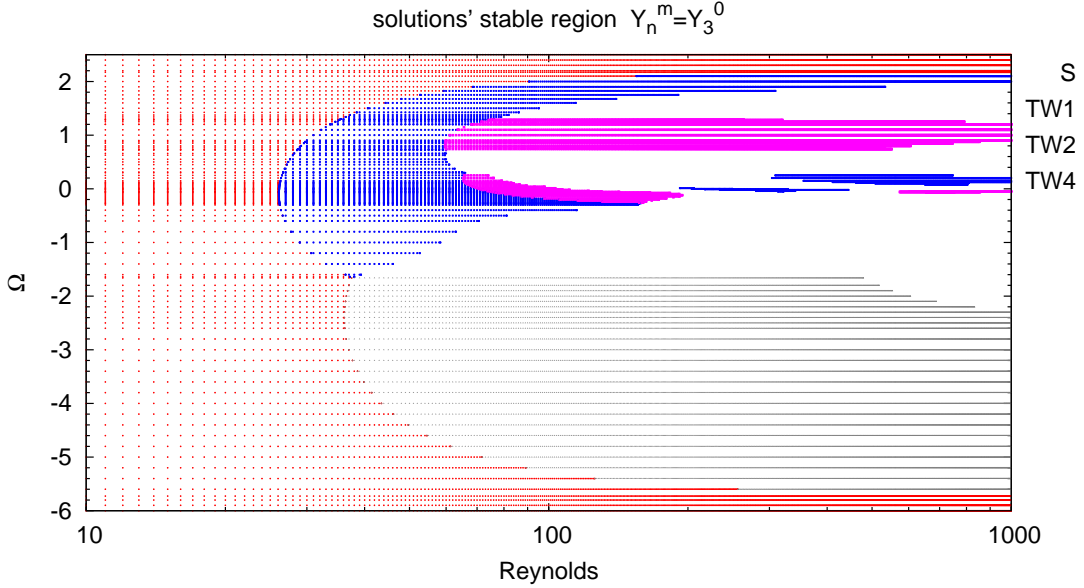


Figure 3.7: Stable regions of nonlinear solutions. The horizontal and vertical axes indicate Reynolds number and rotation rate, respectively. The red cross, the blue asterisk, the purple square and the gray triangle indicate stable regions of trivial solution, TW1, TW2-N (-S) and TW4, respectively. The white regions indicate Hopf unstable regions of trivial solution, TW1, TW2-N (-S) and TW4.

interval $2175 \leq R \leq 2509$, both ends of which are considered to be associated with the bifurcations of time-periodic solutions.

Figure 3.8 bottom shows the bifurcation diagram in the case of $\Omega = -1.0$. We find that as the Reynolds number increases the trivial solution become Hopf unstable at $R = 28.94$ where TW1 ($m = 2$) bifurcates through the super-critical Hopf bifurcation. As the Reynolds number increases TW1 become Hopf unstable at $R = 58.29$. On the trivial solution branches we find that the another Hopf bifurcation point at $R = 41.57$ where TW4 bifurcates. Tracing TW4 branches we find two saddle-node bifurcation points at $R = 540.05$ and 475.33 . Tracing TW4 branch from $R = 41.57$, TW4 obtain the stability at the second saddle-node point $R = 475.33$. On TW4 branches we find three pitchfork bifurcation points at $R = 95.72, 274.5$ and 542.4 , respectively. The two branches arising at the first pitchfork bifurcation point $R = 95.72$ connect to TW4 at the second pitchfork bifurcation point $R = 274.5$. As a result these two branches construct a closed loop. On the third pitchfork bifurcation point $R = 542.4$ we find that TW4 losses stability at this Reynolds number where TW5-N and TW5-S bifurcate. As the Reynolds number increases TW5-N and TW5-S become Hopf unstable at $R = 614.4$.

Figure 3.9 (top) shows the bifurcation diagram in the case of $\Omega = 0.5$. We find that as the Reynolds number increases the trivial solution becomes Hopf unstable at $R = 27.35$

where TW1 bifurcates through the super-critical Hopf bifurcation. Tracing TW1 branch, we find that TW1 becomes Hopf unstable at $R = 60.16$, and a pitchfork bifurcation point at $R = 63.46$ where TW2-N and TW2-S bifurcate and TW2-N and TW2-S are Hopf unstable except for the interval $64.918 \leq R \leq 85.036$. On the trivial solution we find another Hopf bifurcation point at $R = 113.7$, where TW4 bifurcates. We confirm that TW4 is also Hopf unstable for $113.7 \leq R \leq 10^4$. As the Reynolds number increases we find that TW5-N and TW5-S bifurcate from TW4 at $R = 983.6$ through the pitchfork bifurcation and TW5-N and TW5-S are also Hopf unstable for $983.6 \leq R \leq 10^4$.

Figure 3.9 (bottom) shows the bifurcation diagram in the case of $\Omega = 1.0$. We find that as the Reynolds number increases the trivial solution becomes Hopf unstable at $R = 31.00$ where TW1 bifurcates through the super-critical Hopf bifurcation. As the Reynolds number increases TW1 become unstable at $R = 61.11$ where TW2-N and TW2-S bifurcate through the pitchfork bifurcation. We confirm that TW2-N and TW2-S is stable for $61.11 \leq R \leq 10^4$ and there is no bifurcation point on trivial solution.

Under the stabilizing effect of rotation, as the absolute value of the rotation rate increases, the number of nonlinear steady traveling solutions at high Reynolds number decreases monotonically. In the case of $\Omega < 0$ we find the saddle-node bifurcation points and a closed loop branch, while in the case of $\Omega > 0$ the secondary bifurcation branches arise only through the pitchfork bifurcation. These results show that the bifurcation structure changes drastically, as the absolute value of the rotation rate increases.

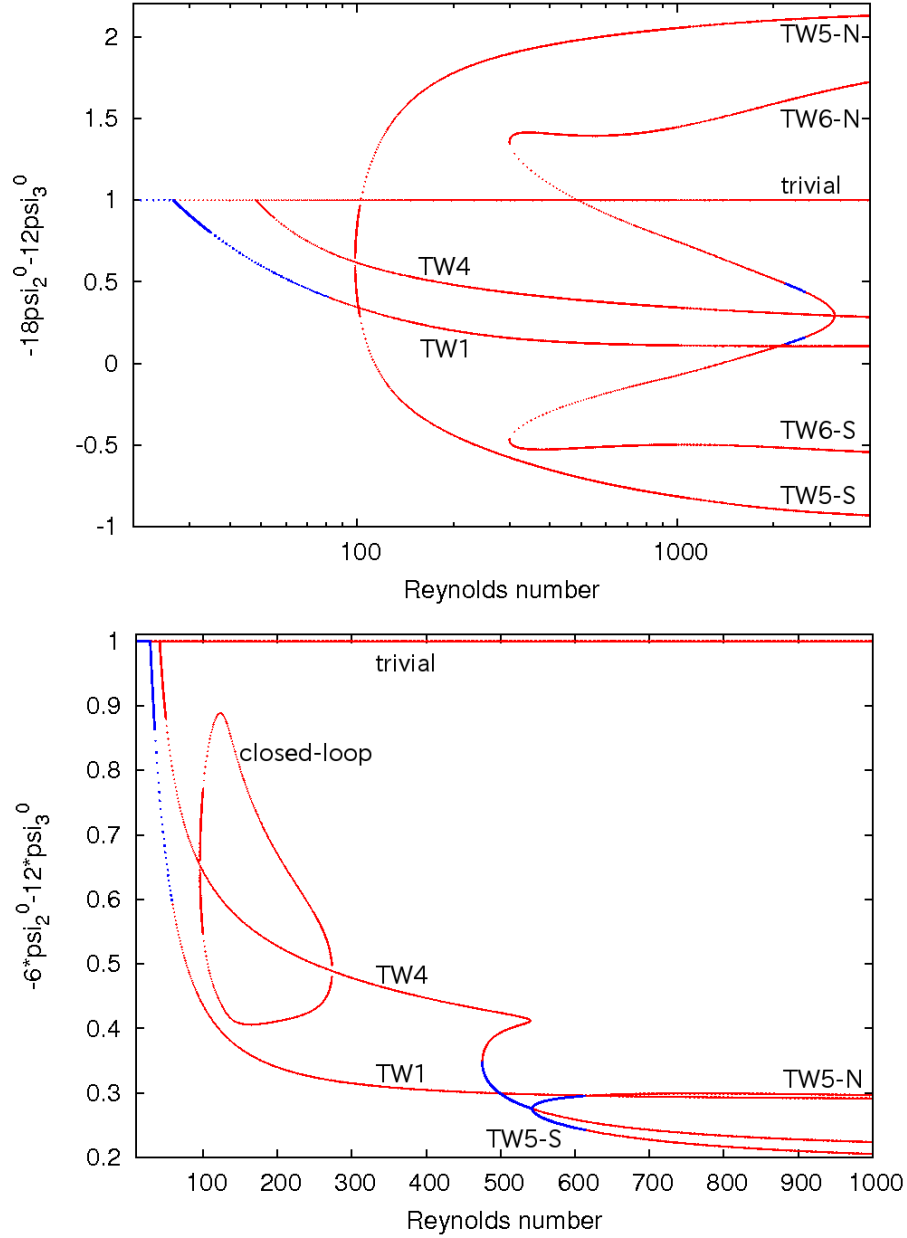


Figure 3.8: Same as figure 3.6 but $\Omega = -0.5$ and -1.0 . The top and bottom figures show the case of $\Omega = -0.5$ and -1.0 , respectively. The horizontal and vertical axes indicate Reynolds number and $-18\psi_2^0 - 12\psi_3^0$ in the top figure and $-6\psi_2^0 - 12\psi_3^0$ in the bottom figure, respectively. Note is that in the top figure the horizontal axis is Log-scale in order to describe all bifurcation points.

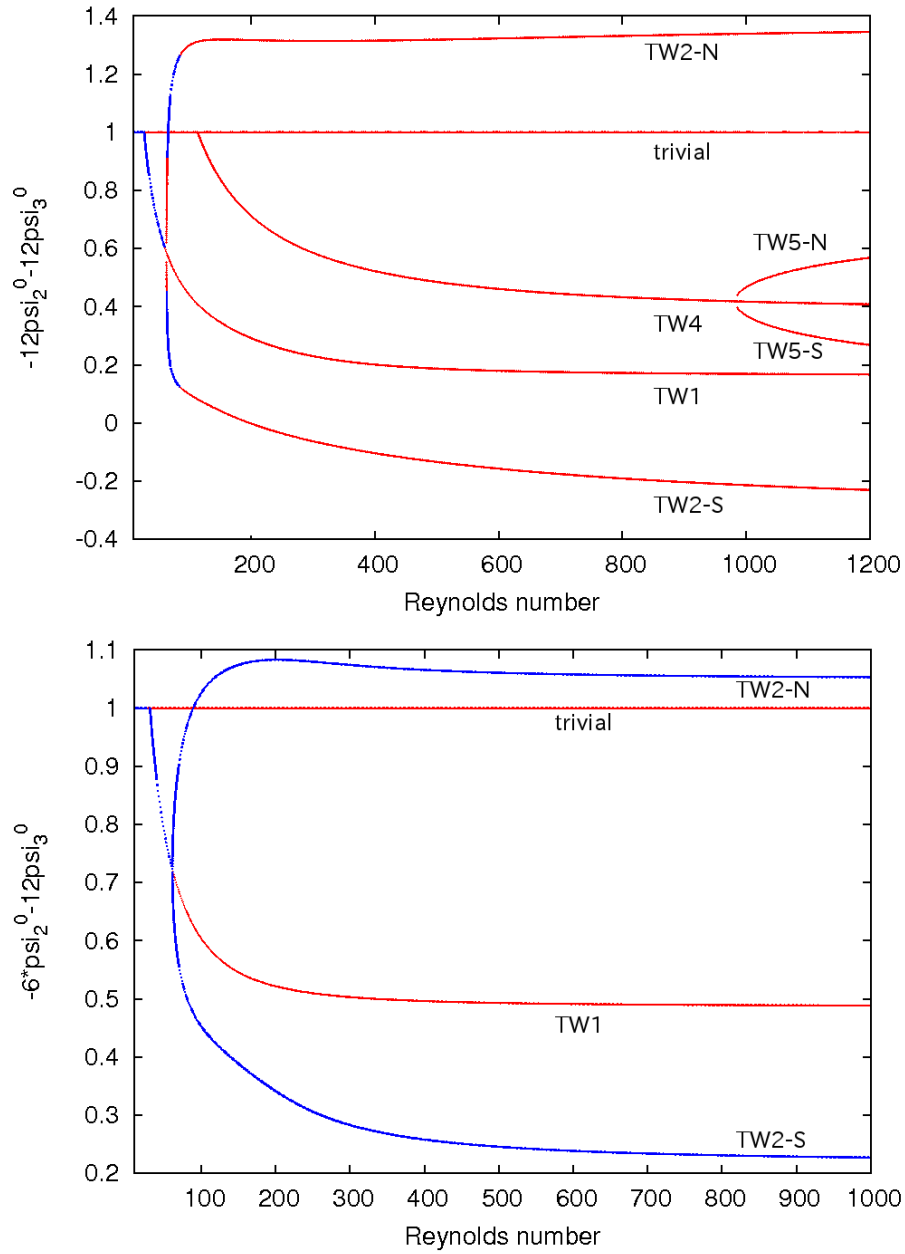


Figure 3.9: Same as figure 3.6 , but $\Omega = 0.5$ and 1.0 . The top and bottom figures show in the case of $\Omega = 0.5$ and 1.0 , respectively. The horizontal and vertical axes indicate Reynolds number and $-12\psi_2^0 - 12\psi_3^0$ in the top figure and $-6\psi_2^0 - 12\psi_3^0$ in the bottom figure, respectively.

3.5.3 Characteristics of steady traveling solutions at high Reynolds number

In this section we discuss the flow field of the steady traveling solutions at high Reynolds number. Figure 3.10 shows streamfunctions of TW1 at $\Omega = 0.0, 0.5, 1.0$. The flow field consists of four positive and negative mid-latitude vortices, and as Reynolds number increases, the stream function becomes more symmetric with respect to the equator with the circumpolar flows being reduced. We find that the streamfunction of TW1 almost recovers the equatorial symmetry at $R = 10^6$. In the cases of $\Omega = 0.5$ and 1.0 , we find that in contrast with the non-rotating case, the mid-latitude vortices remains non-symmetric with respect to the equator and the circumpolar vortices survives when R is increased. The flow fields seem to change little for $R \gtrsim 10^4$. We also find that in the cases of $\Omega = -0.5$ and -1.0 , the streamfunction of TW1 does not have the equatorial symmetry at high Reynolds number, either. We note that the trivial solution does not have this symmetry. On the other hand, in the case of $\Omega = 0.0$, each vortex is almost symmetric with respect to a meridian passing through the center of the vortex at high Reynolds numbers. However, this symmetry is not observed for $\Omega \neq 0$ at high Reynolds numbers.

Figure 3.11 shows the zonal-mean zonal velocity profile for TW1 and TW5-N at $\Omega = 0.0$ together with the trivial solution, where the zonal-mean zonal velocity is defined by

$$U(\mu) := \frac{1}{2\pi} \int_0^{2\pi} u_\lambda(\lambda, \mu) d\lambda,$$

in which $u_\lambda(\lambda, \mu)$ is the longitudinal component of the velocity. Note that the trivial solution is always the steady solution irrespective of the Reynolds number. For TW1, we see that as the Reynolds number increases the magnitude of zonal-mean zonal velocity of TW1 decreases and it is nearly 1/1000 of that of the trivial solution at $R = 10^6$. This phenomena may be inferred from the fact that the positive and negative vortices for $\Omega = 0$ and $R = 10^6$ in figure 3.10 are almost the same with the sign reversed, and therefore they almost cancel out with each other when zonally averaged, resulting in a nearly vanishing profile of zonal velocity. On the other hand, the zonally averaged profiles for TW5-N and TW5-S (figure 3.11) show clear zonal jet flows even at high Reynolds numbers, where the number of the zonal jets in the zonally averaged profiles changes from 3 to 2 as the Reynolds number is increased, and the magnitude of the zonal jets is even stronger than the trivial solution. This result is partially inferred from the streamfunction of TW5-N shown in Figure 3.12, where, as the Reynolds number increases, the vortices spread and become uniform in the longitudinal direction, preventing the cancellation when averaged. However, the mechanism of the reduction of the number of jets in the averaged velocity profile is left open. It should be added that in the rotating cases the number of jets in the zonal-mean zonal velocity profile of steady traveling solutions appears to take a constant value (3 in this case) even at high Reynolds numbers.

3.5 Bifurcation structure of nonlinear steady solutions arising from 3-jet zonal flow

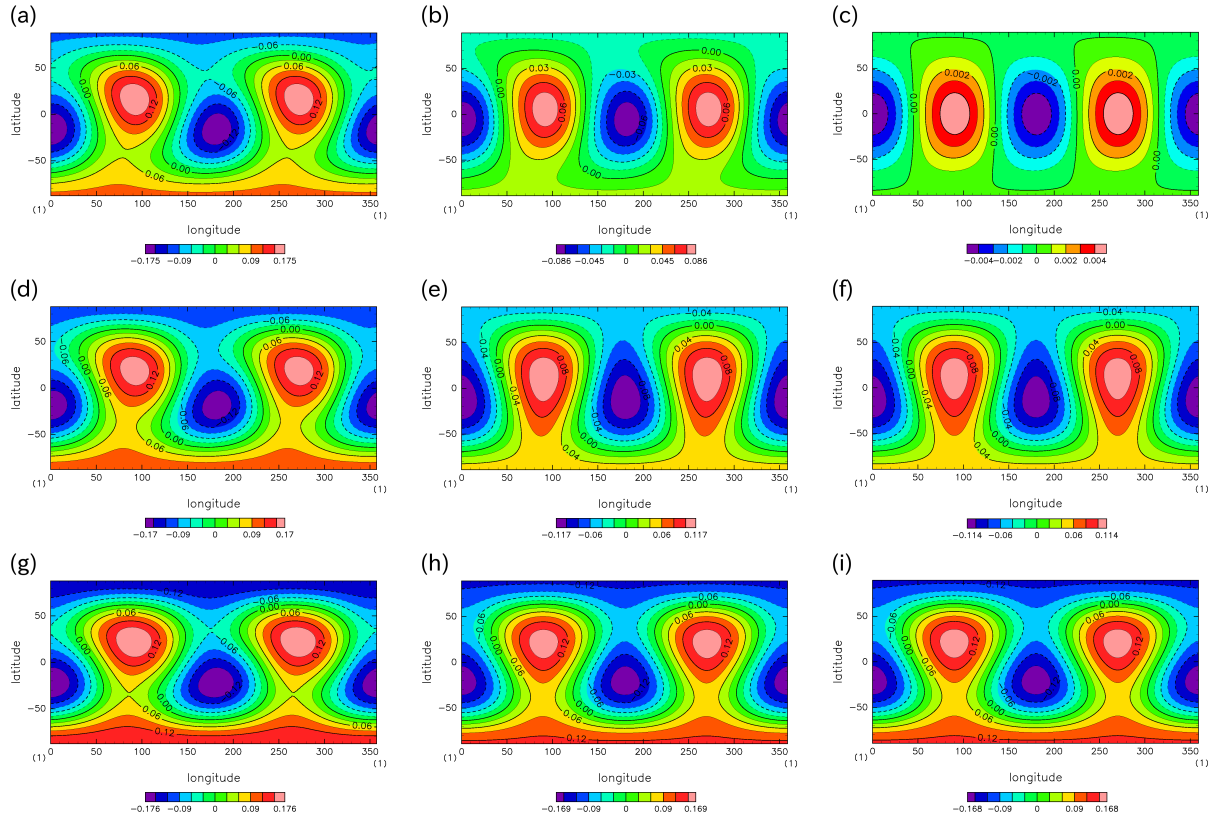


Figure 3.10: Streamfunctions of TW1: (a) $\Omega = 0.0, R = 10^2$, (b) $\Omega = 0.0, R = 10^3$, (c) $\Omega = 0.0, R = 10^6$, (d) $\Omega = 0.5, R = 10^2$, (e) $\Omega = 0.5, R = 10^3$, (f) $\Omega = 0.5, R = 10^6$, (g) $\Omega = 1.0, R = 10^2$, (h) $\Omega = 1.0, R = 10^3$, and (i) $\Omega = 1.0, R = 10^6$, respectively. The horizontal and vertical axes indicate longitude and latitude, respectively.

3 Stability and bifurcation structure of viscous zonal jet flows on a rotating sphere

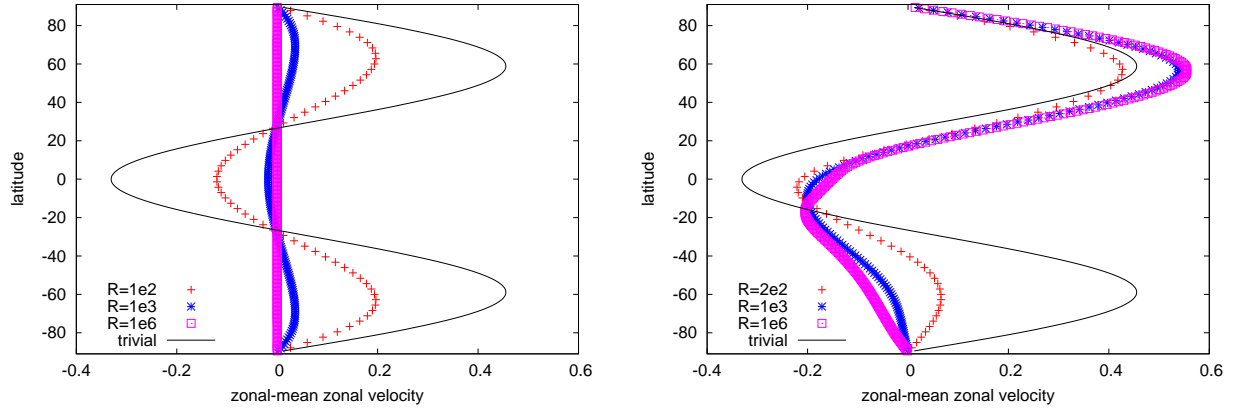


Figure 3.11: zonal-mean zonal velocity of TW1 and TW5 at $\Omega = 0.0$. The left and right figures show TW1 and TW5-N cases, respectively. In the left figure red cross, blue asterisk and purple square denote $R = 100, 10^3$ and 10^6 cases, respectively, and in the right figure $R = 200, 10^3$ and 10^6 cases, respectively. The horizontal and vertical axes indicate zonal-mean zonal flow and latitude, respectively. For comparison the black line denote the longitudinal velocity of the trivial solution.

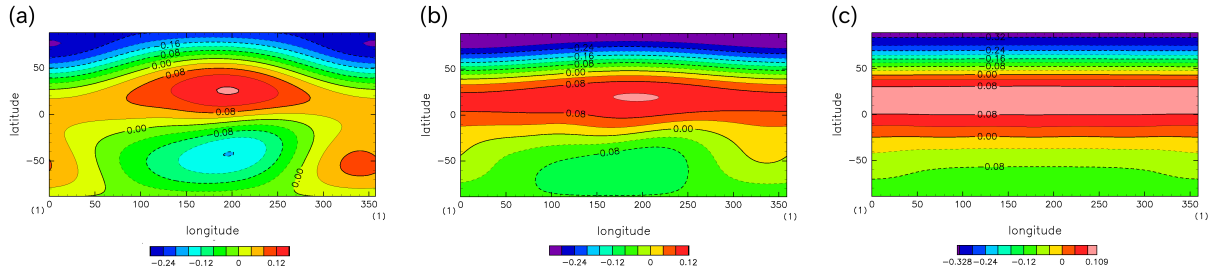


Figure 3.12: Streamfunctions of TW5-N at $\Omega = 0.0$: (a) $R = 200$, (b) $R = 10^3$ and (c) $R = 10^6$, respectively. The horizontal and vertical axes indicate longitude and latitude, respectively.

3.6 Numerical simulations at high Reynolds number under 3-jet zonal forcing

To study attractor properties at high Reynolds number, we carry out numerical simulation with varying the Reynolds number and the rotation rate for $R = 10^3, 10^4$ and $\Omega = 0.0, \pm 0.5, \pm 1.0$. We employ the spectral method as same as before section but the truncation wavenumber is fixed on $N = 53$ (for the grid points $I = 160$ and $J = 80$). The time integration is performed with the fourth order Runge-Kutta method with a time step interval $\delta t = 0.05$ from several initial conditions which are given by each nonlinear steady solution added with three different disturbances

$$\psi(t = 0, \lambda, \mu) = \psi_N(\lambda, \mu) + \delta\psi_i(\lambda, \mu) \quad (i = 1, 2, 3),$$

where ψ_N and $\delta\psi_i$ are the steady/steady traveling solutions and the disturbances, respectively. The disturbances are given by

$$\delta\psi_i(\lambda, \mu) = \sum_{n=2}^{10} \sum_{m=-n}^n \delta\psi_{in}^m Y_n^m(\lambda, \mu),$$

where $\delta\psi_{in}^m$ is the expansion coefficient in which the uniform random number are substituted with the energy density of $\delta\psi_i$ equal to 10^{-4} times of that of the original steady/steady traveling solutions. Here the energy density of ψ is defined by

$$E = \frac{1}{8\pi} \int |\nabla\psi|^2 dS = -\frac{1}{8\pi} \int \psi\Delta\psi dS.$$

We carry out the time integration until $t = 5 \times 10^5$ and calculate statistical quantities at the interval $5 \times 10^4 \leq t \leq 5 \times 10^5$.

3.6.1 Properties of chaotic solutions in the non-rotating case

From the bifurcation analysis (Section 3.5) we find the eleven steady/steady traveling solutions at $R = 10^4$, one of which is the trivial solution, and these solutions are already Hopf unstable since $R = 249.5$. Figure 3.13 and 3.14 show the streamfunctions and the zonal-mean zonal velocity of the steady/steady traveling solutions at $R = 10^4$, respectively. The number of initial conditions is 33 obtained by the eleven steady/steady traveling solutions with 3 disturbances and we take an ensemble average by the 33 solution orbits obtained by these initial conditions.

Figure 3.15 shows the time series of the energy density of solutions orbits and its power spectrum. The energy density undergoes intermittent bursts and its power spectrum is broad, that is, the solution orbits are chaotic. Figure 3.16 and 3.17 show the snapshots of streamfunction and zonal-mean zonal velocity, respectively. We find that there are many

3 Stability and bifurcation structure of viscous zonal jet flows on a rotating sphere

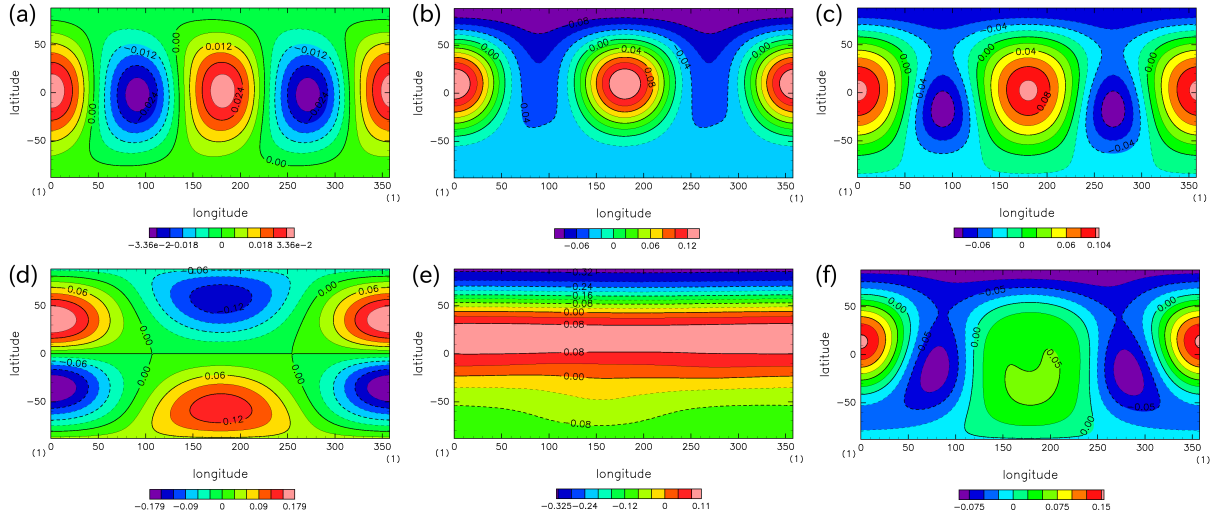


Figure 3.13: Streamfunctions of the nonlinear steady solutions at $\Omega = 0.0$ and $R = 10^4$: (a) TW1 (b) TW2-N, (c) TW3-N, (f) TW4 (e) TW5-N and (f) TW6-N, respectively. The horizontal and vertical axes indicate longitude and latitude, respectively.

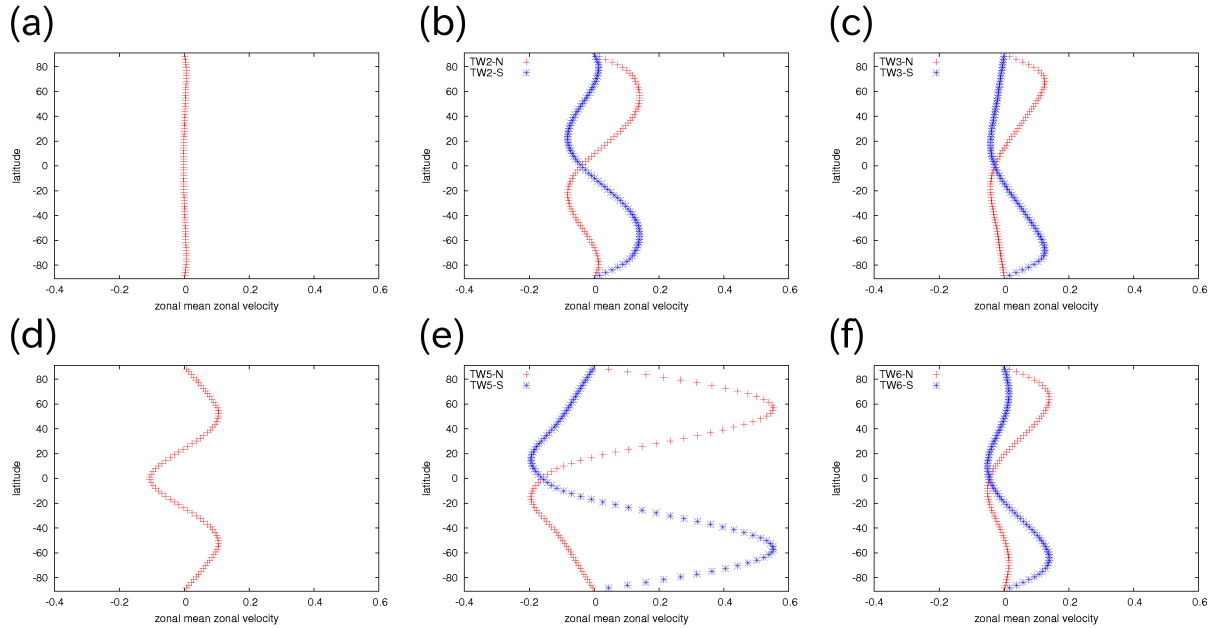


Figure 3.14: Zonal-mean zonal velocity of the nonlinear steady solutions at $\Omega = 0.0$ and $R = 10^4$: (a) TW1 (b) TW2, (c) TW3, (f) TW4 (e) TW5 and (f) TW6, respectively. In figure (b) red cross and blue asterisk indicate TW2-N and TW2-S, respectively. This point manner is same in the TW3, TW5 and TW6 cases.

time when the streamfunction of the chaotic solutions is similar to each unstable steady traveling solution. Then the chaotic orbits seem to wander around the unstable steady solutions.

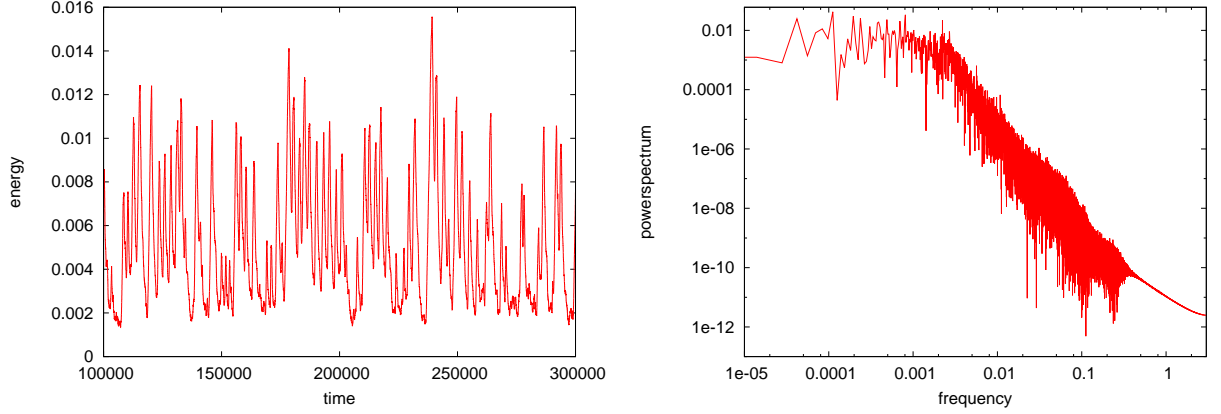


Figure 3.15: The time series of energy density and the power spectrum at $\Omega = 0.0$ and $R = 10^4$. The left and right figures show time series of energy density and the power spectrum of energy density, respectively. In the left figure the horizontal and vertical axes indicate the time and the energy density, respectively. In the right figure the horizontal and vertical axes indicate the frequency and power spectrum, respectively.

Observing the streamfunctions, we expect that properties of the chaotic solutions can be obtained by using unstable steady solutions. Here we focus on the zonal-mean zonal velocity, and try to reproduce the zonal-mean zonal velocity of the chaotic solutions by using those of the unstable steady/steady traveling solutions. Figure 3.18 shows the time-averaged zonal-mean zonal velocity \bar{U} of chaotic flow with the snapshots of zonal-mean zonal velocity. Here $\bar{\cdot}$ denotes time-averaged $\bar{\cdot} = \frac{1}{T} \int_T \cdot dt$. The zonal-mean zonal velocity is equatorial asymmetric but the time-averaged zonal-mean zonal velocity has equatorial symmetry. This means that the chaotic solutions have equatorial asymmetric states with approximately same frequencies. The number of jets of the time-averaged zonal-mean zonal velocity is 3 which is equal to that of trivial solution but the magnitude of that is $\sim 1/10$ of the trivial solution.

First, we consider a linear combination

$$\tilde{U}(\mu) = \sum_{i=1}^{11} a_i U_i(\mu), \quad (3.21)$$

where a_i are constant coefficients and $U_i(\mu)$ are the zonal-mean zonal velocities of unstable steady/steady traveling solutions. The coefficients a_i is obtained by the ratios of time-averaged energy distance, $a_i = \bar{r}_i / \sum_j \bar{r}_j$ and recurrence ratios $a_i = p_i$ defined by the ratio of the number of times when ψ_i is the closest solution from the point on the chaotic orbit

3 Stability and bifurcation structure of viscous zonal jet flows on a rotating sphere

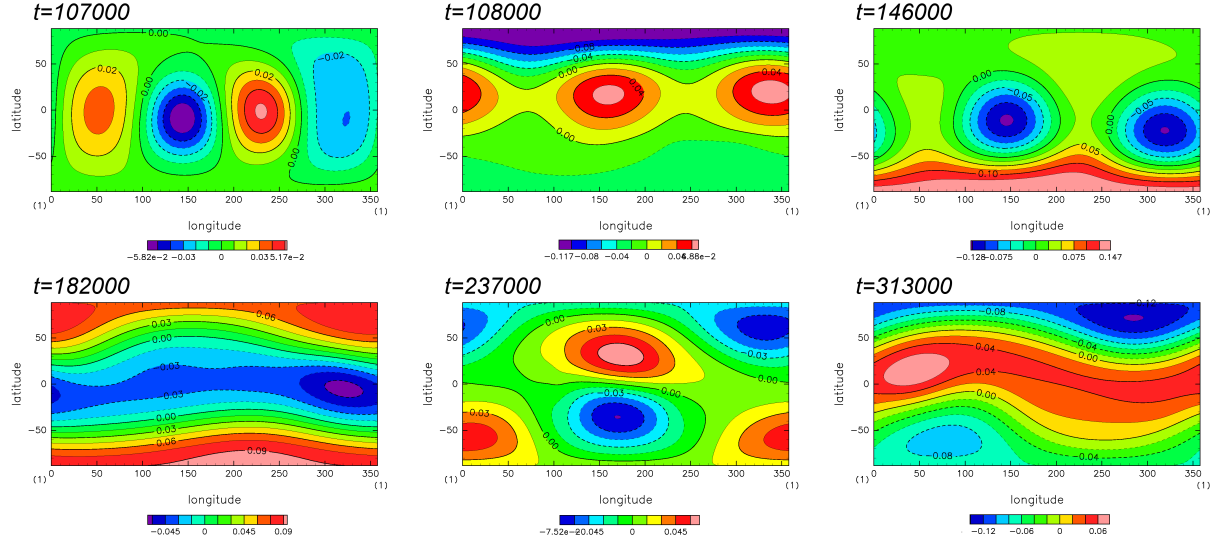


Figure 3.16: Snapshots of streamfunction of chaotic solutions at $\Omega = 0.0$ and $R = 10^4$. The horizontal and vertical axes indicate longitude and latitude, respectively.

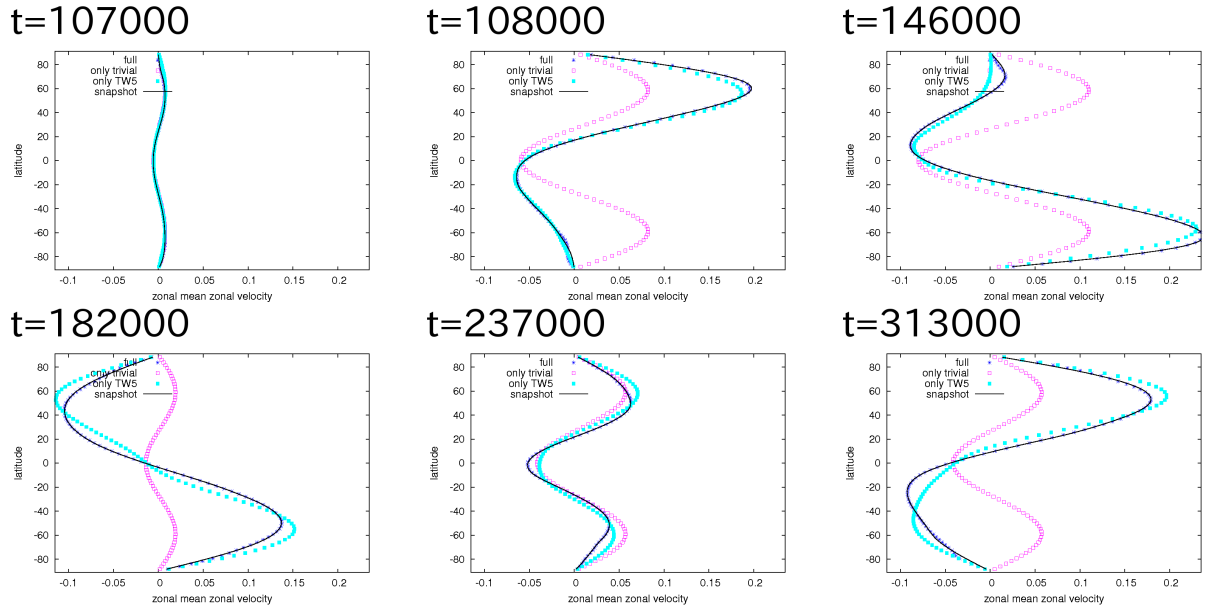


Figure 3.17: Snapshots of zonal-mean zonal velocity of chaotic solutions in the case of $\Omega = 0.0$ and $R = 10^4$ at each time of the streamfunction shown in figure 3.16. The line indicates snapshot of zonal-mean zonal velocity of chaotic solutions. The blue asterisks, purple squares and aqua squares indicate reproduction by the linear mapping using the eleven unstable steady/steady traveling solutions, only trivial solution and TW5, respectively

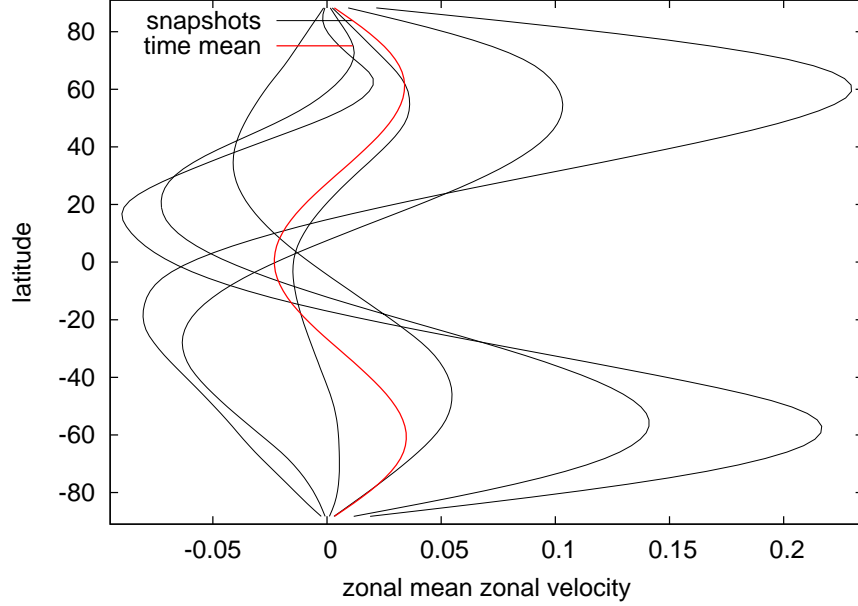


Figure 3.18: The zonal-mean zonal velocity in $\Omega = 0.0$ and $R = 10^4$ case. The red lines denotes time-averaged zonal-mean zonal velocity of chaotic solution, while the black line denotes the snapshots of zonal-mean zonal velocity of the chaotic solution, respectively. The horizontal and vertical axes indicate the zonal-mean zonal velocity and the latitude, respectively.

to the number of observation times. The energy distance between the chaotic solution $\psi(t)$ and each steady/steady traveling solution ψ_S^i given by

$$r_i^2(t) = (\psi(t) - \psi_S^i, \psi(t) - \psi_S^i)_E.$$

$(\psi_1, \psi_2)_E$ is the energy inner product defined by

$$\begin{aligned} (\psi_1, \psi_2)_E &= \frac{1}{4\pi} \int \Delta^{1/2} \psi_1^* \Delta^{1/2} \psi_2 dS \\ &= \sum_{l,m} l(l+1) \psi_{1l}^{m*} \psi_{2l}^m. \end{aligned} \quad (3.22)$$

Here ψ_{1l}^m and ψ_{2l}^m are the expansion coefficients of ψ_1 and ψ_2 , respectively and if $\psi_1 = \psi_2 = \psi$ the energy inner product gives two times of the energy density of ψ .

Figure 3.19 (top) shows the linear combination \tilde{U} . The \tilde{U} , given by the ratios of time-averaged distance or the recurrence ratios, are not close to the time-averaged zonal-mean zonal velocity of the chaotic solution. We also calculate a_i same as the above manner

but using distances between zonal-mean streamfunctions of chaotic solutions and unstable steady/steady traveling solutions, however we find that the linear combinations do not reproduce the time-averaged zonal-mean zonal velocity of chaotic solutions. As a results, the linear combination of the zonal-mean zonal velocity using the energy distances (3.21) can not reproduce the time-averaged zonal-mean zonal velocity.

Next, we consider a linear mapping defined as below. When the linear mapping operates the steady/steady traveling solutions ψ_i , the linear mapping gives the zonal-mean zonal velocity of ψ_i , that is $U_i(\mu)$, while if the linear mapping operates the orthogonal compliment of the linear space which is extended by the steady/steady traveling solutions, the linear mapping gives zero. To obtain the function values of this linear mapping, first, we consider a member of the linear space extended by the longitudinal velocities of the steady/steady traveling solutions, which given by

$$\hat{u}(\lambda, \mu) = \sum_{i=1}^N \int \frac{d\theta}{2\pi} c_i(\theta) u_i(\lambda - \theta, \mu) + \sum_{j=1}^M d_j U_j^S(\mu),$$

where $u_i(\lambda, \mu)$ are the longitudinal velocities depending on the longitude while $U_j^S(\mu)$ are the longitudinal velocities independent of the longitude. $c_i(\theta)$ and d_j are expansion coefficients. Taking zonal mean of $\hat{u}(\lambda, \mu)$, we obtain

$$\int \hat{u}(\lambda, \mu) \frac{d\lambda}{2\pi} = \sum_{i=1}^N \int \frac{d\theta}{2\pi} c_i(\theta) U_i(\mu) + \sum_{j=1}^M d_j U_j^S(\mu) = \hat{U}(\mu) \quad (3.23)$$

where $\hat{U}(\mu)$ and $U_i(\mu)$ are zonal-mean zonal velocity of $\hat{u}(\lambda, \mu)$ and $u_i(\lambda, \mu)$, respectively. The coefficients $\int \frac{d\theta}{2\pi} c_i(\theta)$ and d_j can be obtained by

$$\int \frac{d\theta}{2\pi} c_i(\theta) = \int_{-1}^1 \frac{d\mu}{2} U_i^{\dagger*}(\mu) \hat{U}(\mu) \quad d_j = \int_{-1}^1 \frac{d\mu}{2} U_j^{S\dagger*}(\mu) \hat{U}(\mu) \quad (3.24)$$

where $U_i^{\dagger}(\mu)$ and $U_j^{S\dagger}(\mu)$ are dual bases of $U_i(\mu)$ and $U_j^S(\mu)$, respectively. Here we assume that $U_i(\mu)$ and $U_j^S(\mu)$ are linear independent of each other. And we also define the inner product of zonal-mean zonal velocity $U_i(\mu)$ and $U_j(\mu)$ by

$$\int_{-1}^1 \frac{d\mu}{2} U_i^*(\mu) U_j(\mu).$$

To obtain the dual bases we use Schmidt orthogonalization method. When we obtain $U_i^{\dagger}(\mu)$, for example, in first we carry out Schmidt orthogonalization for zonal-mean zonal velocities except for $U_i(\mu)$, and we employ the orthogonalization to U_i to obtain orthogonal basis $e_i(\mu)$ with which the inner product of $U_j(\mu)$ is zero except for the case of $j = i$. Through an appropriate scaling for $e_i(\mu)$, we obtain the dual basis $U_i^{\dagger}(\mu)$. The function values of

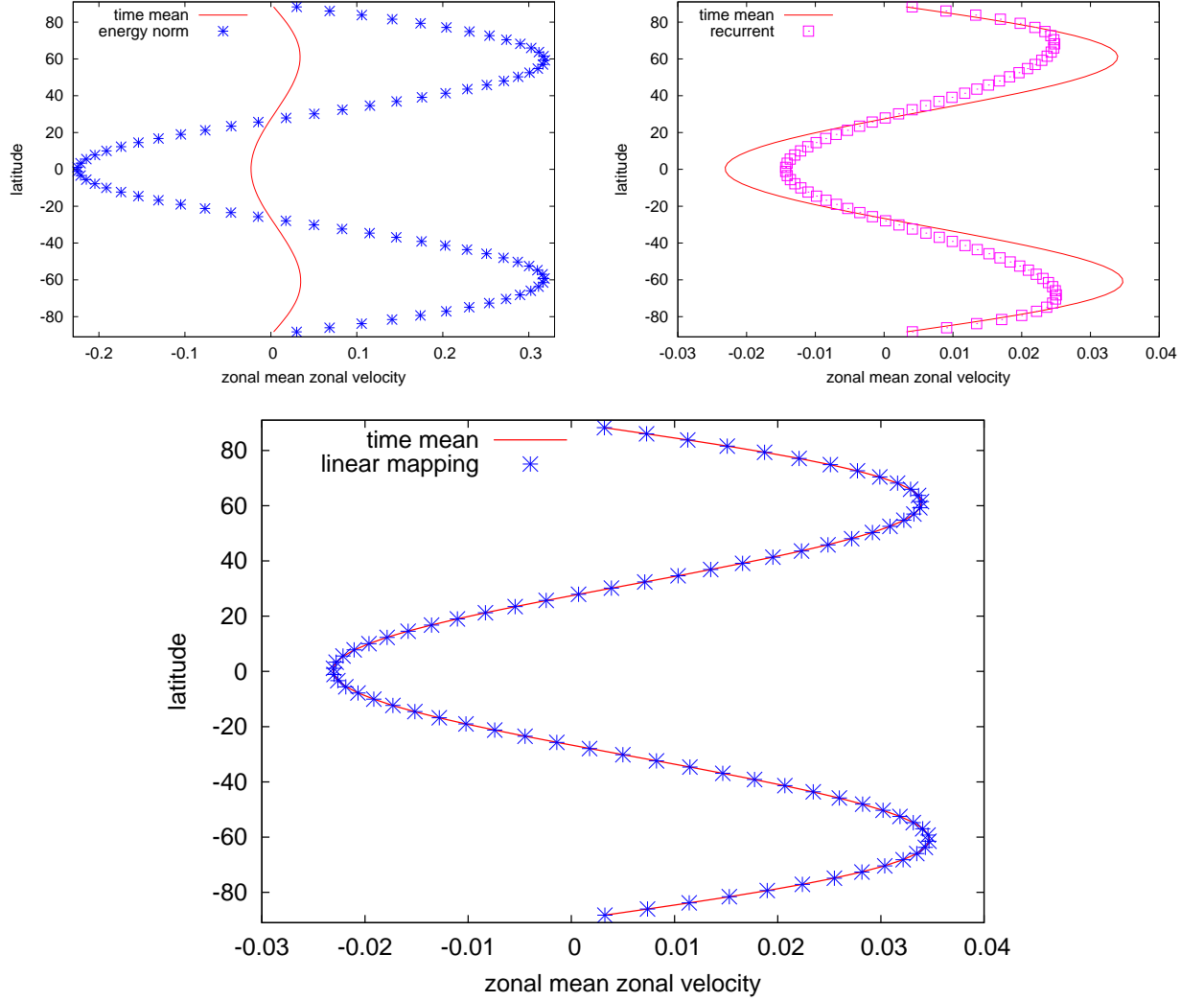


Figure 3.19: Reproduction of time-averaged zonal-mean zonal velocity in $\Omega = 0.0$ and $R = 10^4$ case. The top and bottom figures show reproductions using the linear combination (3.21) and the linear mapping method (3.23), respectively. The red line denotes time-averaged zonal-mean zonal velocity of the chaotic solution. In the top-left figure, the blue asterisks denote the linear combinations the coefficients of which are obtained by the energy distance ratios while in the top-right figure the purple squares denote that the coefficients of which obtained by the recurrence ratios. In the bottom figure, the blue asterisks denote $\tilde{U}(\mu)$ using the eleven steady/steady traveling solutions.

the linear mapping are obtained by the equation (3.23) substituting the zonal-mean zonal velocity of the chaotic solution $U(\mu, t)$ in $\hat{U}(\mu)$.

Figure 3.19 (bottom) shows the time-averaged (3.23) using the eleven steady/steady traveling solutions for the linear mapping. We find that $\bar{\hat{U}}(\mu)$ approximates well the time-averaged zonal-mean zonal velocity of the chaotic solutions within $\sim 0.3\%$ error. However, figure 3.20 shows $\bar{\hat{U}}(\mu)$ using only trivial solution and only a single pair of TW5-N and TW5-S, respectively. We find that $\bar{\hat{U}}(\mu)$ by using only the single solution also approximate the time-mean zonal-mean zonal velocity of chaotic solution.

By contrast, there are differences on the time series of the zonal-mean zonal velocity. Figure 3.21 shows the time series of relative errors between the zonal-mean zonal velocity of chaotic solutions $U(\mu, t)$ and the reproduced zonal-mean zonal velocity by the linear mapping. Here the relative error is given by

$$\mathcal{E}(t) = \frac{\sqrt{\int_{-1}^1 \frac{d\mu}{2} (U(\mu, t) - \hat{U}(\mu, t))^2}}{\sqrt{\int_{-1}^1 \frac{d\mu}{2} U^2(\mu, t)}}$$

We find that the time series of the relative errors of linear mapping using the eleven steady/steady traveling solutions are smaller than that using only the trivial solution or the TW5, although they give good approximations to the time-averaged zonal mean zonal velocity. Figure 3.22 shows the time and ensemble average of the relative error for using the eleven unstable solutions and each single solution. Clearly the relative error of the linear mapping using the eleven steady/steady traveling solutions is smallest in the other cases. Then if the eleven steady/steady traveling solutions are taken as the bases of the linear space, this linear mapping method gives good approximations to not only the time-averaged but also the time-progressing zonal-mean zonal velocity of the chaotic solutions. On the figure 3.17 this results can be found partially by that $\hat{U}(\mu)$ using the eleven steady/steady traveling solutions are very close to the zonal-mean zonal velocity of the chaotic solutions for the several times.

This result suggests that the chaotic solutions even at high Reynolds number, which is 40 times of the critical Reynolds number of the laminar flow (see section 3.5), lay mostly within a relatively low-dimensional space spanned by the steady/steady traveling solutions. In addition, we also carry out the time integration at $R = 10^3$ and we find that solutions are also chaotic and the linear mapping method also gives good approximations to the time-progressing zonal-mean zonal velocity of chaotic solutions. This result suggests that the properties of chaotic solutions do not change drastically at high Reynolds numbers.

Next considering the contributions from each steady solution in the linear mapping,

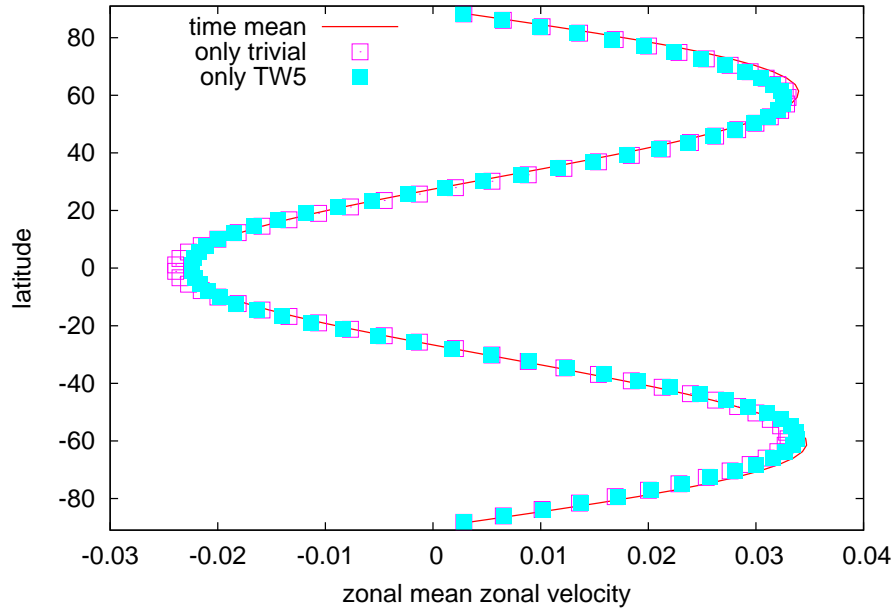


Figure 3.20: time-averaged zonal-mean zonal velocity of \hat{U} using only the trivial solution and TW5. The red line denote time-averaged zonal-mean zonal velocity of the chaotic solutions. The purple and aqua squares denote approximation using only the trivial solution and the pair of TW5-N and TW5-S, respectively.

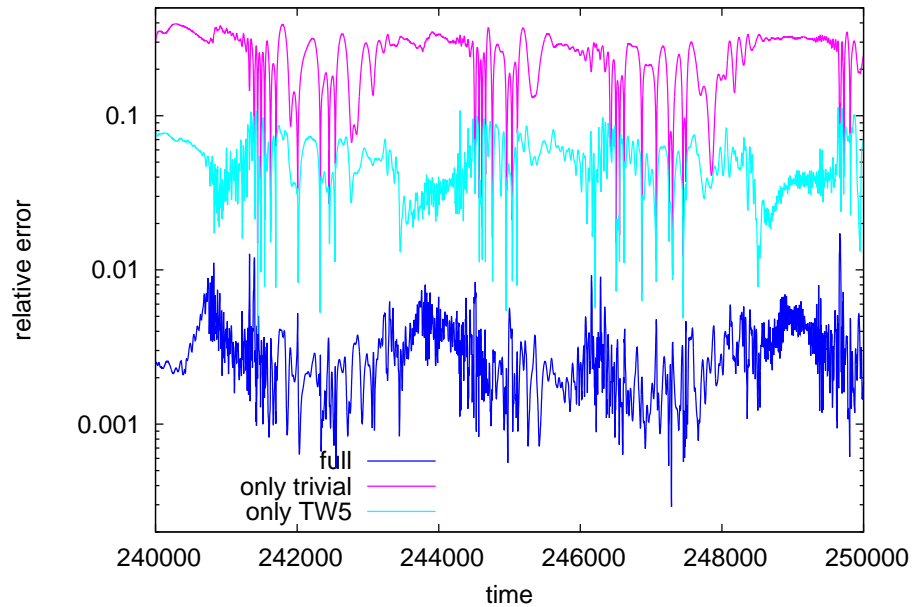


Figure 3.21: The time series of the error of the approximation \mathcal{E} . The blue, purple and aqua lines denote the error using the eleven steady/steady traveling solutions, only the trivial solution and TW5-N, respectively. The horizontal and vertical axes indicate the time and the error of approximation, respectively.

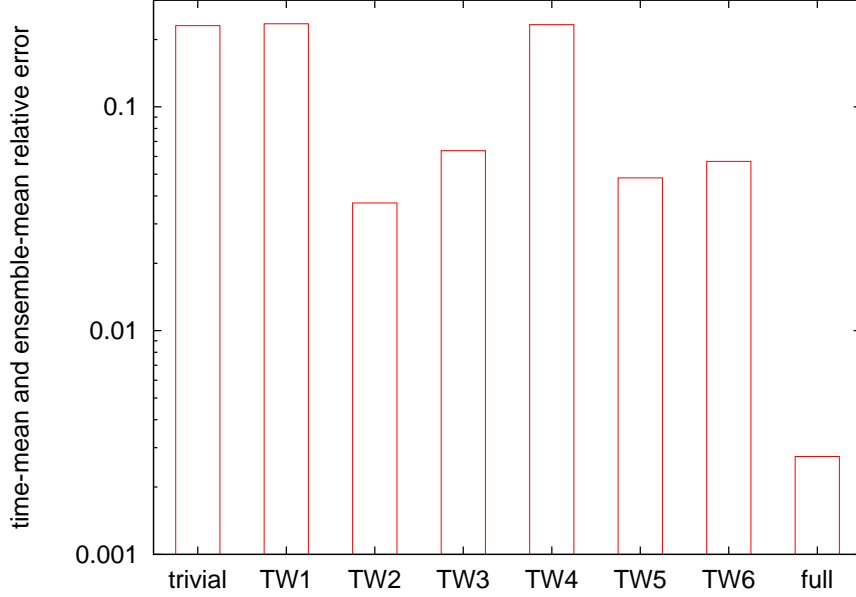


Figure 3.22: Ensemble-time-averaged of the error of the approximation \mathcal{E} . The horizontal and vertical axes indicate the kinds of the linear mapping and the ensemble-time-averaged error of approximation, respectively. On the horizontal axes, the characters denote the bases of the linear mapping using only trivial solution, only TW1, the pair of TW2-N and TW2-S, the pair of TW3-N and TW3-S, only TW4, the pair of TW5-N and TW5-S, the pair of TW6-N and TW6-S and the eleven steady/steady traveling solutions, respectively.

we study the time-averaged square of the inner product with \hat{U} ,

$$\int \frac{dt}{T} \left(\int_{-1}^1 e_i^*(\mu) \hat{U}(\mu) d\mu \right)^2, \quad (3.25)$$

where $e_i(\mu)$ is a normalized vector of the dual basis $U_i^\dagger(\mu)$. This quantity represents the amount of the contribution of the zonal-mean zonal velocity $U_i(\mu)$ for $\hat{U}(\mu)$; if this quantity is small the contribution of $U_i(\mu)$ is small. We call this quantity *the contributing energy* of the nonlinear solution i . Suppose that the linear mapping is constructed by N solutions. We then exclude a solution the contributing energy of which is the smallest among the N solutions and construct a new linear mapping using the remaining $N-1$ solutions. Excluding solutions one by one starting from the linear mapping using the eleven solutions, we study a relevance between the number of the solutions used in the linear mapping and the time average of the absolute error of $\hat{U}(\mu)$,

$$\int \frac{dt}{T} \sqrt{\int \frac{d\mu}{2} (U(\mu, t) - \hat{U}(\mu, t))^2}.$$

Figure 3.23 shows the time and ensemble average of the absolute error as a function of the number of the solutions used in the linear mapping. When the eleven solutions are used for the linear mapping the absolute error is smallest. As the number of solutions N decreases, at first the absolute error varies only slightly, but when the number of the solutions is less than 8, the absolute error increases rapidly as $N^{-1.82}$. Table 3.3 shows the solutions used in each step. It should be noted that in the 3rd step the time and ensemble average of the contributing energy of TW2-N is slightly larger than that of TW2-S and then we exclude TW2-S in the 4th step. We expect that if TW2-N is excluded in the 4th step the remaining solutions in the 10th step should be TW2-S and TW6-N because the time average of the chaotic zonal-mean zonal velocity has the equatorial symmetry. When $N < 5$ the absolute error increases rapidly and this result suggests that the chaotic solution should exist disproportionately around TW2 and TW6. In addition we confirm that when the trivial solution, TW3-N, TW3-S, TW6-N, and TW6-S are used for the linear mapping where TW3-S is excluded in the 7th step, the absolute error of the linear mapping is greater than that using the trivial solution, TW2-N, TW3-N, TW6-N and TW6-S.

As an idealized model case, consider a chaotic attractor which uniformly distributes in M -dimensional sphere with the radius R . The distance between this chaotic attractor and the subspace which is expanded by the N mutually orthogonal vectors ($N < M$) is given by $d_N = \sqrt{\int_{V_M} \frac{dV}{V_M} \sum_{i=1}^{M-N+1} x_i^2} = \sqrt{\frac{M-N+1}{M+2}} R$, where V_M is the volume of the M -dimensional sphere. Then the absolute error is proportional to $\sqrt{12-N}$, in contrast with $N^{-1.82}$ in our case. This result suggests that the chaotic attractor nonuniformly distributes around the specific solutions such as TW2.

3.6.2 Properties of solutions orbits in the rotating case

We also carry out time integration at $\Omega = \pm 0.5, \pm 1.0$ with varying $R = 10^3, 10^4$. Figure 3.24 shows the power spectrum of the energy density of unsteady solutions at each parameter and Table 3.4 shows the type of unsteady solutions. The solutions are steady traveling or periodic except for $\Omega = 0.0$ and $\Omega = -0.5, R = 10^4$ cases where we find chaotic solutions. When $\Omega = 1.0$ and $R = 10^3$, the solutions obtained by time integration are TW2. When $\Omega = 0.5$ and $R = 10^4$ we find the solutions are two kinds of periodic solution. This result suggests that the solutions tends to be less chaotic under the stabilizing effect of rotation. Here we show the case of $\Omega = -1.0, R = 10^3$.

Figure 3.25 shows the streamfunctions of the steady traveling solutions at $\Omega = -1.0, R = 10^3$. From the bifurcation analysis we find five steady/steady traveling solutions at $\Omega = -1.0, R = 10^3$ as far as our computation, and these solutions are already Hopf unstable since $R = 614.4$.

The unsteady solutions obtained by time integration are time-periodic. Figure 3.26 and 3.27 show the snapshots of the streamfunction and zonal-mean zonal velocity of the time-periodic solution. We find that the streamfunction of the time-periodic solutions is

# step	trivial	TW1	TW2-N	TW2-S	TW3-N	TW3-S	TW4-0	TW5-N	TW5-S	TW6-N	TW6-S
1	○	○	○	○	○	○	○	○	○	○	○
2	○	○	○	○	○	○	○	○	○	○	○
3	○	○	○	○	○	○	○	○	○	○	○
4	○	○	○	○	○	○	○	○	○	○	○
5	○	○	○	○	○	○	○	○	○	○	○
6	○	○	○	○	○	○	○	○	○	○	○
7	○	○	○	○	○	○	○	○	○	○	○
8	○	○	○	○	○	○	○	○	○	○	○
9	○	○	○	○	○	○	○	○	○	○	○
10	○	○	○	○	○	○	○	○	○	○	○
11	○	○	○	○	○	○	○	○	○	○	○

Table 3.3: The name of the steady/steady traveling solutions used in the linear mapping. Column 1 and 2~ 12 indicate the number of steps and the solutions used in the linear mapping.

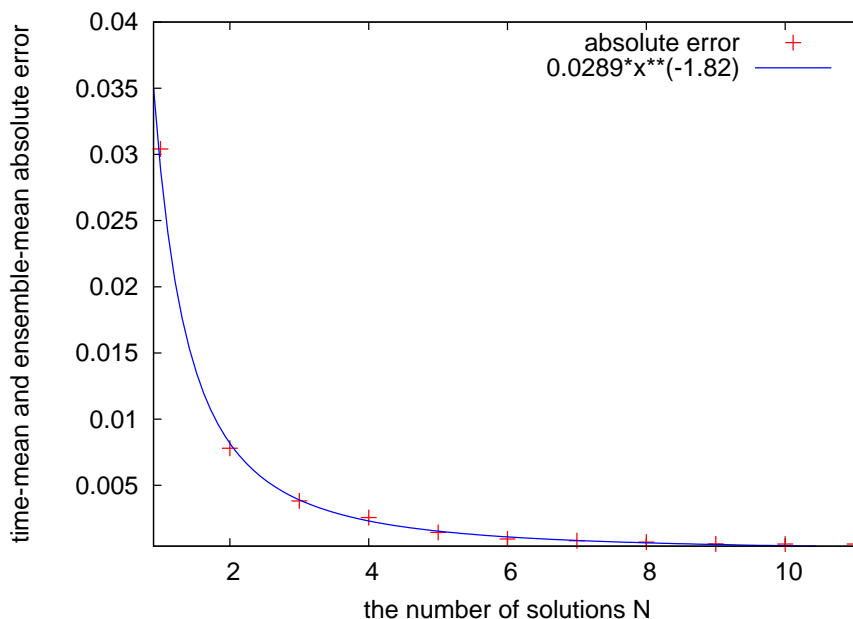


Figure 3.23: Ensemble-time-averaged of the relative error for the linear mapping using the portion steady/traveling solutions. The horizontal and vertical axes indicate the number of solutions used for the linear mapping and the ensemble-time-averaged relative error, respectively.

dissimilar to that of unstable steady/steady traveling solutions and the reproduced zonal-mean zonal velocity by the linear mapping using the unstable solutions does not coincide with the zonal-mean zonal velocity of the periodic solutions. In fact we find that the time and ensemble average of the relative error of $\Omega = -1.0, R = 10^3$ is 2.85×10^{-2} , while that of $\Omega = 0.0, R = 10^4$ is 2.74×10^{-3} , i.e. the time and ensemble average of the relative error of $\Omega = -1.0, R = 10^3$ is larger about 10 times of that of $\Omega = 0.0, R = 10^4$. Then the linear mapping method for the time development reproduces the zonal-mean zonal velocity of time-periodic solution at the case of $\Omega = -1.0, R = 10^3$ less well than that of the chaotic solution at the case of $\Omega = 0.0, R = 10^4$. Figure 3.28, however, shows the time-averaged zonal-mean zonal velocity and the linear mapping reproduces the time-averaged zonal-mean zonal velocity of the periodic solution. The reason why the linear mapping method reproduces the time-averaged zonal-mean zonal velocity but does not reproduce the time development is not clear. This result suggests that the relation between the unsteady solutions and the steady/steady traveling solutions changes as the effect of rotation increases.

3 Stability and bifurcation structure of viscous zonal jet flows on a rotating sphere

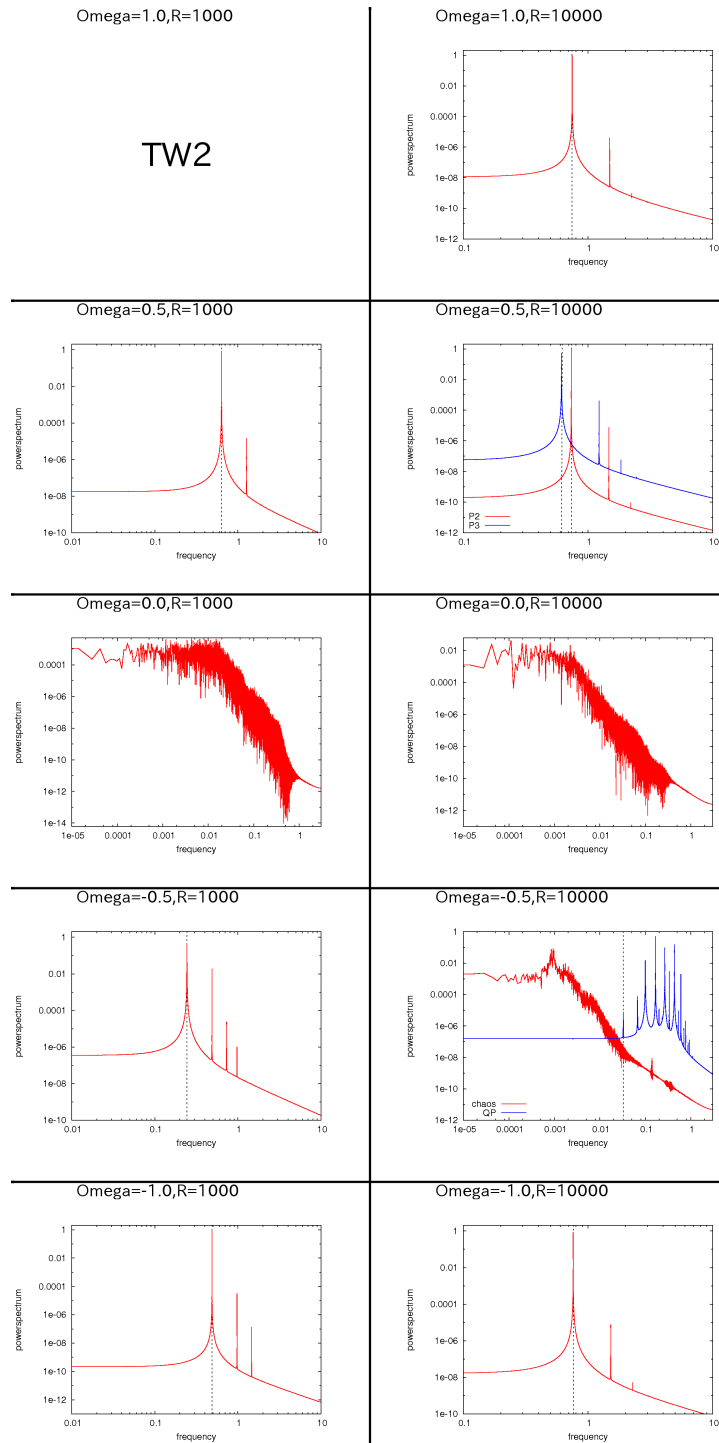


Figure 3.24: Power spectrum of the energy density of the unsteady solutions. Column 1 and 2 indicate the case of $R = 10^3, 10^4$, respectively. Row 1,2,3,4,5 indicate the case of $\Omega = 1.0, 0.5, 0.0, -0.5, -1.0$, respectively.

3.6 Numerical simulations at high Reynolds number under 3-jet zonal forcing

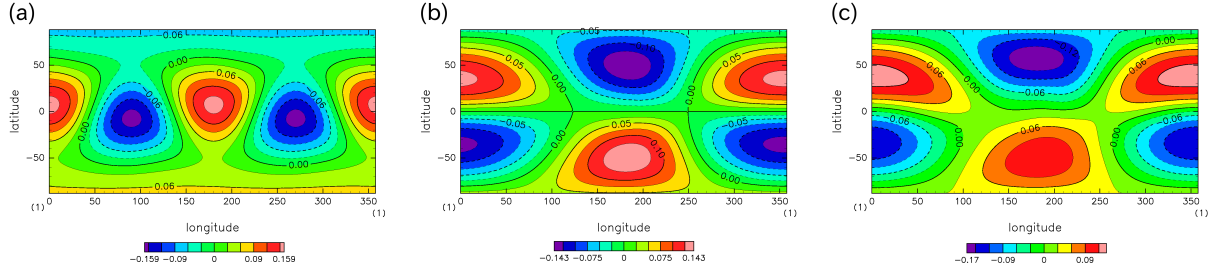


Figure 3.25: The streamfunction of steady traveling solutions at $\Omega = -1.0$ and $R = 10^3$: (a) TW1 (c) TW4, (d) TW5-N, respectively.

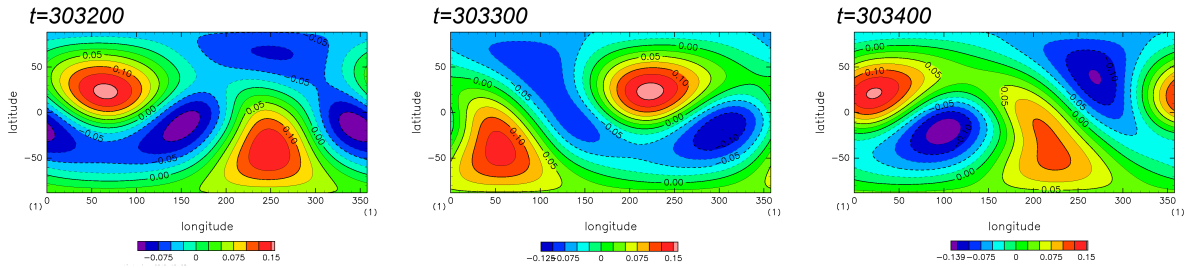


Figure 3.26: Snapshots of streamfunction of time-periodic solutions at $\Omega = -1.0$ and $R = 10^3$. The horizontal and vertical axes indicate longitude and latitude, respectively.

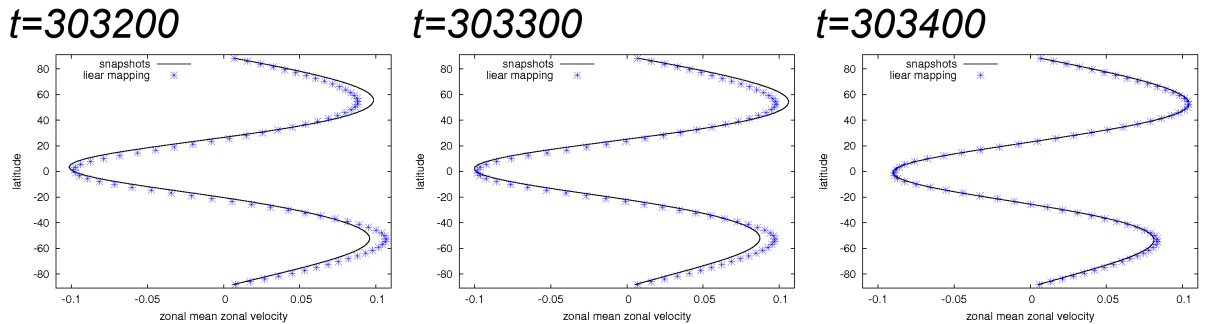


Figure 3.27: Snapshots of zonal-mean zonal velocity of time-periodic solutions in the case of $\Omega = -1.0$ and $R = 10^3$ at each time of the streamfunction shown in figure 3.26. The line indicates snapshot of zonal-mean zonal velocity of chaotic solutions. The blue asterisks indicate the reproduced zonal-mean zonal velocity by the linear mapping using all unstable steady/steady traveling solutions.

Ω	$R = 10^3$	$R = 10^4$
1.0	TW2	TW2 or P
0.5	P	P(2)
0.0	C	C
-0.5	P	QP or C
-1.0	P	P

Table 3.4: The type of solutions. Column 1, 2 and 3 indicate the rotation rate and the Reynolds number $R = 10^3, 10^4$, respectively. In the row 2~6, P, QP and C mean time-periodic solution, quasi-time-periodic solution and chaotic solution, respectively. In the case of $\Omega = 0.5$ and $R = 10^4$, P(2) means that the unsteady solutions are two kinds of periodic solution.

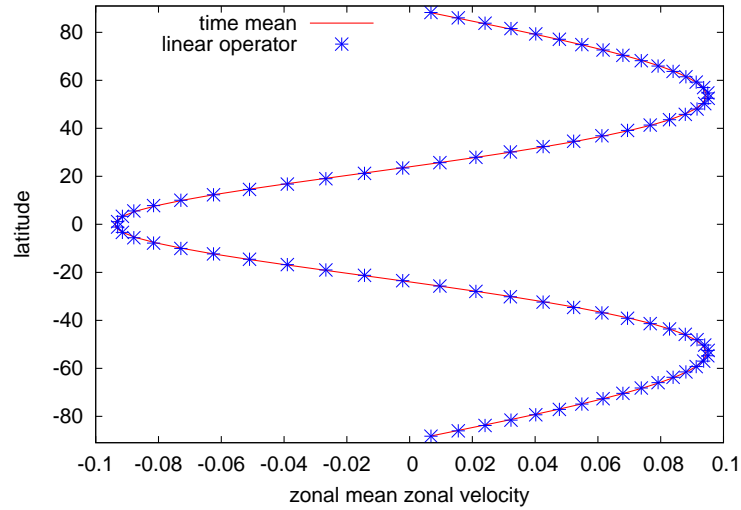


Figure 3.28: Reproduction of time-averaged zonal-mean zonal velocity in the case of $\Omega = -1.0, R = 10^3$ case. The red line denote time-averaged zonal-mean zonal velocity of the time-periodic solution. The blue asterisks denote the time-averaged zonal-mean zonal velocity by the linear mapping method using all steady/steady traveling solutions.

3.7 Conclusion and Discussion

In this chapter we study stability and bifurcation structure of viscous l -jet zonal flow on a rotating sphere. We proof rigorously that 2-jet zonal flow is globally asymptotic stable for any Reynolds number and the rotation rate. In Kolmogorov problem, Iudovisch [13] proved that 2-jet parallel flow on the flat torus is globally asymptotic stable for any Reynolds number. This result implies that the globally stability of 2-jet flow is a common property between the flat torus and the sphere.

The linear stability of l -jet zonal flow with $3 \leq l \leq 9$ is studied numerically. in the non-rotating case, we find that, as the number of jets increases, the critical Reynolds number increases monotonically, the critical modes are Hopf mode, and the critical wavenumbers $m_c = 2$. On the linear stability of Kolmogorov flow, the critical Reynolds number increases monotonically as the number of jets increases, while the critical modes are steady mode (not Hopf) and the critical wavenumbers $m_c = 1$ [5, 14, 18, 23]. It is a similar feature between the flat torus case and the sphere case that, as the number of jets increases, the critical Reynolds number increases monotonically.

in the rotating case we find that the critical Reynolds number takes its lowest value at non-zero rotation rate; at a small negative rotation rate for the odd-jet zonal flow, and at a small non-zero rotation rate (both positive and negative values) for the even-jet zonal flow, while This means that the effect of small rotation is not always the stabilization of the zonal flows, while because the critical Reynolds number of each zonal jet flow increases rapidly the rotation rate increasing large, the zonal flows are stabilized by the large rotation rates. On the inviscid limit of the stability, we find that the unstable region of rotation rate for viscous odd-jet zonal flows is larger than that for inviscid zonal flows, and the former does not converge to the latter even in the inviscid limit. This seeming contradiction between inviscid limit and inviscid is resolved by the observation that as Reynolds number increases the growth rates of the unstable mode converge to zero at the region, where the inviscid zonal flow is stable but viscous zonal flow unstable. On the other hand, if the number of jets is even, we find that as the Reynolds number increases the absolute values of the rotation rates, where the even-jet zonal flow losses the stability, increases monotonically but less than that of inviscid zonal flow. Then, we expect that the critical rotation rate of the inviscid limit coincides with inviscid one.

In the numerical simulation by Obuse et al. [22], the asymptotic states of forced two-dimensional turbulence are only the 2- or 3-jet zonal flow. In the case of that the asymptotic state is the 3-jet zonal flow, we find that the rotation rate, which they adapted, is at least $\Omega \simeq 27$, where the Reynolds number is $R \sim 6.6 \times 10^4$, and the rotation rates at which the resultant flow is 3-jet zonal flow are much greater than the critical rotation rate of the laminar 3-jet zonal flow, 2.171 or -5.727 . However, if the turbulence becomes the 2-jet zonal flow going through 3-jet zonal flow, we find that the rotation rate at the 3-jet stage is at least $\Omega \simeq 9.1$, where the Reynolds number is $R \sim 5.0 \times 10^4$, and the rotation rates when the 3-jet zonal flow emerges in the course of time development are also much greater than

the critical rotation rate of the laminar 3-jet zonal flow. This means that the jet flows found in the intermediate stages would be mostly stable if the jet flows were laminar, and therefore the route to the asymptotic state of the forced turbulence is not explained in the framework of the linear stability of laminar zonal jet flows, while the stability of the resultant 3-jet flow is supported by the linear stability of the laminar 3-jet flow.

We also study the bifurcation structure arising from the 3-jet trivial zonal flow. in the non-rotating case, as Reynolds number increases, the steady traveling wave solutions arises from 3-jet zonal flow through Hopf bifurcation. As Reynolds number more increases, several traveling wave solutions arise only through the pitchfork bifurcation from the traveling wave solutions and finally the steady traveling solutions become Hopf unstable. When $\Omega < 0$, we find the saddle-node bifurcations and the closed-loop bifurcation branch while in the case of $\Omega > 0$ we find only the pitchfork bifurcations. Then the bifurcation structure changes vastly depending on the rotation.

in the non-rotation case, we find the symmetry restoration of the streamfunction of the steady traveling solutions at high Reynolds number. Note is that The 3-jet zonal flow does not have this symmetry. On the torus case, Kim and Okamoto [14] studied the inviscid limit of the steady solutions arising from 4- and 6-jet trivial flows, and they found that along the branches the flow field of the steady solution becomes dominated only by a pair of a negative and a positive vortices at high Reynolds number. They called this solution *unimodal* solution, and suggested that at a high Reynolds number there is a steady unimodal solution independently of the value of k . Similar phenomena were found also by Okamoto and Shōji [23]. It should be noted that the symmetries of the steady solutions, which become the unimodal solutions at high Reynolds number, are restored as the Reynolds number increases. Considering the symmetry restoration in the torus case and the sphere case, it may be suggested that the symmetry restoration of the steady solutions at high Reynolds number is a common feature between the flat torus and the sphere. In the rotating case, on the other hand, we does not find the symmetry restoration of the steady traveling solutions.

We carry out time integrations at high Reynolds number. in the non-rotating case, we find that the solutions are chaotic and wander around unstable steady/steady traveling solutions. Observing the streamfunctions of chaotic solutions we expect that the properties of chaotic solutions can be obtained by using unstable steady/steady traveling solutions. As an example, we try to reproduce the zonal-mean zonal velocity of the chaotic solutions by using those of the unstable steady and steady traveling solutions. First, we consider the linear combination of the zonal-mean zonal flow of unstable steady/steady traveling solutions the coefficients of which are given by the properties of the energy distance between chaotic solutions and unstable steady/steady traveling solutions. This linear combinations, however, do not give the approximations to the time-averaged zonal-mean zonal flow of the chaotic solutions.

Next, we consider the linear mapping; if the linear mapping operates the steady/steady traveling solutions, the linear mapping gives the zonal-mean zonal velocity of the solution

which the linear mapping operates, while if the linear mapping operates the orthogonal compliment of the linear space which is extended by the unstable steady/steady traveling solutions, the linear mapping gives zero. We find that when the unstable steady/steady traveling solutions, which we obtain by the computational bifurcation analysis, are used for the linear mapping, the linear mapping gives good approximations to not only the time average but also the time series of zonal-mean zonal velocity of chaotic solutions. This result suggests that even the chaotic orbits at high Reynolds number, which is 40 times of the critical Reynolds number of the laminar flow, lies mostly within a relatively low-dimensional box, the vertices of which are the steady and steady traveling solutions.

In the rotating cases, on the other hand, the solution tends to be less chaotic under the stabilizing effect of rotation, and we find that the reproduced zonal flow by the linear mapping method does not approximate well the zonal-mean zonal velocity of the unsteady solutions at several Reynolds numbers and rotation rates. This result suggests that the relation between the unsteady solutions and the steady or steady traveling solutions changes as the effect of rotation increases.

Chapter 4

Conclusion

The two-dimensional incompressible Navier-Stokes flow on a rotating sphere is considered to be one of the simplest and most fundamental models of the atmospheric motions taking into account the effect of the planetary rotation. The Reynolds number of the planetary atmosphere is so large that properties of the Navier-Stokes turbulence on a rotating sphere should be relevant to some aspect of the dynamics of the atmosphere. However, even in this simplest model, it is far from straightforward to obtain global properties of fully nonlinear solutions. In this thesis we discuss the Navier-Stokes flows on a rotating sphere, with an attention focused on the stability problem, the bifurcation structure of the zonal jet flows and chaotic solutions at high Reynolds numbers.

First we investigate inviscid stability of zonal jet flows on a rotating sphere, shown in Chapter 2. The semi-circle theorem obtained by Howard [7] on non-rotating planer domain was expanded to the rotating sphere by Thuburn and Haynes [36]. However we obtained different results from that of Thuburn and Haynes to utilize a property of Legendre functions. Furthermore, we obtain corrected values of the critical rotation rate of stability. Baines [1] numerically studied the linear stability of inviscid zonal jet flow the streamfunction of which is expressed by the zonal spherical harmonics Y_l^0 . Re-examining the numerical calculation, we find that the eigenvalues obtained by the spectral method adopted by Baines [1] include numerical errors which do not decrease even by increasing the truncation wavenumber as far as practically available in the computation. These numerical errors are caused by an emergence of singularities, called as critical layers, near the north and the south poles when the zonal flow approaches the marginal stability state. To obtain the critical eigenvalues and critical rotation rates with sufficient accuracy, we make use of the shooting method and the power series expansion method, taking into account the singular points. As a result, we find that the critical rotation rates of Baines [1] should be corrected by $\sim 10\%$.

In the aforementioned paper, Baines also studied the stability of non-zonal Rossby waves, i.e. ψ_0 proportional to $Y_l^m(\lambda, \mu)$, ($m \neq 0$). However, we have found in high-resolution computations, that some of the stability results for these flows in Baines [1] also suffer from inaccuracy due to the singular point where the coefficient of the highest-order derivative of

the eigenfunction vanishes. The traditional technique of bypassing the singular point in the complex plane, which we have employed in this chapter, is applicable only to the problems of space dimension one. Accurate results of the stability eigenvalues for the two-dimensional problem is therefore still open to further study.

Second, in Chapter 3, we study stability and bifurcation structure of viscous zonal flow. This problem is formulated by introducing a forcing term, which consists of a single spherical harmonics, to balance with the viscous dissipation term to keep the flow steady. Notice that this problem setting is similar to so-called Kolmogorov problem which has been considered as a typical and simplest example to get insight into the solution properties of the Navier-Stokes equations.

We prove that the 2-jet zonal flow is globally asymptotically stable for any Reynolds number and the rotation rate. In Kolmogorov problem, Iudovisch [13] proved that 2-jet parallel flow is globally asymptotically stable for any Reynolds number. This result implies that the global stability of 2-jet flow is a common property between the flat torus and the sphere. We study linear stability of l -jet zonal flow in the region $3 \leq l \leq 9$. In non-rotating case, we find that as the number of jets increases the critical Reynolds number increases monotonically, the critical modes are Hopf mode, and the critical wavenumbers $m_c = 2$. In rotating case we find that the critical Reynolds number takes its lowest value at non-zero rotation rate; at a small negative rotation rate for the odd-jet zonal flow, and at a small non-zero rotation rate (both positive and negative values) for the even-jet zonal flow, while This means that the effect of small rotation is not always the stabilization of the zonal flows, while because the critical Reynolds number of each zonal jet flow increases rapidly the rotation rate increasing large, the zonal flows are stabilized by the large rotation rates. On the inviscid limit of the stability, we find that the unstable region of rotation rate for viscous odd-jet zonal flows is larger than that for inviscid zonal flows, and the former does not converge to the latter even in the inviscid limit. This seeming contradiction between the inviscid limit and the inviscid is resolved by an observation that as the Reynolds number increases the growth rates of the unstable mode converge to zero at the region, where the inviscid zonal flow is stable but viscous zonal flow unstable. Obuse et al. [22] reported that the asymptotic states of forced two-dimensional turbulence are only the 2- or 3-jet zonal flow. We find that in their calculation, the rotation rate is always larger than the critical rotation rate of the laminar jet flows, in the course of time development, except for some initial period. This means that the jet flows found in the intermediate stages would be mostly stable if the jet flows were laminar, and therefore the route to the asymptotic state of the forced turbulence is not explained in the framework of the linear stability of laminar zonal jet flows, while the stability of the resultant 3-jet flow is supported by the linear stability of the laminar 3-jet flow.

The bifurcation structure arising from the 3-jet zonal flow are studied. In non-rotating case, as Reynolds number increases, the steady traveling solution arises from 3-jet zonal flow through the Hopf bifurcation. As the Reynolds number increases, the several traveling solutions arise only through the pitchfork bifurcation from the traveling solutions and

finally the steady solutions become Hopf unstable. In the rotating case, when $\Omega < 0$, we find saddle-node bifurcation points and the closed-loop bifurcation branch while in $\Omega > 0$ case only the pitchfork bifurcation points. Then the bifurcation diagrams change significantly depending on the rotation. About the properties of steady traveling solutions at high Reynolds number, in non-rotation case, we find the symmetry restoration of the streamfunction of the steady traveling solutions at high Reynolds number. Similar phenomenon has been found in Kolmogorov problem by Okamoto and Shōji [23] and Kim and Okamoto [14]. On the other hand, in the rotating cases, no symmetry restoration is found.

We carry out time integrations at high Reynolds number. In non-rotating case, we find that solution orbits are chaotic, which wander around unstable steady/steady traveling solutions. Observing the streamfunction of chaotic solutions we expect that the properties of chaotic solutions can be obtained by using unstable steady/steady traveling solutions. In order to find out the relationships between the chaotic solutions and the steady/steady traveling solutions, we try to reproduce the zonal-mean zonal velocity of chaotic solutions using the unstable steady/steady traveling solutions. First, we consider the linear combination of the zonal-mean zonal flow of unstable steady/steady traveling solutions. The coefficients of linear combination are given by the properties of the energy distance between chaotic solutions and unstable steady/steady traveling solutions. This linear combination however does not give a good approximation to the time-average zonal-mean zonal flow of chaotic solutions. Next, we consider the linear mapping: if the linear mapping operates the steady/steady traveling solutions, the linear operator gives the zonal-mean zonal velocity of the operated steady/steady traveling solutions, while if the linear mapping operates the orthogonal complement of the linear space which is extended by the steady/steady traveling solutions, the linear operator gives zero. We find that this linear mapping reproduces not only the time average but also the time series of the zonal-mean zonal velocity of chaotic solutions. This result suggests that even at high Reynolds number, which is 40 times of the critical Reynolds number of laminar flows, the chaotic solutions exist on the linear space which is extended by the unstable steady solutions arising from 3-jet zonal flow at low Reynolds number. This suggestion brings a expectation that as the Reynolds number increases the dynamical dimension of the chaotic solutions of this model converges to finite. It is necessary for making this expectation clear to research dynamical system properties such as Lyapunov analysis and routes of turbulence. In the rotating cases, on the other hand, the solution tends to be less chaotic under the stabilizing effect of rotation, and we find that the reproduced zonal flow by the linear mapping method does not approximate well the zonal-mean zonal velocity of the solutions at several Reynolds numbers and rotation rates. This result suggests that the relation between the chaotic solutions and steady or steady traveling solutions changes as the effect of rotation increases.

Acknowledgements

I would like to express my deepest gratitude to Prof. Michio Yamada, who has introduced me to not only various knowledge of the physics and the mathematics but also how to approach the science and the researches. I am also sincerely appreciate to Prof. Shin-ichi Takehiro, who has given me essential insights of problem from simple but intrinsic questions. It's my great pleasure and honor to have studied under the precious supervisions of Prof. Yamada and Prof. Takehiro.

Dr. Yoshitaka Saiki, Dr.Miki U. Kobayashi and Dr. Youhei Sasaki have given fruitful and evaluative comments on my research project. Dr. Kiori Obuse has offered advice on the several research matters. I would also like to acknowledge meaningful and stimulating discussions of Masanobu Inubushi, Keiji Kimura and Kenta Ishimoto together with who I have studied at the same laboratory.

I would like to thank my friends and families, who have always supported me during the graduate course at Kyoto University.

Finally, I would like to be obliged to RIMS creating favorable and bright research environments. It is a treasure of my youth that I experienced in this prosperous institute.

Some of the data analyses and the visualisations in this thesis were done with ISPACK [11], Gtool5 library [19] and SPMODEL [34]. The numerical calculations were performed by the computer systems of the Research Institute for Mathematical Sciences, Kyoto University.

Bibliography

- [1] BAINES, P. G., 1976 The stability of planetary waves on a sphere. *J. Fluid Mech.* **73-2**, 193–213.
- [2] BALK, A. M., 1991 A new invariant for Rossby wave systems. *Phys. Lett. A* **155**, 20–24.
- [3] BOFFETTA, G. & ECKE, R. E., 2011 Two-dimensional turbulence. *Annu. Rev. Fluid Mech.* **44**, 427–451.
- [4] GALPERIN, B., SUKORIANSKY, S., DIKOVSKAYA, N., READ, P. L., YAMAZAKI, Y. H. & WORDSWORTH, R., 2006 Anisotropic turbulence and zonal jets in rotating flows with a β -effect. *Nonlin. Processes Geophys.* **13**, 83–98.
- [5] GOTOH, K., YAMADA, M. & MIZUSHIMA, J., 1983 The theory of stability of spatially parallel flows. *J. Fluid Mech.* **127**, 45–58.
- [6] GOTOH, K. & YAMADA, M., 1985 Stability of spatially periodic flows *Encyclopedia of Fluid Dynamics I*, edited by Chermisinoff, N. P., pp 1521 (Chap. 18, p. 589).
- [7] HOWARD, L. N., 1961 Note on a paper of John W. Miles. *J. Fluid Mech.*, **10**, 308–321.
- [8] HUANG, H.-P., GALPERIN, B. & SUKORIANSKY, S., 2001 Anisotropic spectra in two-dimensional turbulence on the surface of a rotating sphere. *Phys. Fluid*, **13**, 225–240.
- [9] INUBUSHI, M., KOBAYASHI, M. U., TAKEHIRO, S. & YAMADA, M., 2012 Covariant Lyapunov analysis of chaotic Kolmogorov flows. *Phys. Rev. E* **85**, 016331.
- [10] ISHIHARA, T., GOTOH, T. & KANEDA, Y., 2009 Study of high Reynolds number isotropic turbulence by direct numerical simulation *Annu. Rev. Fluid Mech.* **41**, 165–180.
- [11] ISHIOKA, K., 2011 ispack-0.96, <http://www.gfd-dennou.org/arch/ispack/>, GFD Dennou Club.

-
- [12] ISHIOKA, K. & YODEN, S., 1992 The stability of zonal flows in barotropic fluid on a rotating sphere. *Kyoto Univ. Res. Inst. Math. Sci. Kokyuroku* **782**, 113–124.
- [13] IUDOVISCH, V. I., 1965 Example of the generation of a secondary stationary or periodic flow when there is loss of stability of the laminar flow of a viscous incompressible fluid. *J. Appl. Math. Mech.*, **29**, 527–544.
- [14] KIM, S. C. & OKAMOTO, H., 2010 Stationary vortices of large scale appearing in 2D Navier-Stokes equations at large Reynolds numbers. *Japan J. Indust. Appl. Math.*, **27**, 47–71.
- [15] KURAICHNAN, R. H., 1967 Inertial ranges in two-dimensional turbulence. *Phys. Fluid*, **10**, 1417–1423.
- [16] KUO, H. , 1949 Dynamics instability of two-dimensional nondivergent flow in a barotropic atmosphere. *J. Meteo.*, **6**, 105–122.
- [17] MCWILLIAMS, J. C., 1984 The emergence of insulated coherent vortices in turbulent flow, *J. Fluid Mech.*, **146**, 21–43.
- [18] MESHALKIN, L. D. & SINAI, Y. G., 1962 Investigation of the stability of a stationary solution of a system of equations for the plane movement of an incompressible viscous liquid, *J. Appl. Math. and Mech.*, **25**, 1700–1705.
- [19] MORIKAWA, Y., TAKAHASHI, O. Y., SASAKI, Y., NISHIZAWA, S., OTOBE, N., ISHIWATARI, M., ODAKA, M., TAKEHIRO, S., HORINOUCI, T., HAYASHI, Y.-Y. & TOYODA, E., 2010 Gtool Development Group, 2010: Gtool5 library, <http://www.gfd-dennou.org/library/gtool/>, GFD Dennou Club.
- [20] NAZARENKO, S. & QUINN, N., 2009 Triple cascade behavior in quasigeostrophic and drift turbulence and generation of zonal Jets. *Phys. Rev. Lett.* , **103**, 118501.
- [21] NOZAWA, T. & YODEN, S., 1997 Formation of zonal band structure in forced two-dimensional turbulence on a rotating sphere *Phys. Fluid* , **9**, 2081–2093.
- [22] OBUSE, K., TAKEHIRO, S. & YAMADA, M., 2010 Long-time asymptotic states of forced two-dimensional barotropic incompressible flows on a rotating sphere. *Phys. Fluid*, **22**, 056601.
- [23] OKAMOTO, H. & SHŌJI, M., 1993 Bifurcation Diagrams in Kolmogorov’s Problem of Viscous Incompressible Fluid on 2-D Flat Tori. *Japan J. Indus Appl. Math.*, **10**, 191–218.
- [24] PEDLOSKY, J., 1964 The stability of currents in the atmosphere and the ocean: part I. *J. Atmos. Sci.*, **21**, 201–219.

BIBLIOGRAPHY

- [25] PEDLOSKY, J., 1987 *Geophysical Fluid Dynamics*, 2nd edition Springer pp709.
- [26] PLATT, N., SIROVICH, L. & FITZMAURICE, N., 1991 An investigation of chaotic Kolmogorov flows. *Phys. Fluid* , **3**, 681–696.
- [27] RHINES, P. B., 1975 Waves and turbulence on a beta-plane *J. Fluid Mech.* , **69**, 417–443.
- [28] SASAKI, E. TAKEHIRO, S. & YAMADA, M, 2012 A note on the stability of inviscid zonal jet flows on a rotating sphere, *J. Fluid Mech.*, **710**, 154–165.
- [29] SILBERMAN, I., 1953 Planetary waves in the atmosphere, *J. Meteo.*, **11**, 27–34.
- [30] SKIBA, Y. N., 1989 Mathematical Problems of the Dynamics of Viscous Barotropic Fluid on a Rotating Sphere., Dept. Numer. Mathematics USSR Academy of Sciences VINITI Moscow (Russian). 1990 Engl. Transl. Indian Institute of Tropical Meteorology. Pune INDIA pp. 211 (English).
- [31] SKIBA, Y. N., 2002 On the spectral problem in the linear stability study of flows on a sphere. *J. Math. Anal. Appl.*, **270**, 165–180.
- [32] SKIBA, Y. N., 2009 Linear instability of ideal flows on a sphere. *Math. Meth. Appl. Sci.*, **32**, 284–306.
- [33] SUKORIANSKY, S., GALPERIN, B. & DIKOVSKAYA, N., 2002 Universal spectrum of two-dimensional turbulence on a rotating sphere and some basic features of atmospheric circulation on giant planets. *Phys. Rev. Lett.* , **89**, 124501.
- [34] TAKEHIRO, S., SASAKI, Y., MORIKAWA, Y., ISHIOKA, K., ODAKA, M., TAKAHASHI, Y. O., NISHIZAWA, S., NAKAJIMA, K., ISHIWATARI, M., & HAYASHI, Y.-Y., 2011 SPMODEL Development Group, 2011 Hierarchical Spectral Models for GFD (SPMODEL), <http://www.gfd-dennou.org/library/spmodel/>, GFD Dennou Club.
- [35] TAKEHIRO, S., YAMADA, M. & HAYASHI, Y.-Y., 2007 Circumpolar jets emerging in two-dimensional non-divergent decaying turbulence on a rapidly rotating sphere. *Fluid Dyn. Res.*, **39**, 209–220.
- [36] THUBURN, J. & HAYNES, P., 1996 Bounds on the growth rate and phase velocity of instabilities in non-divergent barotropic flow on a sphere: A semicircle theorem. *Q. J. R. Meteo. Soc.*, **122**, 779–787.
- [37] TUNG, K. K., 1981 Barotropic instability of zonal flows. *J. Atmos. Sci.*, **38**, 308–321.
- [38] WILLIAMS, G. P., 1978 Planetary circulations: 1. Barotropic representation of Jovian and Terrestrial turbulence *J. Atmos. Sci.*, **35**, 1399–1426.

- [39] YODEN, S. & YAMADA, M., 1993 A numerical experiment on two-dimensional Decaying turbulence on a rotating sphere. *J. Atmos. Sci.*, **50**, 631–643.